UNIVERSITY OF MÜNSTER

MASTER THESIS

Local Coincidence Studies for a Multi-PMT Optical Module for IceCube Upgrade

Supervisor:
Prof. Dr. Alexander KAPPES

Second Supervisor:
Dr. Volker HANNEN

Anna-Sophia TENBRUCK

A thesis submitted in fulfillment of the requirements
*for the degree of **Master of Science***
at the University of Münster

in the

AG Kappes
Institute of Nuclear Physics

December 6, 2025

Declaration of Authorship

I, Anna-Sophia TENBRUCK, declare that this thesis titled, "Local Coincidence Studies for a Multi-PMT Optical Module for IceCube Upgrade" and the work presented in it are my own. I confirm that:

- This work was done wholly or mainly while in candidature for a research degree at this University.
- Where any part of this thesis has previously been submitted for a degree or any other qualification at this University or any other institution, this has been clearly stated.
- Where I have consulted the published work of others, this is always clearly attributed.
- Where I have quoted from the work of others, the source is always given. With the exception of such quotations, this thesis is entirely my own work.
- I have acknowledged all main sources of help.
- Where the thesis is based on work done by myself jointly with others, I have made clear exactly what was done by others and what I have contributed myself.

Signed:

Date:

Contents

1 Introduction

Astroparticle physics aims to understand the most energetic and violent processes in our Universe by studying particles that reach the Earth from cosmic accelerators. Over the past century, observations across the electromagnetic spectrum have revealed an active and dynamic cosmos, yet photons alone cannot probe the extreme environments in which high-energy particles are produced. Magnetic fields deflect charged cosmic rays, obscuring their origin, and high-energy gamma rays can be absorbed during propagation. To overcome these limitations, modern astronomy has expanded into multimessenger astronomy. Combining information carried by electromagnetic radiation, gravitational waves, cosmic rays, and neutrinos provides deeper insight into cosmic accelerators.

Among these messengers, neutrinos represent a unique probe of the Universe. Their extremely small interaction cross section allows them to escape dense astrophysical environments and propagate over cosmological distances without deflection or absorption, preserving directional information. They provide direct access to hadronic acceleration processes that are otherwise hidden to the other messengers. However, their properties make them exceedingly difficult to detect and require large detection volumes composed of transparent media. The IceCube Neutrino Observatory at the South Pole is currently the largest detector of this kind, embedding 5160 optical modules in $\sim 1\,\mathrm{km}^3$ of glacial ice to detect the Cherenkov photons generated indirectly from neutrino interactions [1].

Since its completion in 2011, IceCube detected a diffuse flux of high-energy neutrinos of cosmic origin with energies up to $\mathcal{O}(\mathrm{PeV})$ [1, 2]. Follow-up observations enabled the first identification of a high-energy neutrino with a blazar, TXS 0506+056, providing direct evidence for neutrino emission from an extragalactic accelerator [3]. In 2022, IceCube identified the Seyfert galaxy NGC 1068 as a significant neutrino emitter, which is a smoking gun signature of hadronic particle acceleration at this source [4]. However, the currently identified sources account for only a small fraction of the observed diffuse flux, motivating further detector expansions to uncover the remaining source population.

To improve the sensitivity in the GeV to TeV regime, which is essential, for example, for neutrino oscillation studies, and to achieve a better understanding of the Antarctic ice properties in which IceCube is embedded, the IceCube Upgrade is going to be deployed is going to be deployed during the 2025/26 austral summer [5]. IceCube Upgrade will instrument the central region of the detector with seven new, densely spaced strings hosting over 700 next-generation optical sensors which feature enhanced photon detection efficiency, improved timing resolution, and advanced in-ice calibration systems. A key device among these new sensors is the multi-PMT Digital Optical Module (mDOM), which, unlike the current digital optical modules in IceCube that contain a single downward-facing 10-inch-diameter photomultiplier tube (PMT), contains 24 3-inch-diameter PMTs arranged to cover the entire solid angle inside a pressure vessel [6]. This configuration increases the

effective photosensitive area, provides intrinsic directional information, and enable local coincidences within a single optical module, for example for background suppression.

The performance of the mDOM is not only governed by its photon detection efficiency but also by its optical background. At the depths of IceCube, the Antarctic ice exhibits extremely low optical activity. Consequently, the dominant contribution to the optical background arises from the mDOMs themselves. In particular, two processes are relevant: scintillation and Cherenkov photons produced by trace amounts of radionuclides contained within the borosilicate glass vessel of the mDOM, and uncorrelated PMT noise such as thermionic emission and afterpulsing. For a precise interpretation of mDOM data and to minimize the systematic uncertainties in IceCube Upgrade, a quantitative understanding of these background components is essential. Moreover, realistic simulations of the optical background are required for event reconstruction, calibration procedures, and performance studies for the future IceCube Upgrade and IceCube-Gen2 extensions [7].
Moreover, realistic simulations of the intrinsic optical background of the mDOM and, more generally, of its response are required for event reconstruction, calibration, and other essential tasks. For this reason, the Geant4-based OMSim framework was developed [8].
In this thesis, the simulation is benchmarked against controlled measurements in air and water, which quantify the background contributions under laboratory conditions, including those from atmospheric muons. A dedicated Geant4 simulation, using the OMSim framework, is employed and extended to model radioactive decays and muon-induced Cherenkov light, capable of reproducing the multiplicity-dependent detector response.

2 Astroparticle Physics

Astroparticle physics connects fundamental particle interactions with astrophysical phenomena by studying energetic particles that originate far beyond the solar system. Understanding their production, propagation, and detection is essential for interpreting the signals recorded by the IceCube Neutrino Observatory. This chapter introduces the physical principles underlying the detector's response.

2.1 Cosmic Rays

Cosmic rays consist of high-energy protons and atomic nuclei originating from astrophysical accelerators and propagating through the interstellar and intergalactic medium at relativistic speeds. They provide direct access to high-energy particles outside our solar system, offering crucial information about the non-thermal universe, particle acceleration mechanisms, and interstellar magnetic field. The characterization of the cosmic-ray flux is therefore a central component of astroparticle physics.

The observed spectrum spans over 12 orders of magnitude in energy, from $\sim 10^9$ eV up to energies exceeding 10^{20} eV, following a broken power law of the form $\left(\frac{dN}{dE} \propto E^{-\gamma}\right)$ [10]. The spectrum for all particles is shown in Figure 2.1. Distinct spectral features mark transitions in composition and origin. Cosmic rays below the so-called *knee* $\sim 10^{15}$ eV are attributed to Galactic sources [11]. Diffusive shock acceleration at supernova remnant shock fronts is considered the principal mechanism. Particles (Ultra-High Energy Cosmic Rays) above the so-called *ankle* $\sim 10^{18}$ eV are generally considered extragalactic. Potential sources for these particles, which require immense energy reservoirs, include Active Galactic Nuclei and gamma-ray bursts. The propagation of these highest energy particles is subject to the Greisen-Zatsepin-Kuzmin cut-off at energies above $\sim 5 \times 10^{19}$ eV, caused by photohadronic interactions with the Cosmic Microwave Background (CMB) photons [12].

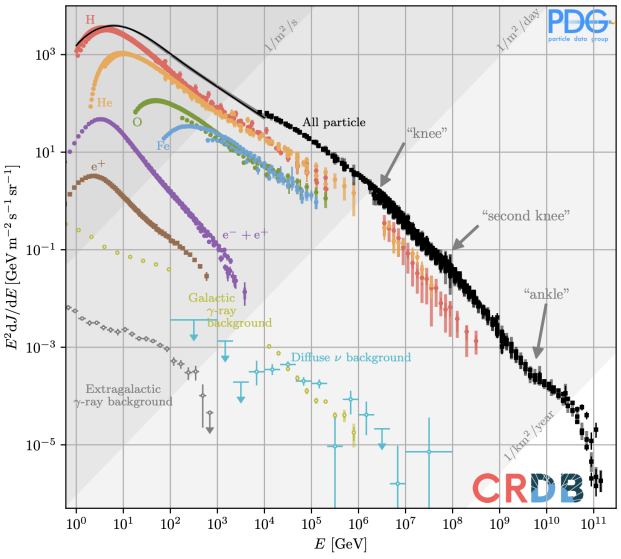

FIGURE 2.1: Primary cosmic ray energy spectrum for all particles. Figure taken from [9].

During propagation, charged cosmic rays experience continuous deflection by the interstellar magnetic fields, producing an almost isotropic arrival distribution. Upon entering the Earth's atmosphere, a primary cosmic ray initiates an extensive air shower, a cascade of secondary particles created through successive hadronic and electromagnetic interactions with atmospheric nuclei. The cascade develops until particle energies fall below critical thresholds, yielding a spatially extended distribution of various secondary particles at ground level, as illustrated in Figure 2.2 [10].

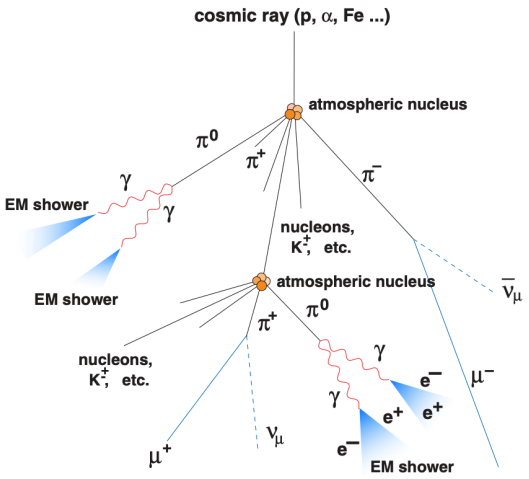

FIGURE 2.2: Schematic description of extended air showers caused by a cosmic ray interaction with the atmosphere. Figure taken from [13].

2.2 ATMOSPHERIC MUONS

Predominantly, pions and kaons are produced in the hadronic interaction of cosmic rays with the atmosphere's nuclei. These mesons form the dominant parents of the atmospheric muon component. Their subsequent decays via weak interaction populate the charged lepton sector and give rise to the muons observed at the ground. Astrophysical muons can hardly reach the Earth's atmosphere due to their lifetime ($\tau \sim 2\ \mu$s). This lifetime is however large enough that secondary muons produced in the air showers can reach the Earth's surface [12]. The dominant decay channels relevant for atmospheric muons are

$$\pi^{\pm} \to \mu^{\pm} + \nu_{\mu}\,(\bar{\nu}_{\mu}), \qquad K^{\pm} \to \mu^{\pm} + \nu_{\mu}\,(\bar{\nu}_{\mu}).$$

The mean energy at sea level is about 4 GeV [11].
The flux of muons above 4 GeV at sea level is approximately $60\,\mathrm{m}^{-2}\mathrm{s}^{-1}\mathrm{sr}^{-1}$. The flux exhibits a characteristic angular dependence. For muons of $E \sim 3$ GeV, the empirical approximation

$$I(\theta) \propto \cos^2\theta,$$

describes the zenith scaling, where θ denotes the incident zenith angle [11]. Low energy muons at large angles decay before reaching the surface.

2.2.1 Muon Energy Loss

Atmospheric muons lose a non-negligible fraction of their energy while traveling through dense or gaseous media such as air. The stopping is governed by two classes of processes whose relative importance evolves with energy. At low and intermediate energies, the dominant mechanism is electronic energy loss through ionization and excitation of atomic nuclei, accurately described by Bethe theory once the projectile is relativistic. For relativistic muons in material with low proton number Z (air, water, concrete), the standard minimum-ionizing muon energy loss is approximately $2\,\mathrm{MeV\,g^{-1}\,s^{-1}}$ [14]. At higher energies, radiative channels, mainly bremsstrahlung, pair production and photo nuclear interactions, introduce an additional contribution that scales approximately linearly with the muon energy. The mean stopping power can therefore be written as

$$-\frac{\mathrm{d}E}{\mathrm{d}x} = a(E) + b(E)\,E$$

where $a(E)$ is the electronic stopping power and $b(E)$ is the sum of the radiative coefficients. Their magnitudes depend on the medium, specifically on the proton number Z and the mass number A ($a \propto Z/A$ and $b \propto Z^2/A$). The energy loss of muons in copper as a function of momentum is shown in Figure 2.3. For copper, radiative losses dominate above $E_{\mu c} \simeq 315$ GeV [14]. In IceCube's low-Z medium, radiative losses dominate only $\gtrsim 1$ TeV [15].

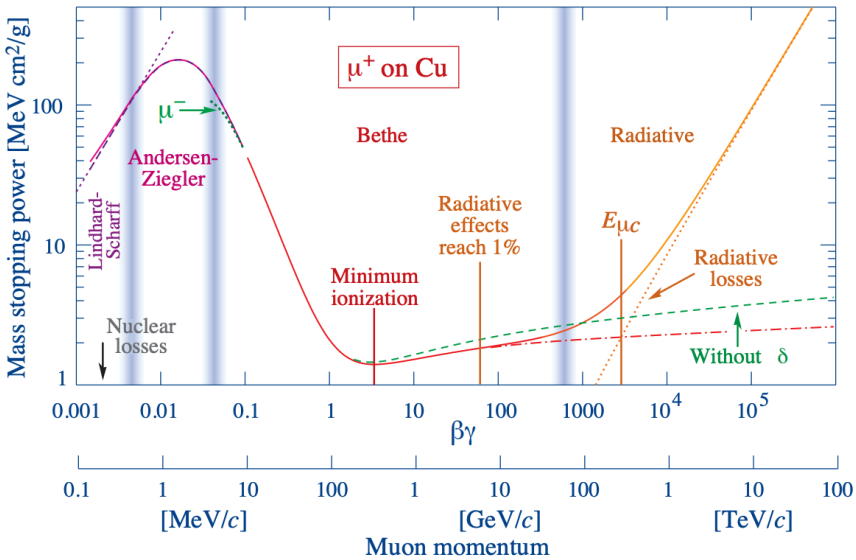

FIGURE 2.3: Mass stopping power for positive muons in copper as a function of the momentum in the 0.1 MeV to 100 TeV range. The rise in radiative loss becomes relevant above 100 GeV. Figure taken from [14].

2.2.2 INTERACTION AND DETECTION

Muon interactions in matter proceed predominantly through electromagnetic processes. Ionization yields continuous energy deposition along the muon's trajectory, whereas radiative interactions generate secondary electromagnetic or hadronic sub-showers at high energies [14]. Due to their long range and directional stability, muons are ideally suited as indicators of extensive air showers. Detection exploits their charged particle signatures through scintillation light, Cherenkov radiation, or secondary-cascade production, depending on the detector medium.

2.3 NEUTRINOS

Neutrinos are electrically neutral, weakly interacting elementary particles that appear in three flavors, each associated with a charged lepton - e, μ, τ. They possess nonzero but extremely small masses ($m_\nu < 0.45\,\text{eV}$, CL 90 %) [16]. Because they interact only via charged and neutral current weak processes, their cross sections increase approximately linearly with energy yet remain orders of magnitude below those of electromagnetic or strong interactions [17]. As a consequence, neutrinos travel cosmological distances essentially unperturbed and preserve information about their production sites.

2.3.1 PROPAGATION AND INTERACTION

Neutrinos are produced in a wide range of astrophysical and terrestrial processes, including beta decay, hadronic interactions in cosmic ray accelerators, nuclear fusion in stars, and particle cascades in the atmosphere. Their propagation over astronomical distances is facilitated by the small cross section, which results in interaction lengths far exceeding typical terrestrial scales.
A further central property of neutrinos is neutrino oscillation, first observed by the Homestake experiment in the 1960s and later by Kamiokande [18, 19]. It is the observed periodical conversion of neutrino lepton flavors and constitutes that neutrinos cannot be massless, as mentioned earlier. This discovery was honored with the Nobel Prize in Physics in 2015 [20].
Neutrino interactions with matter proceed via the weak interaction and are mediated by the corresponding massive gauge bosons $W^\pm$ and Z^0 [17]. Interactions via $W^\pm$ are classified as charged current (CC), while those via Z^0 described as neutral current (NC). The kind of interaction is dependent on the neutrino flavor as well as the energy, whereas the interaction partner adds further variety to the final outcome.
At neutrino energies above a few-GeV interactions are dominated by deep inelastic scattering with the constituent quarks of matter. The corresponding CC and NC interactions are

$$\nu_l + N \xrightarrow{W^\pm} l + X \qquad \text{(CC)}, \qquad \text{and} \qquad \nu_l + N \xrightarrow{Z^0} \nu_l + X \qquad \text{(NC)},$$

where ν_l denotes an (anti)neutrino with lepton flavor $l \in \{e, \mu, \tau\}$, N is a nucleon, and X represents the hadronic final state, which can develop in a complete hadronic cascade. CC interactions produce a charged leptopn, resulting in either a long track or a compact cascade depending on flavor and energy, whereas NC interactions deposit energy solely in the hadronic component.

2.3.2 Detection Principle

The detection of neutrinos in large-volume detectors relies on the observation of Cherenkov radiation emitted by relativistic charged leptopns in neutrino interactions. When a charged lepton created in a CC interaction, or secondary particles from a hadronic cascade, traverse a transparent, dielectric medium with a velocity exceeding the local phase velocity of light, coherent electromagnetic radiation is emitted. The condition for Cherenkov emission is

$$v > \frac{c}{n},$$

where v is the charged lepton's velocity, c the speed of light in vacuum, and n the refractive index of the medium [22].

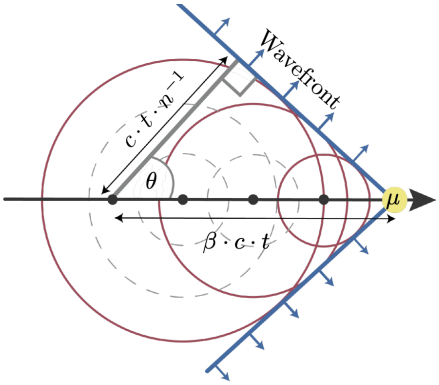

FIGURE 2.4: Sketch of a Cherenkov cone emitted by a muon traversing through a medium with refractive index n. The circular waves form a straight wavefront at the characteristic Cherenkov angle θ_C. Figure taken from [21]

A charged particle moving faster than the phase velocity of light in the medium induces a polarization of the surrounding molecules. Because the particle outruns the response time of the medium, the induced dipoles cannot return to equilibrium quickly enough, and the resulting electromagnetic fields add coherently. This constructive interference produces the characteristic Cherenkov wavefront shown in Figure 2.4. The opening angle θ_C of the Cherenkov cone is given by

$$\cos\theta_C = \frac{1}{n\beta}, \tag{2.1}$$

where $\beta = v/c$ [22]. For typical refractive indices of natural detection media, such as ice or water, this angle is around 41°. The emitted Cherenkov light forms a continuous wavefront that propagates through the medium, as seen in Figure 2.4 and can be recorded by optical sensors. The pattern and timing of the arriving photons encode the geometry of the underlying particle track or cascade. Muons produced in CC interactions generate extended, straight tracks that emit Cherenkov light along their complete propagation path (left Figure 2.5). In contrast, electrons and hadrons deposit their energy over short distances, producing compact cascades with nearly spherical light emission (middle Figure 2.5). Tau leptons, produced in CC interactions, typically decay within mm to m depending on energy, producing either a single a single cascade, or, at sufficiently high

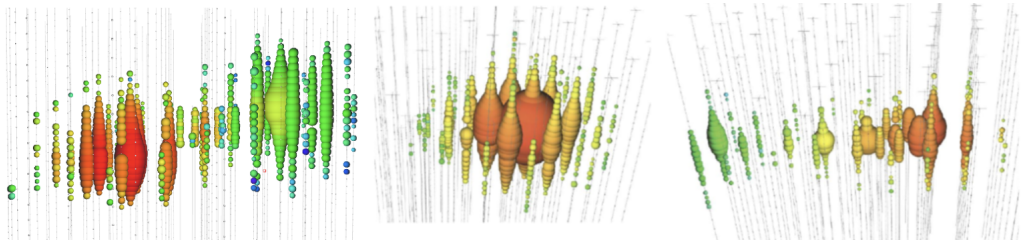

FIGURE 2.5: Examples of simulated light deposition signatures of cascades (left, middle) and tracks (right) within a detector volume instrumented with optical sensors. The color indicates the the arrival time of the photons, going from read (early) to blue (later), while the size of the sphere corresponds to the amount of the detected light. Picture courtesy of the IceCube collaboration.

energies, two spatially separated cascade (left Figure 2.5). NC interactions contribute exclusively to the cascade channel since the outgoing neutrino remains undetected.
The detection of these Cherenkov photons requires a medium with high optical transparency and sensitive optical sensors capable of resolving faint and temporally precise light signals. In addition, due to their low cross section, immense detector volumes are needed. For that reason, water and ice are mostly chosen, since they are naturally abundant in large quantifies on Earth. The reconstruction of direction, energy, and event topology is based on the distribution of detected photons within the instrumented volume.
The most extensive realization of this detection principle is the IceCube Neutrino Observatory, which at present constitutes the largest neutrino detector in the world. The following sections introduce its structure and operating principles.

2.4 THE ICECUBE NEUTRINO OBSERVATORY

The IceCube Neutrino Observatory is a cubic-kilometer Cherenkov detector embedded in the deep glacial ice at the geographic South Pole. Its purpose is to detect high energy neutrinos through the observation of Cherenkov light emitted by secondary charged particles produced in neutrino interactions within or near the instrumented volume. The exceptionally clear Antarctic ice provides a natural, optically transparent medium whose absorption and scattering properties enable photon propagation over hundreds of meters, an essential requirement for large scale neutrino detection.
IceCube comprises 86 vertical strings, each equipped with 60 Digital Optical Modules (DOMs), deployed at depths between roughly 1450 m and 2450 m. A sketch of the Observatory is shown in Figure 2.6. The strings form a grid with an average horizontal spacing of 125 m, yielding a three-dimensional array of 5160 optical sensors. Each DOM contains a 10-inch photomultiplier tube (PMT), digitization and timing electronics, and calibration devices housed inside a pressure resistant glass sphere. DOMs record photon arrival times with nanosecond precision and measure the integrated charge, allowing the reconstruction of the direction, energy and topology of neutrino induced events. The energy of the initial neutrinos ranges from 100 GeV to $\mathcal{O}(\text{PeV})$. For lower energies on the order of tens of GeV, *DeepCore* is more densely instrumented in the center of the detector.

At the surface, *IceTop* consists of water tank, including 2 DOMs each, spanning 1 km^2 of the surface area above the IceCube strings. IceTop enables detailed studies of the mass composition of primary cosmic rays in the energy range $\sim$ 100 TeV to 1 EeV and acts as a veto for events by tagging mainly penetrating atmospheric muons and some atmospheric neutrinos, thereby identifying non-starting events that are not of astrophysical origin [23].
Since its completion in 2011, IceCube has established the existence of a diffuse flux of high-energy astrophysical neutrinos. The limited event statistics, however, constrain the precision of spectral and source studies, creating the need for larger instrumented volumes and improved calibration capabilities. The next steps for expanding the detector's capabilities are IceCube Upgrade and IceCube-Gen2.

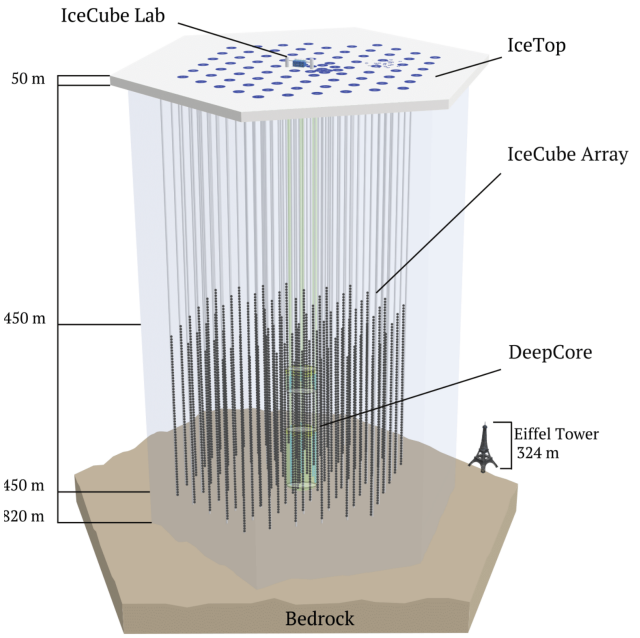

FIGURE 2.6: Layout of the IceCube Observatory infrastructure at South Pole. The lines represent the strings and the dots the optical modules. Courtesy of the IceCube collaboration.

2.4.1 ICECUBE UPGRADE AND ICECUBE-GEN2

IceCube Upgrade represents the first stage of the extension of the current IceCube detector and is being deployed during the 2025/26 Antarctic Summer season within the DeepCore region in depths of 2150 m to 2435 m [5]. Figure 2.7 illustrates the footprint of IceCube Upgrade in the current IceCube array (right side). Seven new strings will be concentrated in the deepest part of the ice from 2100 m to 2450 m, where the ice has the best optical properties [24]. Each string is equipped with a new optical sensors and dedicated calibration devices. Their primary objectives are to improve the characterization of the optical properties of the ice, enhance the precision of event reconstruction, and extend the sensitivity to neutrinos in the few-GeV energy range [5]. Each string will be equipped with new optical sensors, primarily 402 multi-PMT Digital Optical Modules (mDOMs) and 277 D-Eggs [25]. As the mDOM is a central subject of this thesis, it will be described in detail in Chapter 3. With the increased instrumentation density, the Upgrade will enable precision measurements of atmospheric neutrino oscillations, provide improved constraints on the neutrino mass ordering, and allow for one of the most stringent tests of the unitarity of the PMNS matrix to date and improve the sensitivity to potential signals from dark matter interactions [5],[26]. In addition, the Upgrade serves as a testbed for novel sensor concepts and advanced calibration techniques designed for next-generation detectors. These improvements will benefit not only future measurements but also enable the re-analysis

of IceCube's data archive, improving energy and angular resolution due to reduced systematics stemming from better knowledge of the ice properties.
Beyond IceCube Upgrade, IceCube-Gen2 represents the planned large-scale expansion of the observatory. IceCube-Gen2 plans to increase the detection volume of the main optical array by a factor of eight with an additional radio surface array that extends the instrumented volume and effectively expands the accessible neutrino energy into the EeV regime [7]. Figure 2.7 summarizes all ongoing and planned extensions of the IceCube Neutrino Observatory: from right to left the IceCube Upgrade, the current IceCube array, the envisioned IceCube-Gen2 optical array, and the large-scale Gen2 radio surface array.

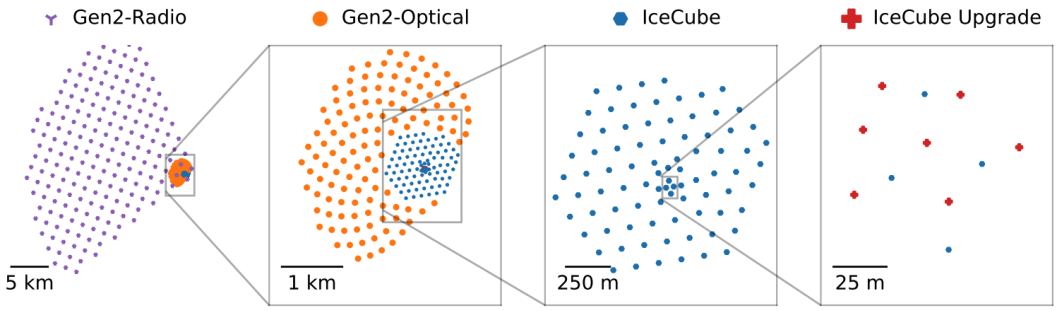

FIGURE 2.7: Footprint of the envisioned IceCube-Gen2 radio array (left) and optical array (mid left) compared to the current IceCube footprint (mid right). On the right is IceCube Upgrade, considered as the first phase of IceCube-Gen2. Figure taken from [7].

3 Multi-PMT Optical Module

The multi-PMT Digital Optical Module (mDOM) is one of the primary optical sensors of IceCube Upgrade [28]. It integrates 24 3-inch photomultiplier tubes (PMTs) within a compact pressure vessel, providing intrinsic directional sensitivity, high dynamic range, and enhanced background suppression capabilities. Its design follows the concept introduced by KM3Net [29], but is adapted to the environmental, mechanical, and readout constraints of the South Pole deployment. The following sections describe the hardware design of the mDOM as required to understand the background response characteristics central to this work. Figure 3.1 shows a picture of the mDOM (top).

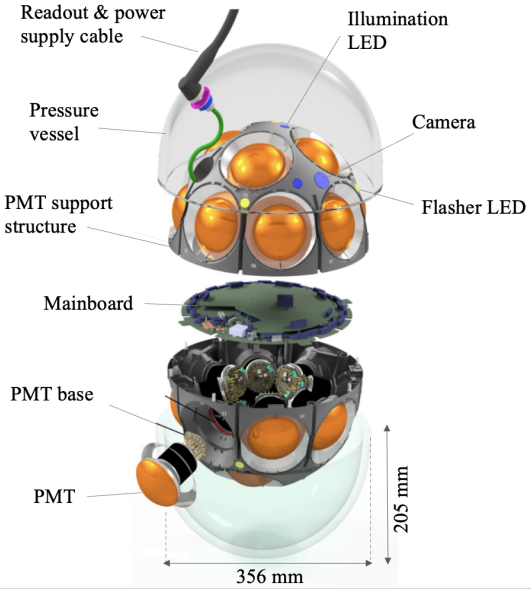

FIGURE 3.1: Top: Picture of an mDOM. Courtesy of the IceCube collaboration. Bottom: exploded view showing the arrangement of 24 PMTs and the mainboard region. Taken from [27].

3.1 Design

The mDOM is housed in a borosilicate glass vessel with an outer diameter of 356 mm and a height of 410 mm [30]. An exploded view can be found in Figure 3.1 (bottom). The vessel is composed of two 13 mm thick glass hemispheres joined at an equatorial interface and held together by two crossed metal bands. The glass half spheres are made of Vitrovex glass, chosen for its high transparency and its verified tolerance against static pressure exceeding 700 bar [31]. Inside the vessel, the 24 PMTs are mounted on two 3D-printed hemispherical support structures. Each hemisphere hosts twelve PMTs arranged in a fixed orientation: four polar PMTs and eight equatorial PMTs.

A thin layer of optically clear silicone gel fills the volume between the PMTs and the inner glass surface [32]. The gel provides optical coupling with a

refractive index similar to the one of the glass, ensuring minimal losses due to total internal reflection. The support structure holds each PMT in a fixed orientation and also provides defined mounting points for the embedded calibration devices. These include ten LED flashers, four illumination LEDs, and three cameras used for in-ice calibration and orientation monitoring.
Reflective cones around each PMT increase the effective photon collection area, and their reflectivity and angular shape have been optimized to enhance the response for incident Cherenkov photons. These passive optical elements influence the spatial distribution of photon detections.

3.2 PHOTOMULTIPLIER TUBES

PMTs are photodetectors capable of detecting single photons with high gain and subnanosecond timing precision. Their performance is governed by three fundamental processes: photoelectron emission at the photocathode, electron multiplication along the dynode chain, and signal readout at the anode.

3.2.1 STRUCTURE AND OPERATION PRINCIPLE

A PMT consists of a photosensitive photocathode evaporated onto the inside of a glass entry window, followed by focusing electrodes, a subsequent multiplication stage consisting of multiple dynodes, and an anode, as seen in Figure 3.2. When a photon reaches the photocathode, it can release an electron via the photoelectric effect if its energy exceeds the material-specific work function [33]. The initial photoelectron is accelerated towards subsequent dynodes by an externally supplied high voltage.

At each dynode, secondary emission amplifies the number of electrons by a factor δ_i, leading to an approximately exponential gain along the multiplier chain. For a PMT with n dynodes, the total gain is

$$G = \prod_{i=1}^{n} \delta_i. \tag{3.1}$$

Typical gains range from 10^5 to 10^7 at nominal operation voltage [34]. Focusing electrodes shape the electron trajectories such that photoelectrons are directed efficiently onto the first dynode.

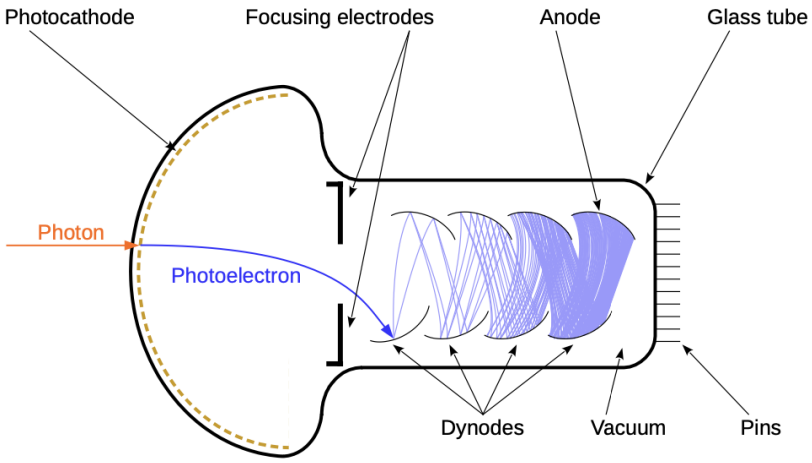

FIGURE 3.2: Schematic structure of a PMT, showing photocathode, focusing electrodes, dynode chain, and anode. Taken from [32].

3.2.2 QUANTUM EFFICIENCY

The quantum efficiency (QE) is the probability that a photon incident on the photocathode produces a photoelectron. Experimentally it is defined as

$$\mathrm{QE}(\lambda) = \frac{N_{\mathrm{pe}}}{N_{\gamma}}.$$

Bialkali[1] photocathodes used in the Hamamatsu R15458-02/20 PMTs for the mDOM reach peak QE values of 25% − 35% around 350 nm − 420 nm [28]. The long-wavelength cutoff is governed by the photoemission threshold, typically around 650 nm for bialkali materials [34]. At short wavelengths, the effective QE is limited primarily by two factors: the absorption in the borosilicate entry window, whose transmission falls steeply below ∼ 300 nm, and the photocathode material itself, whose photoemission probability decreases once photon energies exceed the range efficiently converted into photoelectrons [32, 34].

3.2.3 TIME CHARACTERISTICS

The transit time (TT) is defined as the delay between photon absorption at the photocathode and the appearance of the corresponding charge pulse at the anode. It is governed by photoelectron drift times and the electric-field configuration inside the dynode system. For the mDOM PMTs the TT is 43 ns [28]. Electron trajectories vary depending on the emission position, the initial emission angle, and the residual kinetc energy with which the electron exits the photocathode. These variations introduce a statistical broadening of the arrival times known as the transit-time spread (TTS). It quantifies the intrinsic temporal resolution of the PMT and is typically between 1-3 ns (FWHM) [34]. The TTS directly

[1] A combination of materials including two alkali metals [34].

limits the achievable coincidence.
The rising and falling edges of the PMT pulse are characterized by the $10\% - 90\%$ rise and fall times, which reflect both the electron multiplication dynamics within the dynode chain and the bandwidth limitations of the readout circuit. The signal width is commonly characterized by its full width at half maximum (FWHM). Figure 3.3 illustrates the characteristic timing response of a PMT.

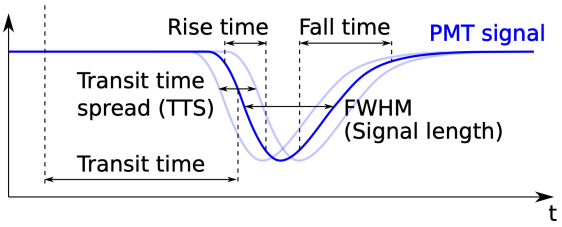

FIGURE 3.3: Illustration of the timing characteristics of the PMT output. Taken from [32].

3.2.4 UNCORRELATED NOISE

Even in the absence of incident photons, PMTs produce pulses due to several internal processes, all of which contribute to the **intrinsic dark rate**, defined as the rate of spurious pulses not caused by external photons [33]. The dominant contributions are

- **Thermionic emission**: thermal excitation of electrons at the photocathode or early-stage dynodes. It constitutes the primary contribution near room temperature and increases exponentially with temperature T:

$$R_{\text{th}}(T) \propto T^2 \cdot \exp\left(-\frac{W}{k_B T}\right), \tag{3.2}$$

  where W is the effective work function of the photocathode and k_B is Boltzmann's constant. Equation 3.2 describes the temperature dependence of the thermionic dark rate R_{th}, showing strong suppression at low temperatures and rapid growth toward higher temperatures.

- **Field emission**: electrons emitted from sharp structures at high electric fields, relevant at high voltages.

- **Leakage currents**: unintended conductive paths between electrodes on the glass and along insulating surfaces. They dominate the dark current whenever surface contamination is present.

- **Trace Isotopes**: decays of trace isotopes in the glass envelope-most prominently ^{40}K-produce energetic secondaries that generate Cherenkov or scintillation light in the glass. A detailed description is done in Chapter 4.

The arrival times of uncorrelated noise pulses follow a Poisson process, resulting in exponentially distributed inter-arrival times. Typical dark-rate levels for 3-inch bialkali PMTs operated at low temperature range from a few tens to several hundred counts per second, depending on photocathode material, temperature, and applied high voltage [33].

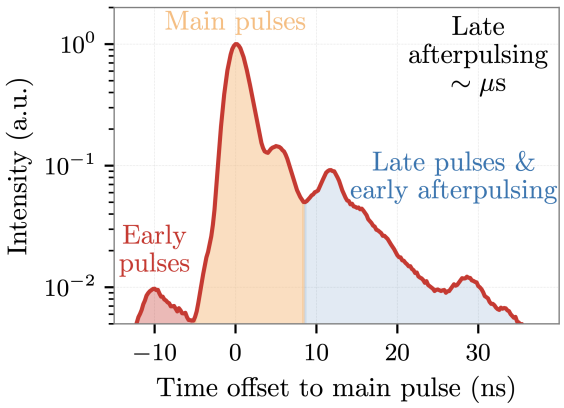

FIGURE 3.4: Time distribution of PMT pulses relative to the main pulse, illustrating early pulses (prepulsing), delayed and afterpulses. Figure taken from [35].

3.2.5 CORRELATED NOISE

Correlated noise refers to pulses that occur at characteristic times relative to a preceding main pulse. In contrast to uncorrelated noise, these pulses originate from processes triggered by the primary photoelectron or the primary avalanche. Their timing structure allows a classification into prepulsing, delayed pulsing, and afterpulsing, each linked to a specific microscopic mechanism. Figure 3.4 shows the characteristic time distributions of these processes.

PREPULSES

Prepulses originate from photons that pass though the photocathode and release electrons at the first dynode or other internal metallic structures, which can carry similar photoemissive coatings, rather than ar the photocathode itself. Since these electrons start at the first dynode instead of the photocathode, their drift path is shorter and the resulting pulse arrives earlier than the main pulse. This time difference is typically of order

$$t_{\text{pre}} \sim 10\,\text{ns to } 20\,\text{ns},$$

for 3-inch PMTs like the mDOM PMTs [32]. Prepulses amplitudes are usually smaller than the main pulse due to the short electron multiplication chain. Prepulse probabilities are typically below 1 % [34].

LATE PULSES

Late pulsing is caused by elastic backscattering of the primary photoelectron at the first dynode. The backscattered electron performs a longer trajectory before being reaccelerated towards the first dynode. This results in pulse delays typically of

$$t_{\text{delay}} \sim 15\,\text{ns to } 80\,\text{ns},$$

with amplitudes comparable to the main pulse, reflecting the full multiplication chain being active. Delayed pulsing represents less than 5 % of all pulses in typical 3-inch bialkali PMTs [32].

AFTERPULSING

Residual gas molecules inside the PMT can be ionized by the electron avalanche. The resulting positive ions drift back toward the photocathode or early-stage dynodes, where their impact releases secondary electrons. These electrons initiate a secondary pulse after a characteristic drift time. The delay is set by the ion drift velocity, leading to afterpulses occurring at typical timed of

$$t_{\text{after}} \sim 100\,\text{ns} - 10\,\mu\text{s}$$

after the primary pulse. In mDOM PMTs, afterpulses appear with a probability of about 8 % and an average delay of $< 6\,\mu$s, while their amplitudes range from single-photoelectron signals to several photoelectrons depending on the ion species [35].

3.2.6 SINGLE-PHOTOELECTRON SPECTRUM

The SPE spectrum describes the PMT response to an individual photoelectron, although in practice 2–3 photoelectrons may reach the photocathode within the transit-time spread and generate overlapping signals. A typical spectrum is shown in Figure 3.5 and consists of a pedestal, originating from electronic noise, a valley separating noise from true photoelectron signals, and a distinct SPE peak. The mean position of the 1-PE peak defines the PMT gain, while the peak-to-valley ratio quantifies the separation between noise and single-photoelectron signals and is an important performance indicator of low-noise PMTs.

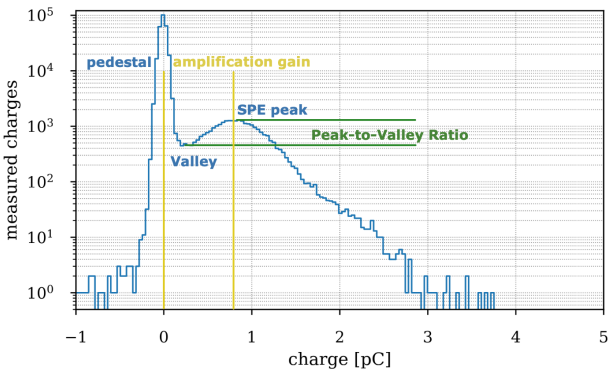

FIGURE 3.5: Representative SPE spectrum illustrating pedestal, valley, SPE peak, and amplification gain. The peak-to-valley ratio quantifies the separation between noise and single-photoelectron signals. Figure taken from [36].

3.2.7 HAMAMATSU R15458-02/20 PMT

The mDOM houses 24 Hamamatsu R15458-20 PMTs, each with a 80 mm diameter photocathode and an attached active high-voltage base (μBase) [30]. Figure 3.6 shows a photograph of such a PMT with its active base attached to the back. The compact base generates the dynode voltages and enables operation within the confined space of the pressure vessel. Each PMT is identified by a unique serial number (DMxxxxx) and all PMTs underwent a dedicated acceptance test prior to integration into the module [36]. The acceptance tests revealed a characteristic discontinuity in the intrinsic dark rate behavior between early-batch PMTs (DM $\leq$ 01130) and later production batches [37]. The early PMTs meet the nominal dark rate specification (found in Appendix B), whereas the majority of the later batches exhibit substantially elevated intrinsic dark noise rates due to increased concentrations of radioactive isotopes such as ^{40}K in the PMT glass [28]. The distribution of measured dark rates is shown in Fig. 3.7. The mDOM examined in this work contains exclusively early-batch PMTs and therefore constitutes a module assembled from PMTs meeting the nominal noise requirements (Table B.1).

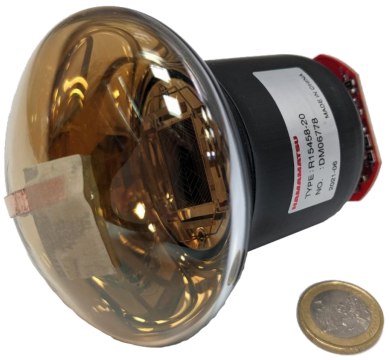

FIGURE 3.6: Hamamatsu R15458-20 PMT with integrated active base used in the mDOM. Figure taken from [36].

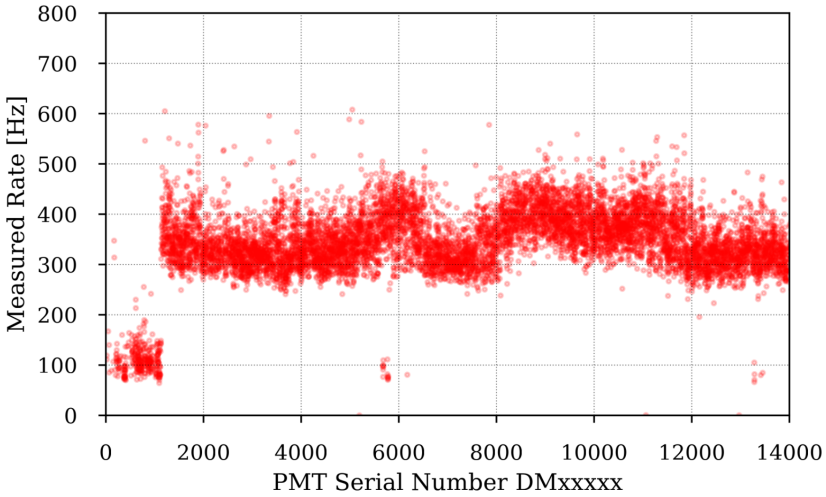

FIGURE 3.7: Measured intrinsic PMT dark rates in the scope of the acceptance tests as a function of the serial numbers of the PMTs. PMTs with serial numbers after DM01130 do not meet the specification of the dark rates. Figure taken from [37].

3.3 COMMUNICATION AND DATA ACQUISITION

The mainboard integrates the electronics required for PMT operation, signal processing, data acquisition, and communication [38]. Power and data are transmitted through a single twisted-pair line in the penetrator cable assembly. Inside the module, the IceCube Communication Module (ICM) separates power and data streams and provides the synchronized system clock used by the module electronics.
Each PMT is connected to an individual analog front-end (AFE) channel on the mainboard. The AFE splits the analog signal into two parallel paths (see Figure 3.8). One path is shaped by a low-pass filter (LPF) and amplifier chain and digitized by a 12-bit analog-to-digital (ADC) operating at 120 MHz. The second path is processed by a leading-edge discriminator sampled at 960 MHz, providing $\sim$ 1 ns time resolution for photon hit extraction. The discriminator threshold of each channel is set via a 16-bit digital-to-analog (DAC) converter, enabling operation at a well-defined sub-photoelectron level.
All waveform and timestamp data are handled by a field-programmable gate array (FPGA), which manages the readout sequencing, hit formation, and temporary storage in a 2 Gbit DDR3 memory. The FPGA also interfaces with the calibration devices and the ICM. This architecture enables precise photon-timing measurements across all 24 PMTs while keeping the power consumption and electronics complexity within the constraints required for deep-ice operation. Figure 3.8 shows a picture of the mainboard and a schematic block diagram of the AFE.

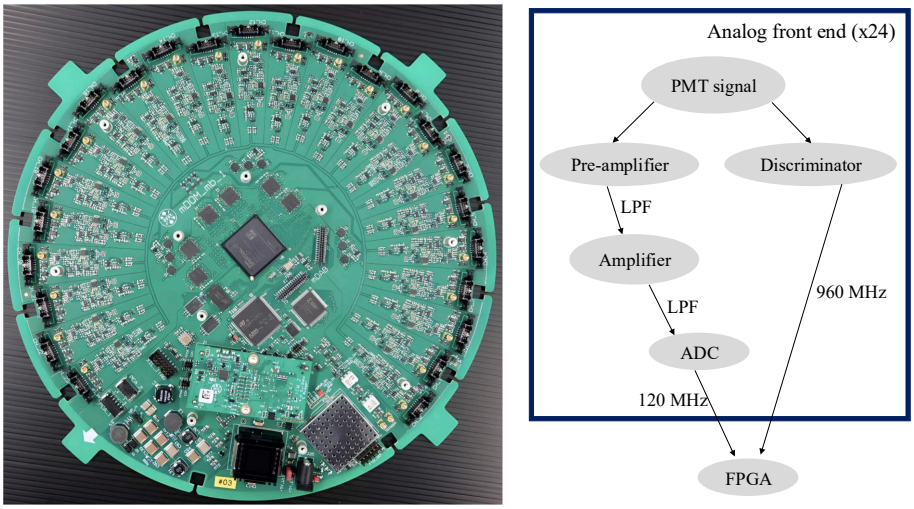

FIGURE 3.8: **Left:** Picture of the mDOM mainboard. Taken from [28]. **Right:** Schematic block diagram of the AFE of each PMT. PMT signals are split into two paths.

4 Optical Background of the mDOM glass

The intrinsic optical background of the mDOM originates from radioactive decays inside the borosolicate pressure vessel and the PMT bulb glass. Decays from the U- and Th-chains and from ^{40}K emit α particles, β electrons and γ rays, which deposit energy in the glass and generate two optical emission mechanisms: scintillation and Cherenkov radiation [21]. Scintillation is initiated by all three particle types through ionization and excitation of the electronic system, followed by radiative or non-radiative relaxation [39]. Cherenkov emission occurs only for electrons whose velocity exceeds the threshold condition $\beta > 1/n$. Using this condition, the corresponding kinetic–energy threshold in Vitrovex glass is

$$E_{\text{thr}} = m_e c^2 \left(\frac{1}{\sqrt{1 - 1/n^2}} - 1 \right) = 0.18\,\text{MeV}, \tag{4.1}$$

reached by β electrons and by Compton electrons from MeV γ rays. α particles, with energies of only a few MeV, remain far below threshold and do not generate Cherenkov photons [21]. The Cherenkov spectrum extends toward short wavelengths and overlaps with the scintillation band, but remains temporally prompt ($\sim$ ps-scale). Both scintillation and Cherenkov photons propagate through the glass and optical gel and can be detected by the mDOM PMTs.

4.1 Radioactive Isotopes in mDOM Components

The VITROVEX® borosilicate pressure vessel and the PMT bulb glass contain trace concentrations of the ^{238}U, ^{235}U, and ^{232}Th decay chains, as well as ^{40}K [21]. These decay chains produce a sequence of α, β, and γ emissions through their daughter isotopes. The absolute number of decays in a given component scales with its specific activity (in Bq/kg) and mass. The mean specific activity measured for four Vitrovex glass samples is listed in Table 4.1. The activities were measured in the scope of a Master thesis [28] using γ-spectroscopy. The measurements showed good agreement among three samples, while one sample exhibited no detectable ^{40}K, indicating batch-to-batch variations. A sample of the optical gel used between the PMTs and the pressure-vessel glass was also assayed and showed no measurable radioactivity.

TABLE 4.1: Activity per mass of the three natural decay chains and ^{40}K measured Vitrovex glass. Data taken from [28].

Decay	Specific activity (Bq/kg)
^{40}K	60.98 ± 0.86
^{238}U chain	4.61 ± 0.07
^{235}U chain	0.59 ± 0.05
^{232}Th chain	1.28 ± 0.05

PARTICLE TYPES AND THEIR EMISSION IN THE MDOM

- α **particles** originate from U- and Th-decay chains. They deposit energy over very short ranges via dense ionization and excitation, and are far below the Cherenkov threshold in the glass. Hence, they are only producing scintillation photons.
- β **electrons** arise directly from β decays throughout all isotopes. They deposit energy via ionization and excitation along extended tracks. Their energies can exceed the Cherenkov threshold, and they also excite scintillation.
- γ **rays** emerge throughout all isotopes. They interact predominantly by Compton scattering in the glass at MeV energies, producing Compton electrons which then lose energy as they traverse the material as well, resulting in scintillation and Cherenkov emission.

PARTICLE TYPES AND THEIR EMISSION OUTSIDE THE MDOM

Particles produced inside the mDOM could in principle leave the module into the outer environment. Depending on the medium, additional emissions can occur. Here, only air and water are considered.

- α **particles** stop within tens of micrometers in glass and will effectively never reach the surrounding medium.
- β **electrons:** MeV e^- can in principle escape only if created within $\mathcal{O}(\text{mm})$ of the interface, which is possible considering the glass thickness of 13 mm. Only in water do they exceed the Cherenkov threshold and emit prompt, directional Cherenkov light along short (mm–cm) tracks. However, probably only a small fraction will intersect again with the mDOM, reaching PMT, which can detect the light.
- γ **rays** can easily exit the glass. In **water** they predominantly Compton scatter within cm to tens of cm, producing recoil electrons whose Cherenkov cones can hit the mDOM and might be detected by the PMTs.

4.2 Scintillation in Borosilicate Glass

Scintillation denotes the radiative de-excitation that follows energy deposition by charged particles in the glass. As discussed above, the relevant particles are electrons from β^- decays, electrons from Compton scattering of γ rays, and α particles from the U- and Th-decay chains. The resulting scintillation spectrum $S(\lambda)$ is broad (near-UV/blue), the emission is delayed with a multi-component time profile $f(t)$, and the light yield depends on temperature and ionization density. This section states the phenomenology and the parametrization used later for simulations.
Scintillator response is parameterized by three measurable functions:

- **Yield** Y (photons/MeV): mean photon number per deposited energy.
- **Time profile** $f(t)$: time distribution of photon emission.
- **Emission spectrum** $S(\lambda)$: wavelength-dependent energy distribution.

These macroscopic quantities arise from the microscopic excitation and relaxation processes in the glass. Figure 4.1 illustrates these processes in configuration–coordinate space. The lower and upper curves represent the ground- and excited-state potential energy surfaces as a function of the configuration coordinate Q. The displaced minima at Q_g and Q_e give rise to the Stokes shift [40].

When a charged particle traverses the glass, it excites valence electrons or electrons in localized defect states into electronically excited vibrational levels of the upper potential surface, with energies in the absorption band centered around E_a [39]. This excitation occurs on femtosecond timescales. The excited electronic configuration then relaxes vibrationally by phonon emission on sub-picosecond to picosecond timescales, reaching the lowest vibrational level ($m = 0$) of the excited-state potential. From this relaxed level, radiative recombination to vibrational states of the ground-state potential takes place on nanosecond to microsecond timescales, producing the scintillation photons. The emitted photon energy corresponds to the emission band centered around $E_e < E_a$ [39].

A competing non-radiative recombination channel exists, shown in the right panel. To access this path, the system must cross the activation barrier W separating the radiative valley from the non-radiative crossing point. Relaxation through this channel releases the excitation energy as heat and produces no light. The competition between radiative and non-radiative decay determines the scintillation yield. High ionization-density projectiles, such as α particles, cause strong quenching because their dense energy deposition locally saturates the available excitation channels, which reduces the scintillation yield [21]. Temperature has the same qualitative effect: higher temperatures enhance the phonon population and facilitate activation over the barrier, reducing the light yield, whereas lower temperatures suppress non-radiative relaxation and increase $Y(T)$. This temperature dependence is known as **thermal quenching**, the thermally activated enhancement of non-radiative multiphonon relaxation via the barrier W, which reduces the radiative yield at elevated temperatures.

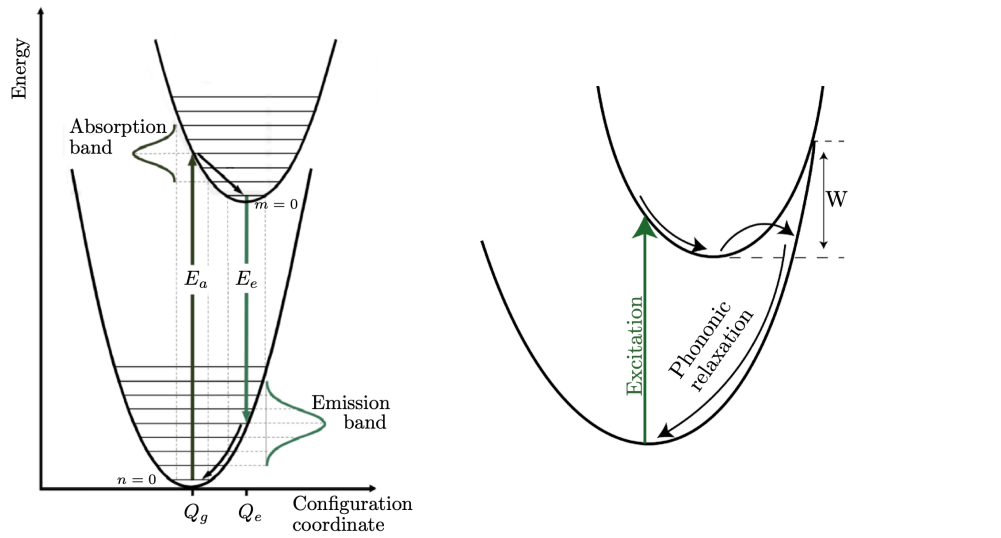

FIGURE 4.1: Configuration–coordinate diagram of the radiative and non-radiative relaxation pathways in borosilicate glass. Taken from [21].

Measurements of Vitrovex samples in the sub-zero operating temperature range showed $Y_e(T)/Y_\alpha(T) \approx 1.6$ to 1.7, with Y_e and Y_α the electron- and α-induced yields [35]. Electrons therefore produce more light per MeV than α particles, because of the stronger quenching of α tracks. Figure 4.2 shows the measured α-induced yield as a function of the temperature. The same dependence follows for the electron.

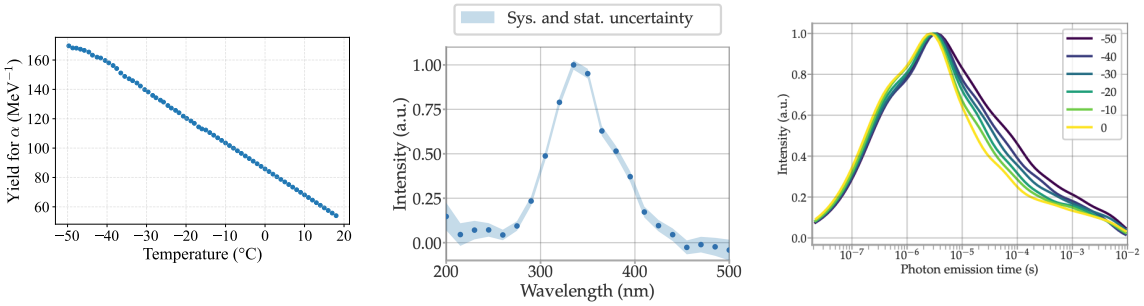

FIGURE 4.2: Scintillation characteristics for Vitrovex glass. Taken from [41] (left), [28] (right), and [35] (middle).

5 Background Measurements with the mDOM

The characterization of the intrinsic and environmental background of the mDOM is required for any quantitative interpretation of laboratory measurements and for the validation of the Geant4 mDOM simulations. This Chapter describes the background measurement procedure performed in a water tank setup in the basement, where the mDOM was operated under controlled environmental conditions in air and water. A complete understanding of the readout chain and a consistent calibration of the module at each temperature setting form the foundation for establishing a reliable measurement dataset in order to reliably compare it to simulations.

5.1 Experimental Setup

All measurements were performed in the institute's basement laboratory under controlled conditions. The room lights remained off during all acquisitions. Measurements were carried out with a design verification module (DVT), DVT09 (Haensel[1]), which belongs to a set of ten prototypes constructed prior to production to verify that all performance specification are met. All DVT modules are equipped exclusively with PMTs from earlier serial batches (serial numbers DM01130 and below, see Figure 3.7), whose intrinsic dark rates do meet the nominal performance specifications defined for the production modules (Appendix B).
The background was measured in two different configurations that probe the behavior of the module in water and air across a wide temperature range.

Water and Air Measurements at Room Temperature inside a Water Tank Setup

Room temperature measurements were performed in a rectangular water tank with internal dimensions 3.5 m $\times$ 1.7 m $\times$ 1.4 m. The interior surfaces are coated in matte black to suppress reflections, and the tank is enclosed by black roller shutters to ensure complete light tightness. The mDOM was placed in the tank using its harness and positioned close to one of the narrow side walls. This asymmetric placement defines a clear front and back orientation of the module: the PMTs on the backside face the nearby wall, whereas the frontside PMTs face the open tank volume. The orientation of the module was kept fixed for all room temperature measurements.

[1] All DVTs were labeled using German fairytale names.

Measurements were conducted inside the tank for both air (18 °C) and water (16 °C). For air, the tank remained empty except for the module; for water, the tank was filled with tap water until the mDOM was fully immersed. Figure 5.1 shows the measurement setup. The setup is commissioned to rotate the module and illuminate from arbitrary positions using the rotation motor and 3D moveable frame as seen on the right side for Figure 5.1 [42].

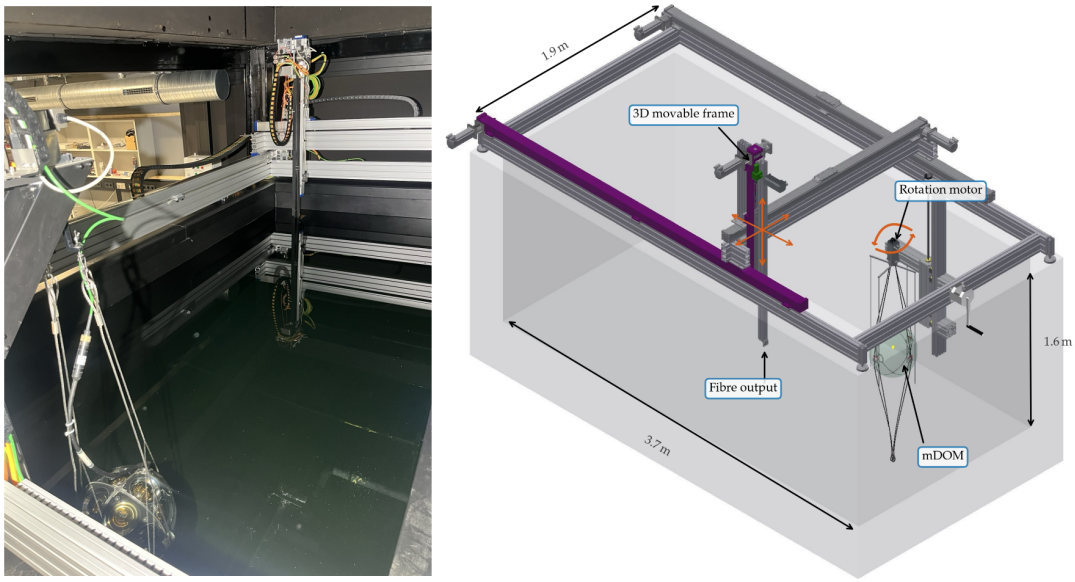

FIGURE 5.1: Measurement setup. Picture taken of the mDOM in water (left) and a rendering of the water tank (right). Taken from [42].

AIR MEASUREMENTS IN A FREEZER

For temperature measurements below 0 °C the mDOM was placed in a freezer in the same laboratory. To ensure light tightness, the module was wrapped in two opaque plastic bags and covered with black cloth. The freezer door remained closed throughout the acquisition. The angular orientation inside the freezer was not recorded, as it is not expected to influence the results, since intrinsic module background does not depend on the environment and atmospheric muons are not expected to bring a visible directional component in. All freezer measurement runs were performed in air.

5.2 CALIBRATION OF THE PMTS

Before background measurements can be taken, the responses of all PMTs must be calibrated to ensure that (i) the LED flashers operate in the single-photoelectron (SPE) regime, (ii) every PMT is set to the nominal operational gain of $G = 5 \times 10^6$, and (iii) the discriminator thresholds correspond to a well-defined photoelectron level [32, 28]. A consistent

calibration at each temperature setting is essential, as both gain and noise properties of the PMTs exhibit temperature dependence (see Equation 3.2). All calibrations were performed only after the module had reached thermal equilibrium; a minimum waiting time of 12 h was applied after each temperature change.
The subsequent calibration procedure followed the standard PMT calibration approach used in IceCube, as documented for example in [37] and described in detail in [32].

Single-Photoelectron (SPE) Illumination Level

The mDOM contains internal LED flashers that are used to illuminate the PMTs at low intensity. Emitted light of the LEDs reaches the PMTs due to internal reflections between the mDOM glass and the surrounding environment. To establish the SPE regime, the flasher bias voltage is scanned while recording the fraction of triggers above threshold for a single PMT. At low illumination levels, the hit probability follows a Poisson distribution and the operating point is chosen at a hit efficiency of approximately 10 %, corresponding to a mean illumination of $\mu \approx 0.1$ PE and negligible multi-PE contributions. Figure 5.2 top illustrates the SPE setting. This SPE illumination is used as the reference for the gain determination and the threshold calibration.

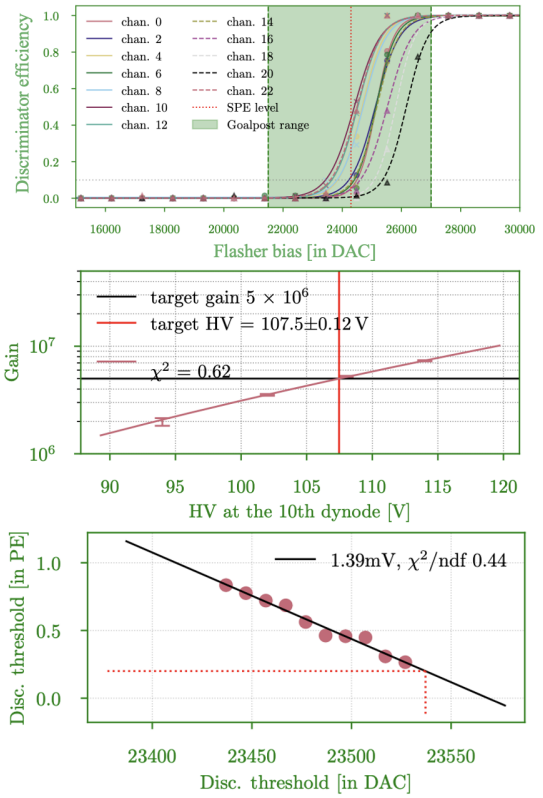

FIGURE 5.2: Example of a PMT calibration sequence. Top: calibration of the LED flasher chain. Middle: Single PMT gain calibration. Bottom: Discriminator threshold trigger calibration.

PMT Gain Calibration

With the SPE illumination fixed, the gain of each PMT is determined by acquiring SPE charge spectra at several high-voltage (HV) settings around the expected nominal operating region. For each HV point, the SPE peak is extracted from the charge histogram, and the resulting gain values are fitted with the standard power-law relation

$$G(U) = a\,U^k, \tag{5.1}$$

where U denotes the HV applied to the final dynode stage. The target HV for each PMT is the value of U for which the gain reaches 5×10^6. This procedure is depicted in Figure 5.2 middle and ensures uniform charge response across the module and compensates for PMT-to-PMT variations inherent to the production process.

DISCRIMINATOR-THRESHOLD CALIBRATION

The mapping between the discriminator digital-to-analog control value (DAC) and an equivalent threshold in PE units is obtained by operating the LED flashers in the SPE regime and scanning the DAC value, seen in Figure 5.2 bottom. The fraction of SPE pulses exceeding the threshold is recorded as a function of DAC, and the resulting curve is fitted with a linear model to extract the DAC value corresponding to a threshold of 0.2 PE. This setting ensures efficient detection of single photons while suppressing baseline fluctuations and electronic noise. The linearity of the DAC–to–PE relation is verified during the scan, and the same threshold-calibration procedure is repeated after each change in temperature.

5.3 READOUT AND DATA ACQUISITION

The data acquisition for the measurements was performed in waveform readout mode using discriminator triggering. Each waveform consists of a fixed number of digitized samples, which are recorded for every channel whenever a discriminator trigger occurs. The readout of waveforms is done in batches, in so-called blocks: during each acquisition block, consecutive waveforms from all PMTs are streamed continuously from the FPGA hit buffer, where they are temporarily stored in the onboard 2 Gbit DDR3-RAM buffer. This buffer is continuously filled by the FPGA and read out to the mainboard in predefined chunks, referred to as waveform blocks. Within each block, the data stream is continuous and no software-imposed deadtime occurs. To prevent hit-buffer overflow, the block size is limited. This is achieved by taking many smaller blocks. Blocks are acquired sequentially throughout a run. Between consecutive blocks, hardware- and software-based deadtimes can occur due to the trigger stream and the transfer of acquired data. These inter-block deadtimes are accounted for in offline analysis.
Within each waveform, several arriving photons can trigger a hit by exceeding the discriminator threshold. The readout stores all hits, even accounting for rapidly succeeding pulses within a single PMT's waveform. The digitization scheme of the analog and discriminator paths follows the AFE architecture described in Section 3. The discriminator stream sampled at 960 MHz supplies the rising-edge timestamps used to extract photon arrival times. For each discriminator edge, the timestamps are stored with a precision of $\sim$1 ns together with the corresponding PMT number.
It should be noted that the AFE channels are assigned different numbers than the PMT channels. For simplicity, all numbers shown in the following chapters refer to the PMT number.

6 Atmospheric Muon Flux

The atmospheric muon flux represents the dominant external background for all measurements performed with the mDOM in the laboratory introduced in Chapter 5. A determination of the absolute intensity and angular distribution at the mDOM environment is required as the building overburden and the surroundings modify the open-sky sea-level atmospheric muon flux and invalidate standard parameterizations of the form $I(\theta) \propto \cos^2\theta$ [9]. For a quantitative interpretation of the background detected by the mDOM and for the validation of Geant4 simulations, both an experimentally determined flux and a theoretically motivated estimation can provide the absolute normalization and the angular distribution of the particles injected into the simulation.
The objective of this Chapter is to measure the directional muon flux in the laboratory using a two-panel scintillation detector, identify true through-going muons via timing and signal-shape correlations, and derive the corresponding differential intensity after correcting for detector efficiency and geometrical acceptance. In addition, the atmospheric muon flux is theoretically calculated with the building overburden explicitly taken into account. The resulting fluxes serve as the reference normalization for the subsequent Geant4 simulation of the mDOM background and form the basis for all comparisons between measured and simulated multiplicity rate distributions.

6.1 Experimental Setup

The setup used to measure the atmospheric muon flux is shown in Figure 6.1. The detection system consists of two plastic scintillation panels operated in coincidence[1].
Each panel consists of an NE102A organic scintillator plate [43], chosen for its fast rise time of $\sim$ 1.4 ns and high light yield suitable for timing-based muon identification. In good approximation, each panel has the shape of an isosceles trapezoid with top width $a = 9.74$ cm, bottom width $b = 16.73$ cm, and height $h = 27.62$ cm, yielding an active area of $A = 365.5\,\mathrm{cm}^2$ per panel. Each scintillator is optically coupled to a Philips XP2972 PMT, operated at a bias voltage of 1500 V. At that operating point the PMTs exhibit a typical rise time of 2.1 ns and a typical transit-time spread (TTS) of 2.5 ns [34]. The corresponding single-PMT timing uncertainty,

$$\sigma_{\mathrm{PMT}} = \frac{\mathrm{TTS}}{2\sqrt{2\ln 2}} \approx 1.1\,\mathrm{ns},$$

sets a fundamental limit on the coincidence time resolution.
The panels are mounted parallel to each other with a fixed vertical separation of $d = 10.9$ cm.

[1] The detector was built as part of a bachelor's thesis project intended for educational demonstrations [43].

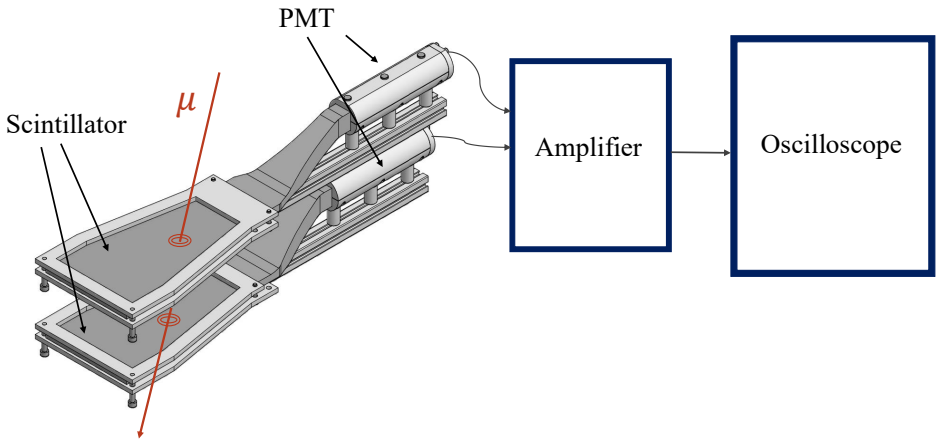

FIGURE 6.1: Schematic view of the coincidence rate measurement setup. Each scintillator is coupled to a photomultiplier tube, and the resulting pulses are amplified and sent to the oscilloscope.

The entire frame can be tilted to discrete zenith angles

$$\theta = 0^\circ,\ 22.5^\circ,\ 45^\circ,\ 67.5^\circ,\ 90^\circ,$$

thus enabling a measurement of the muon flux as a function of zenith angle.
Signals from both PMTs are amplified using a CAEN NIM 8306 fast amplifier. The amplified signals are digitized with a Teledyne LeCroy WaveRunner 8404M-MS oscilloscope with 4 GHz analog bandwidth and 40 GS/s sampling rate. Each waveform contains 1002 samples at 100 ps spacing, corresponding to a 100.2 ns acquisition window. A discriminator threshold of 5 mV suppresses electronic noise while ensuring sensitivity to minimum-ionizing muons. The panels are not hardware-triggered, all pulses above the threshold are recorded and the coincidence selection is performed offline using the extracted arrival times and pulse amplitudes.
For each triggered channel the full waveform is digitized, and two observables are extracted:

1. **Arrival time** t, defined as the time position of the waveform maximum. For every event, t_{upper} and t_{lower} denote the arrival times of the pulse maxima recorded in the upper and lower scintillator panels, respectively. The time difference

$$\Delta t = t_{\text{lower}} - t_{\text{upper}}$$

   is used to identify correlated muon events.

2. **Pulse amplitude** A, defined as the maximum value of the waveform. Likewise, A_{upper} and A_{lower} denote the pulse maxima measured in the upper and lower panels.

The amplitude difference

$$\Delta A = A_{\text{lower}} - A_{\text{upper}}$$

is used as an additional selection variable to reject accidental coincidences not produced by a single through-going muon.

6.2 Analysis

Time-difference selection

A through-going muon produces two signals separated only by its geometric time-of-flight and the detector timing resolution. The perpendicular muon path between the panels corresponds to a minimal time-of-flight of $(d/c) \approx 0.36\,\text{ns}$. Inclined muons increase the track length between the panels, with corner-to-corner trajectories yielding maximal time-of-flights of about $d/\cos\theta \approx 1.1,\text{ns}$. The detector timing resolution is dominated by the PMT transit-time spread and electronic jitter and is estimated as the overall expected coincidence width of approximately

$$\sigma_{\Delta t} = \sqrt{2}\sigma_{\text{PMT}} \approx 1.48\,\text{ns}.$$

A Gaussian fit to the measured Δt distribution returns the mean μ and width σ, which is slightly increased for the measured data.

$$\Delta t \in [\mu - 2\sigma,\ \mu + 2\sigma]. \tag{6.1}$$

Figure 6.2 shows on the left side a representative Δt distribution and the 2σ acceptance area of the measured data for $\theta = 0°$. All zenith angle data show a clear and well fitted Gaussian distribution. The absolute position of the Gaussian mean is determined by fixed channel-dependent delays in the PMTs, cabling, amplifiers, and oscilloscope inputs, and therefore does not correspond to the physical muon time-of-flight.

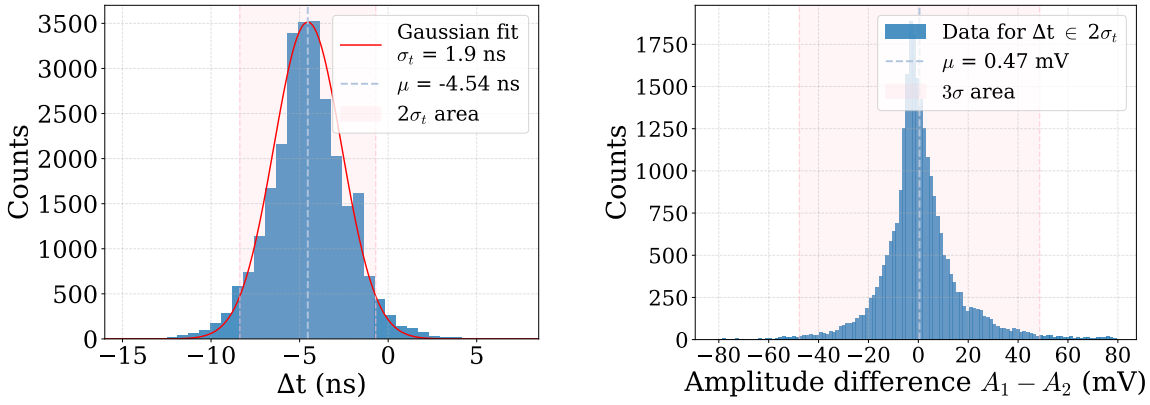

FIGURE 6.2: A representative time- and amplitude-difference selection for $\theta = 0°$.

AMPLITUDE-DIFFERENCE SELECTION

True muons deposit comparable energies in both scintillators, producing similar pulse amplitudes. In contrast, accidental coincidences often have large ΔA. For all events within the selected 2σ time window (Equation 6.1), the amplitude difference distribution is evaluated. Since the ΔA distribution shape is non-Gaussian with long tails from non-physical random coincidences, the empirical mean and standard deviation are used. Events are accepted if

$$\Delta A \in [\mu - 3\sigma,\ \mu + 3\sigma]. \tag{6.2}$$

On the right side of Figure 6.2 the ΔA distribution and the applied 3σ window is shown as an example for $\theta = 0°$.
Non-physical signals characterized by oscillatory structures are rejected. Figure 6.3 shows representative examples of oscillatory noise and a valid muon waveform.

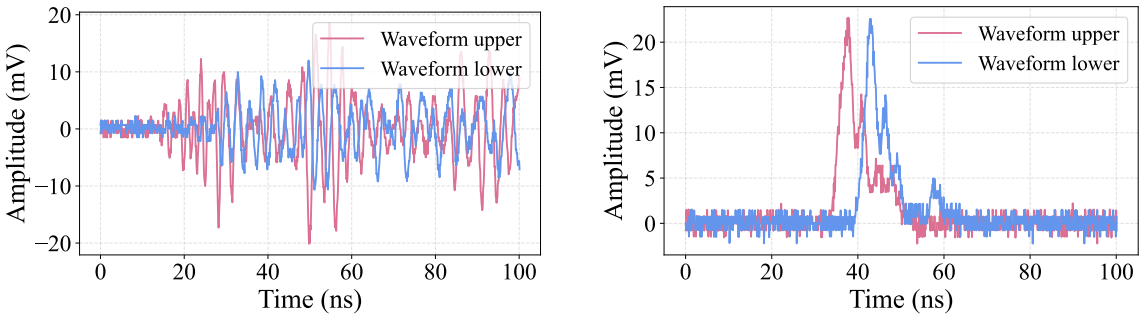

FIGURE 6.3: Oscillating waveforms rejected in the analysis (**left**) and an example of a though-going muon waveform in both panels (**right**).

COINCIDENCE RATE

After applying time and amplitude filtering, the coincidence rate at a given zenith angle is defined as

$$R_c(\theta) = \frac{N_{\text{coinc}}(\theta)}{T_{\text{meas}}}. \tag{6.3}$$

Here, $N_{\text{coinc}}(\theta)$ denotes the number of events that satisfy the coincidence criteria at the tile angle θ, and T_{meas} is the corresponding measurement time. To assess potential anisotropic shielding effects from the surrounding building, the detector was operated in two orthogonal orientations. As no measurable differences appeared, the data from both configurations were averaged.
To account for random uncorrelated coincidences, the background rates of both panels were measured independently. These background singles rates,

$$R_{B_1} = 235.8 \pm 7.5\ \text{min}^{-1}, \qquad R_{B_2} = 187.9 \pm 5.9\ \text{min}^{-1},$$

produce negligible accidental coincidences ($R_{acc} \sim 10^{-6}$ min^{-1}). The uncertainties are based on Poissonian distribution, and from systematic errors, which accounts for the trigger threshold choice, PMT gain drift, and a small dead-time uncertainty.
After subtraction the background single rates and averaging over the two orthogonal orientations of the setup, the coincidence rates are

$$\begin{aligned} R_c(0^\circ) &= (19.0 \pm 2.4)\,\text{min}^{-1}, \\ R_c(22.5^\circ) &= (17.0 \pm 2.4)\,\text{min}^{-1}, \\ R_c(45^\circ) &= (13.0 \pm 1.7)\,\text{min}^{-1}, \\ R_c(67.5^\circ) &= (7.5 \pm 1.0)\,\text{min}^{-1}, \\ R_c(90^\circ) &= (4.3 \pm 0.6)\,\text{min}^{-1}. \end{aligned} \tag{6.4}$$

The quoted uncertainties contain statistical and systematic contributions. The systematic component is obtained by varying the widths of the two coincidence-selection windows. For the time-difference selection the acceptance interval is defined as

$$\Delta t \in [\,\mu - k_t\,\sigma,\ \mu + k_t\,\sigma\,],$$

with the scale factor $k_t \in \{1.5,\ 2.0,\ 2.5\}$, where $k_t = 2.0$ corresponds to the nominal choice (Equation 6.1). Analogue, the amplitude-difference selection uses

$$\Delta A \in [\,\mu - m\,\sigma,\ \mu + m\,\sigma\,],$$

with $m \in \{2,\ 3,\ 4\}$, where $m = 3$ adopted as the nominal setting (Equation 6.2).

Detector Response

The coincidence response of the scintillation panels is described by a directional effective area $A_{\text{eff}}(\theta', \phi')$, which quantifies the probability that a muon arriving from a given direction (θ', ϕ') produces a valid coincidence in both scintillators. This acceptance is determined with a Monte-Carlo ray-tracing method implemented in Python using a HEALPix sampling of the whole sky. For each direction, muons are generated uniformly on a plane perpendicular to the incident direction and propagated as straight trajectories through the exact panel geometry. A trajectory contributes to A_{eff} only if it intersects both scintillator panels. The effective area is defined as

$$A_{\text{eff}}(\theta', \phi') = A_{\text{beam}} \frac{N_{\text{det}}}{N_{\text{emit}}},$$

with A_{beam} the area of the emitting plane and $N_{\text{det}}/N_{\text{emit}}$ the fraction of simulated trajectories producing a coincidence. This procedure yields a full-sky map of the directional coincidence acceptance. Figure 6.4 shows the resulting $A_{\text{eff}}(\theta', \phi')$, reflecting the panel geometry. The intrinsic efficiency of a single panel is taken as $\varepsilon_{\text{int}} = 0.90 \pm 0.10$, accounting for variations in light collection and PMT performance, resulting in an overall intrinsic efficiency of $\varepsilon_{\text{tot}} = \varepsilon_{\text{int}}^2 = 0.81 \pm 0.18$.

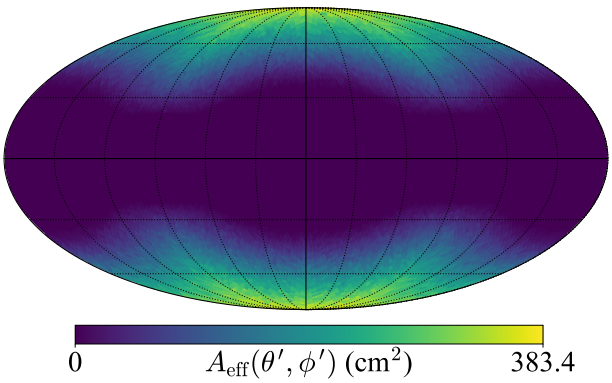

FIGURE 6.4: Effective are $A_{\text{eff}}(\theta', \phi')$ of the panel detector obtained from the Monte-Carlo ray tracing.

The atmospheric muon intensity is defined with respect to the laboratory zenith angle θ. For a detector tilt β, each direction (θ', ϕ') in the detector frame is transformed into the corresponding laboratory zenith angle via

$$\cos\theta(\beta) = \cos\beta\,\cos\theta' - \sin\beta\,\sin\theta'\cos\phi'. \tag{6.5}$$

Only directions with $\cos\theta > 0$ contribute to the downward muon flux.

For a given panel tilt β, the expected coincidence rate is obtained by integrating the directional muon intensity $I(\theta, \phi)$ over the upper hemisphere, weighted by the directional coincidence acceptance A_{eff} and the intrinsic efficiency ε_{tot}. This yields the rate as

$$R(\beta) = \int_0^{2\pi}\int_0^{\pi} I_0 \cos^n\theta(\beta, \theta', \phi')\, A_{\text{eff}}(\theta', \phi')\, \varepsilon_{\text{tot}}\, \sin\theta'\, \mathrm{d}\theta'\mathrm{d}\phi'. \tag{6.6}$$

Here, θ' and ϕ' are the directions defined in the detector frame, and $\theta(\beta, \theta', \phi')$ is the corresponding zenith angle in the laboratory frame after applying the tilt β.

DETERMINATION OF THE MUON INTENSITY

The parameters (I_0, n) describe the differential muon intensity,

$$I(\theta) = I_0 \cos^n\theta,$$

and are obtained by fitting Equation (6.6) to the measured coincidence rates at the five detector tilt angles β. The best-fit parameters are

$$I_0 = (12.2 \pm 1.3)\,\mathrm{m}^{-2}\,\mathrm{s}^{-1}\,\mathrm{sr}^{-1}, \qquad n = 1.3 \pm 0.2. \tag{6.7}$$

The fitted model reproduces the measured coincidence rates at all tilt angles with excellent consistency, as demonstrated by the agreement between the predicted and observed rates:

β (°)	R_{meas} (min^{-1})	R_{model} (min^{-1})
0	19.0 ± 2.4	19.3 ± 4.6
22.5	17.0 ± 2.4	17.5 ± 4.1
45	13.0 ± 1.7	12.6 ± 2.9
67.5	7.5 ± 1.0	7.0 ± 1.7
90	4.3 ± 0.6	4.5 ± 1.1

Figure 6.5 shows the measured coincidence rates together with the best-fit intensity model.

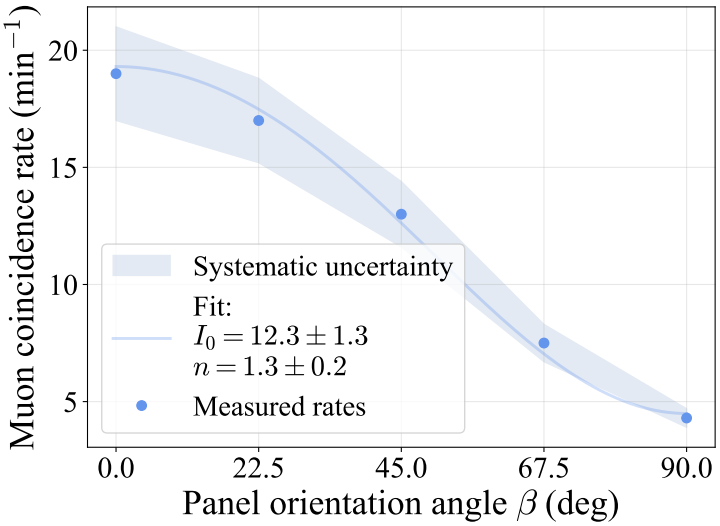

FIGURE 6.5: Measured muon coincidence rates as a function of the detector tilt angle β together with the best-fit differential intensity model $I(\theta) = I_0 \cos^n \theta$ for downward-going muons.

The statistical errors are smaller than the points, while the systematic uncertainty shown reflect the variation of the coincidence selection windows. The agreement between data and model over the full angular range illustrate the consistency of the fitted parameters and validates the Monte-Carlo acceptance calculation.

TOTAL MUON FLUX

The fitted intensity model can be integrated over the upper hemisphere. The total downward muon flux is

$$\Phi = 2\pi \int_0^{\pi/2} I_0 \cos^n \theta \, \sin\theta \, \mathrm{d}\theta = \frac{2\pi I_0}{n+1},$$

which yields

$$\Phi = (33.0 \pm 4.8)\,\mathrm{m}^{-2}\,\mathrm{s}^{-1}. \tag{6.8}$$

The resulting flux represents the the total downward muon flux, i.e. the total number of muons crossing a unit area per unit time, independent of their arrival direction. The standard open-sky parametrization $I(\theta) \propto \cos^2\theta$ yields $\Phi \approx 170\,\mathrm{m^{-2}\,s^{-1}}$ [9]. The reduction relative to the open-sky expectation reflects the shielding by the overlying building structure, while the fitted exponent $n = 1.3$ indicates a flatter angular dependence characteristic, which shallow-depth environments where vertically incident muons experience enhanced attenuation [12]. The observed flux is suppressed by a factor of five compared to the open-sky flux at sea level. This is a suppression observed in deeper laboratory sites [44]. Given the small size of the scintillation detector and the simplified setup, the muon flux might be underestimated. This gives motivation to calculate the muon flux at the measurement site taking the building into account.

6.3 ESTIMATED ATMOSPHERIC MUON FLUX IN THE LABORATORY

The laboratory is located in the basement of the Institute of Nuclear Physics in Münster at an altitude of 66 a.s.l [45] and mid-latitude. Altitude and latitude corrections are negligible for the energies dominating the local muon flux and amount to only a few percent.
For the flux estimation, the standard reference value for the total downward muon flux at sea level is used [9]:

$$\Phi_0 \simeq 1\ \mathrm{muon\,cm^{-2}\,min^{-1}} \approx 170\,\mathrm{m^{-2}\,s^{-1}}. \tag{6.9}$$

The angular distribution of the flux is parameterized as

$$I(\theta) \propto \cos^2\theta.$$

The building above the laboratory consists of seven concrete floors, each with an approximate thickness of 30 cm and a concrete density of $2.3\,\mathrm{g,cm^{-3}}$. A vertically incident muon ($\theta = 0°$) therefore encounters an areal density of

$$X_{\mathrm{vert}} \simeq 7 \times 0.30\,\mathrm{m} \times 2.3\,\mathrm{g\,cm^{-3}} \simeq 483\,\mathrm{g\,cm^{-2}}.$$

For non-vertical trajectories, the geometric path length through the building material increases as $1/\cos\theta$, while muons arriving at large zenith angles intersect fewer floors and may instead traverse the side wall. The effective overburden thus decreases with increasing zenith angle, and the attenuation model accounts for this by applying an angular weighting in which vertical muons experience the full overburden and inclined trajectories sample a reduced number of layers or the facade.
Using this simplified geometric model and a continuous ionization energy loss of approximately 2 MeV per $\mathrm{g\,cm^{-2}}$, the effective muon flux in the basement is

$$\Phi_{n=2} = (71.5 \pm 9.6)\,\mathrm{m^{-2}\,s^{-1}}, \qquad \Phi_{n=1.3} = (83.1 \pm 11.0)\,\mathrm{m^{-2}\,s^{-1}} \tag{6.10}$$

for the exponents $n = 2$ (open-sky) and $n = 1.3$. The uncertainty reflects the simplified building model; in particular, the effective path length is assumed to vary by ± 1 floor depending on the incident trajectory.
Assuming $n = 1.3$, the flux normalization is only reduced by a factor of about two compared to the open-sky flux from Equation 6.9.
The theoretic estimated laboratory atmospheric muon flux cannot reveal the correct angular distribution, and therefore the correct angular exponent for the flux at the laboratory. Comparing the theoretic calculated flux, $\Phi_{n=1.3} = (83.1 \pm 11.0)\,\mathrm{m}^{-2}\,\mathrm{s}^{-1}$, with the fit resulting flux of the measurement, $\Phi = (33.0 \pm 4.8)\,\mathrm{m}^{-2}\,\mathrm{s}^{-1}$, it shows that the scintillation panels cannot replicate the theory and shows a significant difference. On the other hand, the theoretical model provides only an approximate estimation.
For the input of the atmospheric muon flux into the Geant4 simulation in order to compare the mDOM background measurements with the simulation, both the measured, $\Phi = (33.0 \pm 4.8)\,\mathrm{m}^{-2}\,\mathrm{s}^{-1}$, and the theoretic estimated flux $\Phi_{n=1.3} = (83.1 \pm 11.0)\,\mathrm{m}^{-2}\,\mathrm{s}^{-1}$, will be used.

7 GEANT4 SIMULATION FRAMEWORK

Throughout this thesis the optical background of the mDOM is measured, and its quantitative interpretation requires a simulation that reproduces the relevant photon-production mechanisms, the detector response, and the geometrical boundary conditions of the experimental setup. A detailed model of the optical module and its environment is therefore implemented using the Geant4 Monte-Carlo toolkit.
Geant4 is a software toolkit developed at CERN to simulate the passage of particles through matter using Monte-Carlo methods [46]. It offers a comprehensive environment in which complex detector geometries, material properties, and particle sources can be defined, and in which a wide range of physics models, covering electromagnetic, optical, and hadronic interactions, are modeled over a broad energy range. Owing to its flexibility and extensibility, Geant4 has become a standard simulation tool in accelerator, medical, space and astroparticle physics. Its optical physics capabilities allow the user to specify refractive indices, absorption and scattering lengths, and to simulate the generation of transport of optical photons produces by Cherenkov radiation, scintillation or secondary interactions.

The simulations in this work are performed with OMSim (Optical Module Simulation), a Geant4-based framework developed within the IceCube group in Münster and extended in [28] based on two earlier PhD theses [6, 47]. It implements the complete mDOM geometry, including the borosilicate pressure vessel, optical gel, reflective cones, and the full 24-PMT arrangement, together with all optical interfaces and PMT response. Material properties—refractive indices, absorption and scattering lengths, scintillation yields and time constants—are mostly based on laboratory measurements. The surrounding water-tank geometry used in the measurements is included as well, enabling the simulation of photon propagation from intrinsic radioactivity and from atmospheric muons through the tank and into the module. A visualization of the simulated mDOM including its harness is shown in Figure 7.1. The support structure is simulated transparently.

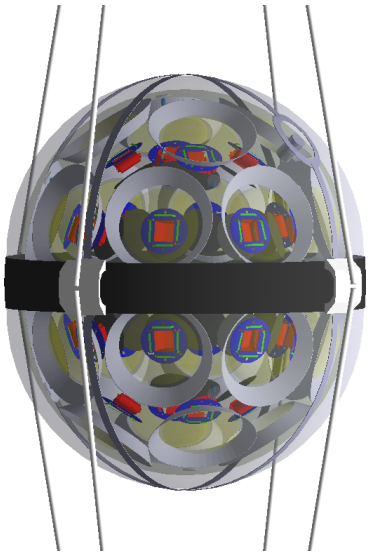

FIGURE 7.1: Visualization of the simulated mDOM in the OMSim framework. The support structure is transparent simulated.

7.1 SIMULATION OF RADIOACTIVE DECAYS IN THE MDOM

Radioactive decays in the mDOM are simulated in OMSim based on the measured isotope activities of the Vitrovex pressure-vessel glass listed again in Table 7.1. These activities determine the number of decays occurring in the module. For each simulation run, all decays expected within a user-defined time window t_w are generated and propagated through the module. For each decay chain (^{238}U, ^{235}U, ^{232}Th) and for ^{40}K, the number of decays in t_w

TABLE 7.1: Activity per mass of the three natural decay chains and ^{40}K measured Vitrovex glass. Data taken from [28].

Decay	Specific activity (Bq/kg)
^{40}K	60.98 ± 0.86
^{238}U chain	4.61 ± 0.07
^{235}U chain	0.59 ± 0.05
^{232}Th chain	1.28 ± 0.05

is calculated from the specific activity and the mass of the glass vessel. Each decay event begins by placing the parent isotope at a random position sampled uniformly within the glass volume. The subsequent decay products are emitted isotropically according to the decay model. If the isotope belongs to an active decay chain, the full sequence of daughter decays is simulated until a stable nuclide is reached. To ensure that all decays fall inside the simulated time interval, the decay time of each nucleus is sampled uniformly in $[0, t_w]$. This approximation reflects the assumption of secular equilibrium inside the glass and avoids extremely long natural lifetimes that are irrelevant for the short time scales of interest.

The emitted α particles, β-electrons and γ-rays are propagated using standard Geant4 electromagnetic processes. Their stepwise energy deposition generates scintillation and Cherenkov photons in the surrounding glass according to the material parameters defined in the mDOM model.
The temperature-dependent scintillation yields, emission spectra, and decay times used in the simulation are taken from the measurements summarized in Figure 4.2. Scintillation is implemented using an extended OMSim version of the standard Geant4 scintillation process. Separate yields are used for electrons (Y_e) and α particles (Y_α) to account for ionization-density–dependent quenching (see Section 4.2). The ratio Y_e/Y_α ranges from 1.5 (18 °C) to 1.8 (−40 °C). Cherenkov radiation is simulated for electrons above the threshold corresponding to the condition $\beta n > 1$, which in Vitrovex glass ($n \simeq 1.48$) gives $E_{\text{thr}} \approx 0.18$ MeV (Eq. 4.1).

All generated photons are propagated through the complete mDOM model, where each material is assigned its measured wavelength-dependent optical properties. Photon transport includes absorption, scattering, and boundary interactions, until the photons either

reach a PMT photocathode or are absorbed or exit the world volume[1]. Detected photons are stored with their timestamps corresponding to their arrival at the PMT. Table 7.2 summarizes the particles and physics processes active in the radioactive-decay simulation. The combination of the decay generation, electromagnetic particle transport through the module and optical processes provides a complete description of the intrinsic photon background produced inside the mDOM.

TABLE 7.2: Particles and physics processes required for the radioactive–decay simulation, together with the corresponding Geant4 classes.

Particle	Process	Geant4 class
Optical photon	Absorption	G4OpAbsorption
	Boundary processes	G4OpBoundaryProcess
	Mie scattering	G4OpMieHG
Ions	Scattering	G4hMultipleScattering
	Ionisation	G4ionIonisation
	Radioactive decay	OMSimRadioactiveDecayProcess
Alpha	Scattering	G4hMultipleScattering
	Ionisation	G4ionIonisation
Electron / Positron	Scattering	G4eMultipleScattering
	Ionisation	G4LivermoreIonisationModel
	Bremsstrahlung	G4eBremsstrahlung
	Cherenkov radiation	G4Cerenkov
	Positron annihilation	G4eplusAnnihilation
Gamma	Pair production	G4LivermoreGammaConversionModel
	Compton effect	G4LivermoreComptonModel
	Photoelectric effect	G4LivermorePhotoElectricModel
All ionizing particles (except optical photons)	Material scintillation	OMSimScintillationProcess

7.2 SIMULATION OF ATMOSPHERIC MUONS

The simulation of the atmospheric muon flux is implemented in OMSim to reproduce the conditions of the background measurements performed in the water tank, as described in Chapter 5. The implementation of the water tank geometry in OMSim follows the framework developed in a previous master thesis [48]. In the present work, the exact tank dimensions and the atmospheric muon flux derived in Chapter 6 were added to this setup. The full tank geometry, the optical properties of the medium, and the exact mDOM position and orientation inside the tank are replicated in the Geant4 simulation. The full

[1] In Geant4 the world volume encloses the entire detector setup. It defines the physical boundary of the simulation.

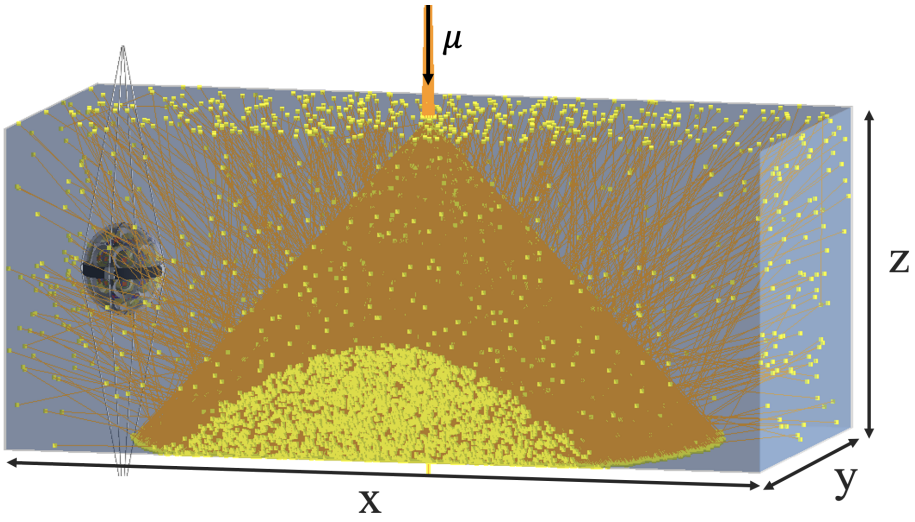

FIGURE 7.2: Water tank geometry in OMSim with the mDOM placed in water and a simulated atmospheric muon producing Cherenkov photons (orange: photon paths, yellow: interaction points).

mDOM geometry with its components and its harness are included with the same material and optical parameters used for the radioactive decay studies. A visualization of the setup is shown in in Figure 7.2 with a representive muon going through the water generating the characteristic Cherenkov cone.

The water tank is implemented as a rectangular volume with inner dimensions

$$x = 3.47\,\text{m}, \qquad y = 1.69\,\text{m}, \qquad z = 1.44\,\text{m}.$$

The mDOM is placed inside the tank at the same position and orientation of the PMTs as in the measurement. The tank walls are represented by a thin absorbing layer with low reflectance, and optical boundary interactions are handled via G4OpBoundaryProcess. Depending on the study, the tank is filled with either air or water. In water simulations, wavelength-dependent absorption is modeled using the coefficients from [49]. Scattering is neglected because the characteristic scattering length in water ($\mathcal{O}(300\,\text{m})$) is much larger than the typical photon path lengths ($\mathcal{O}(3\,\text{m})$) inside the tank [50].

To simulate atmospheric muons arriving from the upper hemisphere, primary muons are generated starting on a fixed horizontal circular disk placed above the water tank. The disk radius R_{disk} is chosen such that all sampled muon trajectories intersect the tank for zenith angles up to 80°[2]. Each muon direction (θ, ϕ) is sampled independently of the disk geometry. The starting point is drawn uniformly on the disk surface, ensuring unbiased sampling of the projected area for all arrival directions.
The zenith distribution follows the intensity parametrization of Equation 6.2. Converting

[2]For the specific tank dimensions and $R_{\text{disk}} = 12.74\,\text{m}$, $z = 2\,\text{m}$, the neglected flux fraction F in all muons with $80° - 90°$ is $F_{80-90} = \cos^{n_\mu+1}(80°)$, which corresponds to $\sim 1.8\,\%$ for $n = 1.3$. This value reflects a conservative upper bound, since only a subset of muons arriving between 80° and 90° would intersect the tank geometry.

this to a probability density over solid angle yields

$$p(\theta) = (n+1)\,\cos^n\,\theta\,\sin\theta,$$

from which inverse-transform sampling gives

$$\cos\theta = U^{1/(n+1)}, \qquad U \sim \mathcal{U}(0,1),$$

while the azimuth is sampled uniformly, $\phi \sim \mathcal{U}(0, 2\pi)$. Muon energies are drawn from the atmospheric muon flux parametrization obtained from [51], which reproduces the sea-level spectrum between 1 GeV and 10 TeV across all zenith angles.
The total number of muons generated in a simulation time window (T_{sim}) is determined from the integrated downward muon flux Φ and the disk area,

$$\langle N \rangle = \Phi\, A_{\text{disk}}\, T_{\text{sim}}, \qquad A_{\text{disk}} = \pi R_{\text{disk}}^2.$$

The actual number of muons is drawn from a Poisson distribution with mean $\langle N \rangle$, and their emission times are sampled uniformly in $t \in [0, T_{\text{sim}}]$.
All relevant electromagnetic and optical processes are activated during the simulation, listed in Table 7.3. Photons reaching a PMT photocathode are registered if they satisfy the wavelength-dependent quantum efficiency and angular acceptance of the PMT model. For each detected photon, the simulation records the PMT number and the global photon arrival time.

TABLE 7.3: Particles and physics processes included in the muon flux simulation, together with the corresponding Geant4 classes.

Particle	**Process**	**Geant4 Class**
Muon ($\mu^{\pm}$)	Multiple scattering	G4MuMultipleScattering
	Ionisation	G4MuIonisation
	Bremsstrahlung	G4MuBremsstrahlung
	Pair production	G4MuPairProduction
Charged particles	Cherenkov radiation	G4Cerenkov
	Scintillation	OMSimScintillationProcess
Optical photon	Absorption	G4OpAbsorption
	Rayleigh scattering	G4OpRayleigh
	Mie scattering	G4OpMieHG
	Boundary processes	G4OpBoundaryProcess

8 Simulation Calibration and Background Characterization

This chapter describes the methods used to characterize the background observed in the mDOM measurements and to calibrate the simulation accordingly. The measured datasets introduced in Chapter 5 contain superimposed contributions from trace radioactivity in the pressure vessel glass, atmospheric muons, intrinsic PMT dark noise, and afterpulsing. The simulation, in contrast, includes only the physical background sources from trace radioactivity in the glass and atmospheric muons, and therefore requires a consistent calibration before a quantitative comparison with the measurement can be performed in Chapter 9.
The following sections establish the separation of correlated and uncorrelated photon components, identify detector-specific background, and derive the corrections needed to align the simulation with the optical response of the specific module used in the measurements.

8.1 Time-Difference Analysis

To characterize the temporal structure of the background, the time difference between two consecutive hits of the same PMT is evaluated as

$$\Delta t_i = t_{i+1} - t_i.$$

For a purely random process with mean rate μ, the time intervals follow an exponential probability density,

$$p(\Delta t) = \mu\, e^{-\mu \Delta t}. \tag{8.1}$$

When expressed on a logarithmic scale, $\log_{10}(\Delta t)$, this transforms to

$$f(x) = \mu \ln(10)\, 10^x e^{-\mu 10^x}, \tag{8.2}$$

where $x = \log_{10}(\Delta t)$. The function exhibits a maximum at $x = -\log_{10}(\mu)$, such that the position of the peak directly reveals the uncorrelated rate μ of the underlying process.
Because Δt spans many orders of magnitude, the logarithmic representation separates the correlated from uncorrelated signal contributions (see Chapter 3). At large Δt (-3 to -1 $\log_{10}(\mathrm{s})$), the distribution follows the exponential behavior of independent processes such as intrinsic PMT dark noise or uncorrelated decays in the glass. At short Δt (-12 to -5 $\log_{10}(\mathrm{s})$), an excess appears, originating from correlated photon detections such as scintillation bursts, Cherenkov light, or PMT afterpulsings. Figure 8.1 shows a representative simulated Δt histogram of the background contributions in the mDOM placed in air, where both regions are visible. The sharp structures near -11 $\log_{10}(\mathrm{s})$ result from prompt

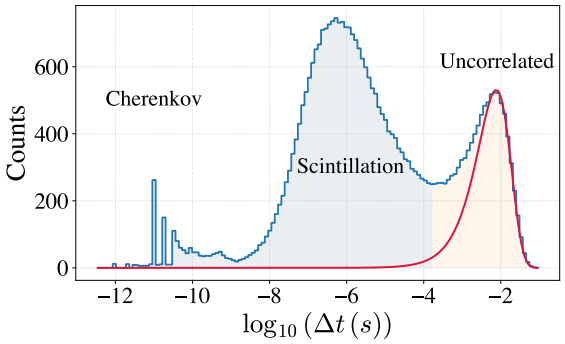

FIGURE 8.1: Example of a simulated Δt histogram illustrating the correlated Cherenkov and scintillation characteristic signal domains and the exponential uncorrelated component fitted with Equation 8.2. The fitted peak position $x = -\log_{10}(\mu)$ directly yields the uncorrelated dark noise rate μ.

Cherenkov photon arrivals. In the present simulation no TTS has been applied, such that the photon arrival times remain resolved and the prompt component appears as a narrow structure. In a real PMT, the broadening induced by the TTS and the limited timing resolution of the readout system prevent the separation of such closely spaced photons. Consequently, they merge into single pulses, suppressing these structures. The uncorrelated rate is modeled using a Poisson distribution as defined in Equation 8.2. It must be noted that the correlated region contains not only true physical correlations but also accidental temporal coincidences from statistically independent radioactive decays that happen to occur within short time separations.

PMT STABILITY IN MEASUREMENT DATA

For the subsequent calibration of the simulation, the per-PMT rates obtained from measurement and simulation are compared. While the simulation provides a statistically stable rate for each PMT, the measured rates can exhibit PMT-specific fluctuations. Therefore, the stability of all 24 PMTs across all measurement runs was evaluated to identify outliers in the total PMT rate.

During several measurement runs at different temperatures when the mDOM operated in air, individual PMTs exhibited anomalously high total background rates. The total rate of a PMT is defined as the number of recorded hits divided by the acquisition time. The spread of the PMT background rate of all 24 PMTs across all measured temperatures runs is shown in Figure 8.2. The left plot shows the absolute rate of all PMTs for each temperature. The right plots displays, for every temperature, the deviation of each PMT from the median rate of all PMTs recorded at the same temperature. Given the magnitude of these deviations, intrinsic PMT dark noise fluctuations cannot account for the observed spread[1]. These high-noise PMTs could be affected by temporary gain instabilities, calibration errors, or electronic noise pickup during acquisition. With the exception of PMT 3 at $-20\,^{\circ}\mathrm{C}$ and $-10\,^{\circ}\mathrm{C}$, all sub-zero datasets show similar behavior with slight fluctuations across all PMTs, whereas significant deviations across multiple PMTs at $0\,^{\circ}\mathrm{C}$ and room temperature are observed. To prevent them from biasing the mean PMT rate used for the

[1] Appendix F in [28] shows the temporal dark rate fluctuations of a DVT module.

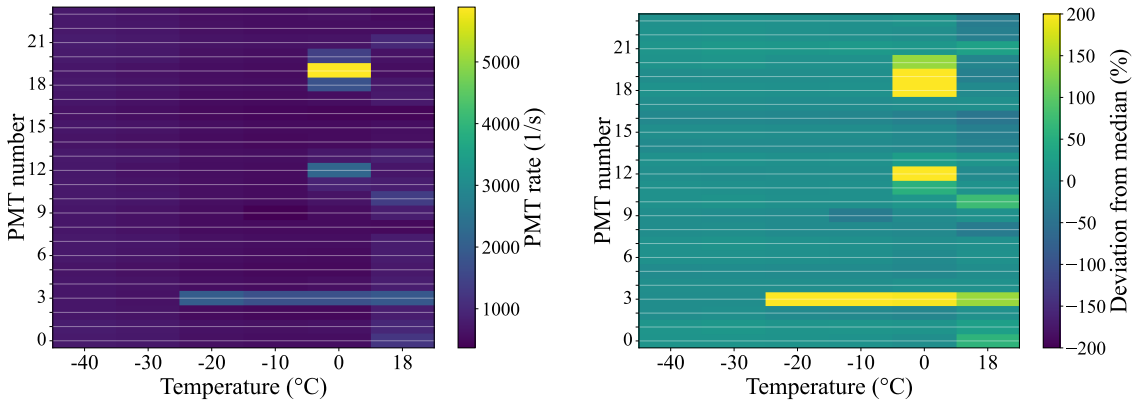

FIGURE 8.2: **Left**: Absolute total rates of all 24 PMTs for each temperature run. **Right**: Relative deviation of per-PMT rates from the median at each temperature.

following simulation calibration, all affected PMTs were excluded. The excluded PMTs are listed in Table 8.1. The rate spread $\Delta\mu_T = \mu_T^{\max} - \mu_T^{\min}$ listed in the table quantifies the per-temperature variation across all PMTs and directly reflects the magnitude of the instabilities that motivated their exclusion.

TABLE 8.1: List of PMTs excluded for the following simulation corrections due to anomalously high total rates, together with the difference between the largest and smallest measured rates $\Delta\mu_T = \mu_T^{\max} - \mu_T^{\min}$ at each temperature.

Temperature (°C)	**Excluded PMTs**	$\Delta\mu_T$ **(1/s)**
−40	–	160
−30	–	168
−20	3	1470
−10	3	1348
0	3, 11, 12, 18, 19, 20	6243
+18	0, 3, 10	1421

For the sake of completeness, Figure 8.3 shows the PMT stability from the averaged measurements when the mDOM was placed in water. For these measurements, the PMTs were relatively stable. The observed pattern across all PMTs reflects the expected angular dependence of Cherenkov emission in the water volume. PMTs oriented toward the tank interior receive a higher photon flux, whereas PMTs facing the nearby tank wall are exposed to a reduced optical path and consequently register lower rates. This will be discussed in Chapter 9.

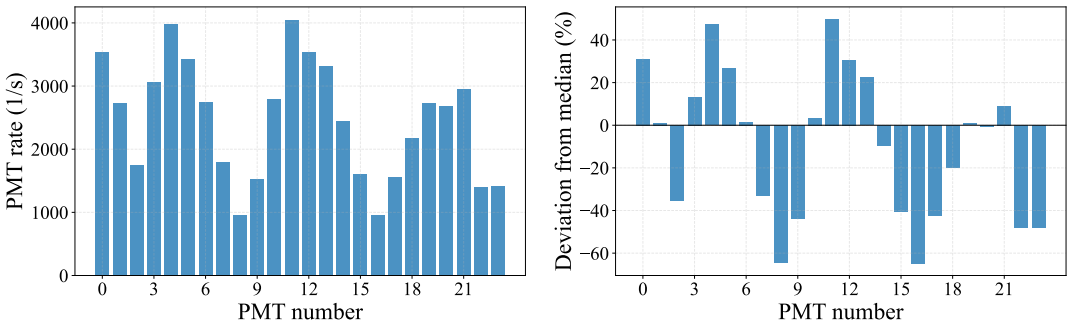

FIGURE 8.3: Absolute PMT rate and per-PMT deviations relative to the median rate, measured in water at 16 °C.

8.2 EXTRACTION OF CORRELATED AND UNCORRELATED RATES

The time difference analysis described in Section 8.1 was applied identically to all measurement datasets and simulation outputs. A dead time of 10 ns was imposed on each PMT in both cases to enforce a consistent hit definition. This value corresponds to the pulse-pair resolution required for mDOM PMTs, which must be able to resolve individual pulses only if they are separated by at least 10 ns [25]. Pulses arriving within this interval cannot be distinguished in the measurement and therefore must not be treated as independent hits in the simulation. For each dataset the Δt distributions were computed separately for all 24 PMTs and subsequently averaged to obtain a single Δt histogram per temperature, which was then averaged over repeated runs at the same temperature.
The uncorrelated pulse region at large Δt was fitted with Eq. 8.2, yielding the uncorrelated rate μ_U. The total mean rate per PMT,

$$\mu_T = \frac{N_{\text{hits}}}{T_{\text{acq}}},$$

was obtained from the total number of hits N_{hits} and the total acquisition time of measurement and simulation, respectively, T_{acq}. From this, the correlated rate directly follows as

$$\mu_C = \mu_T - \mu_U. \tag{8.3}$$

Figure 8.4 shows the resulting Δt histograms with the Poisson fit for the uncorrelated rate μ_U from simulation (left) and measurement (right). This case is shown when the mDOM operates in air at temperatures between -40°C and $+18$°C. Both plots are limited to $-8\ \log_{10}(\text{s})$, reflecting the applied 10 ns dead time. It has to be noted that the simulation in this plot covers a total acquisition time of $T_{\text{acq}} = 120$ s, where as the measurement spans $T_{\text{acq}} = 260$ s, the absolute event counts in both panels are not directly comparable. In the simulation (left), both correlated and uncorrelated components decrease with increasing temperature. At low temperatures, the correlated peak at short Δt is significantly higher, consistent with a greater scintillation yield, as described in Chapter 7. At warmer

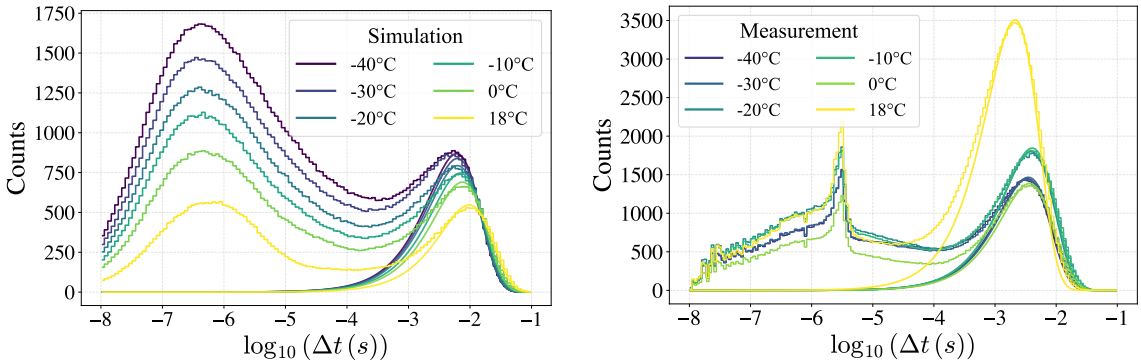

FIGURE 8.4: Average Δt PMT histograms from simulation (**left**) and measurement (**right**) for the mDOM in air at different temperatures. Both plots show per-PMT averages and the uncorrelated rate μ_U is fitted with a Poissonian (Equation 8.2).

temperatures both the correlated and uncorrelated components decrease. For the uncorrelated part, the exponential tail shifts towards larger Δt, consistent with a reduced uncorrelated rate μ_U , since the mean waiting time of a Poisson process satisfies $\langle \Delta t \rangle_R = 1/\mu_U$. The changing ratio between the two peaks visualizes the temperature dependence of the simulated optical processes. In contrast, in the measured data (right), a similar overall structure is observed, but the uncorrelated peak is much more pronounced relative to the correlated peak. This results from thermionic dark noise intrinsic to the PMTs, which is absent in the simulation. The uncorrelated peak converges and narrows towards low temperatures, while at 0°C and especially at 18°C, the uncorrelated peak rises sharply, reflecting the underlying strong temperature dependence of the intrinsic PMT dark noise (see Equation 3.2). Furthermore, a distinct excess around -6 $\log_{10}(\mathrm{s})$ appears in all measurements but is absent in the simulation, reflecting PMT afterpulsing ($\mathcal{O}$(µs) with 5.65 % probability [36]) , which is not included in the simulation.
The identical extraction of μ_U for measurement and simulation under the same dead time conditions establishes the basis for a direct comparison of μ_C and μ_U in the next sections.

8.3 Correction of Detector-Specific Background

The comparison between the correlated rates μ_C^{sim} and μ_C^{meas} extracted in the previous section provides direct sensitivity to the scintillation parameters implemented in the simulation (Figure 4.2). These parameters originate from measurements performed in [28, 35] using a limited number of Vitrovex glass samples and showed substantial batch-to-batch variations [35]. Consequently, the parameters set in the simulation may not represent the glass composition of the DVT09 module used in this work.

8.3.1 AFTERPULSING CORRECTION

Before comparing μ_C^{sim} with the measured correlated rate μ_C^{meas}, the contribution from PMT afterpulsing must be removed from the measurement data, as afterpulses are not simulated. The temperature dependent afterpulsing probabilities are taken from detailed PMT characterizations conducted in [52] and are visualized as the early (I) and late (II) afterpulsing in Figure 8.5. The total afterpulsing probability,

$$P(\text{AP}) = P(\text{API}) + P(\text{APII}),$$

provides the fraction of correlated pulses in μ_C^{meas} that originate from afterpulsing rather than from physical photon processes. Scaling the measured correlated rate by this probability yields the afterpulsing–corrected correlated rate $\mu_C^{\text{meas}^*}$, which is directly comparable to μ_C^{sim} and forms the basis for the scintillation yield calibration in the following section.

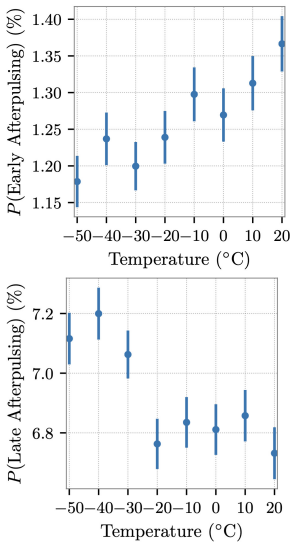

FIGURE 8.5: Probability of early and late afterpulsing as a function of temperature for a mDOM PMT. Taken from [35].

8.3.2 SCINTILLATION YIELD CORRECTION

The correlated rates μ_C are obtained directly from the total rate μ_T and the fitted uncorrelated rate μ_U (Equation 8.3), with μ_U taken from the fit defined in Equation 8.2. The direct comparison in the sub-zero regime between μ_C^{sim} and afterpulsing-removed $\mu_C^{\text{meas}^*}$ is shown in Figure 8.6 at different temperatures and revealed that the simulated values were systematically higher and exhibited a steeper temperature dependence than those measured. The excess rates stemming from scintillation induced by radioactive decays in the pressure vessel are strongly temperature dependent and dominate in the sub-zero regime, whereas the intrinsic PMT dark noise rises exponentially with increasing temperatures. The linear fits quantify the mismatch, yielding slopes of $a_{\text{sim}} = -9.38 \pm 0.57\,(\text{s}\,^\circ\text{C})^{-1}$ and $a_{\text{meas}} = -3.86 \pm 0.19\,(\text{s}\,^\circ\text{C})^{-1}$. This deviation between μ_C^{sim} and $\mu_C^{\text{meas}^*}$ indicates that the scintillation parameters implemented in the simulation framework overestimate the actual scintillation yields of the specific Vitrovex glass sample used in the measured DVT09 module. To adjust the simulation to match the measurement output, μ_C^{sim} and $\mu_C^{\text{meas}^*}$ can be used to determine a temperature dependent correction factor for the scintillation yield Y. The correction factor

$$f(T) = \frac{\mu_C^{\text{meas}^*}(T)}{\mu_C^{\text{sim}}(T)}$$

was determined for sub-zero temperatures (-40°C to -10°C), where scintillation dominates, and linearly interpolated between these points. The factor was applied multiplicatively to the electron- and alpha induced scintillation yield parameters Y^{α,e^-} in the simulation,

$$Y_{\text{corr}}^{\alpha,e^-}(T) = f(T)\, Y_{\text{orig}}^{\alpha,e^-}(T),$$

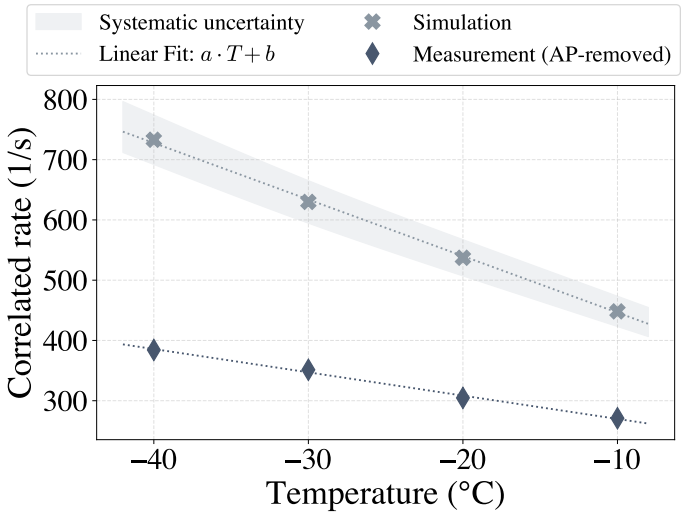

FIGURE 8.6: Comparison of correlated rates from measurement (after afterpulsing correction) and simulation before yield correction.

ensuring that the simulated photon yield follows the same relative temperature dependence as the measured data.
Figure 8.7 illustrates the correction for both alpha and electron induced yields. The applied temperature dependent correction reduces the simulated α and e^- induced scintillation yields by roughly 50 % at $-40°$C. The corrected yields were extrapolated to room temperature because the measurements of the scintillation parameters were only performed up to $-15°C$. The linear extrapolation provides the best available estimate. However, this assumption has to be treated with caution, as light yield could also follow a non-linear behavior due to quenching mechanism (see Section 4.2). Increasing temperature can open additional non-radiative relaxation paths in the glass that reduce the effective scintillation yield. For a realistic simulation comparable to module specific measurements, the scintillation parameters need to be measured at all temperatures.

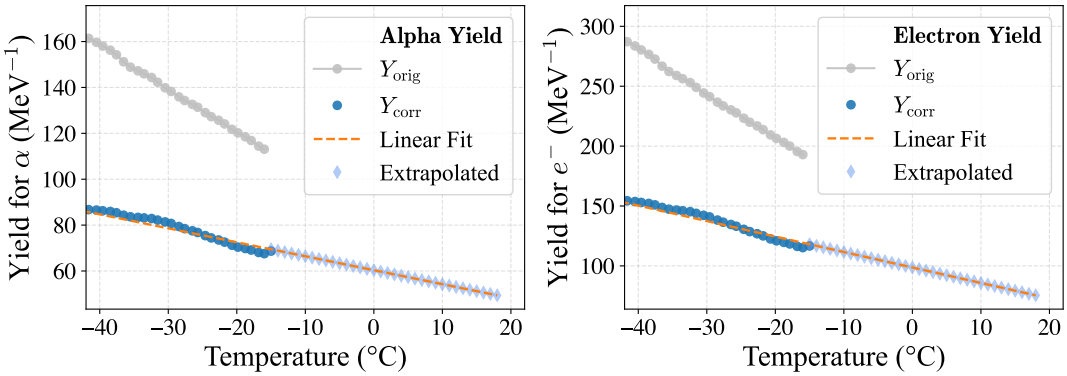

FIGURE 8.7: Temperature dependent correction applied to the simulation scintillation yields for alpha and electron induced processes.

After correction, the simulation was repeated and the Δt analysis, comparing μ_C^{sim} and afterpulsing-removed $\mu_C^{meas^*}$, was performed again. This procedure was done iteratively;

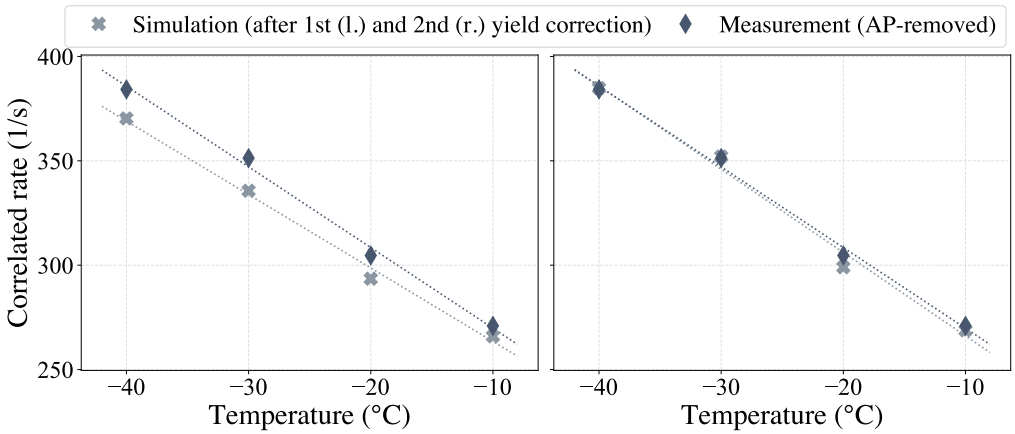

FIGURE 8.8: Comparison of correlated rates between measurement and simulation after applying the temperature dependent scintillation yield corrections.

after two iterations the agreement in both slope and absolute rate level was achieved, confirming that the corrected scintillation yields accurately reproduce the optical behavior of the specific DVT09 module. Figure 8.8 illustrates this process, showing on the left side the corrected simulation output after the first application of $f(T)$ and on the right the output after the second correction. In both plots $\mu_C^{\text{meas}^*}$ stays the same.
The Δt distribution after applying the yield correction is shown in Figure 8.9. In comparison to Figure 8.4 (left) before the yield correction, the relative heights of the two peaks change primarily for the sub-zero temperature curves. The yield correction reduces the strong temperature dependence observed before, aligning the overall amplitudes and slightly modifying the relative prominence of the correlated and uncorrelated peaks.

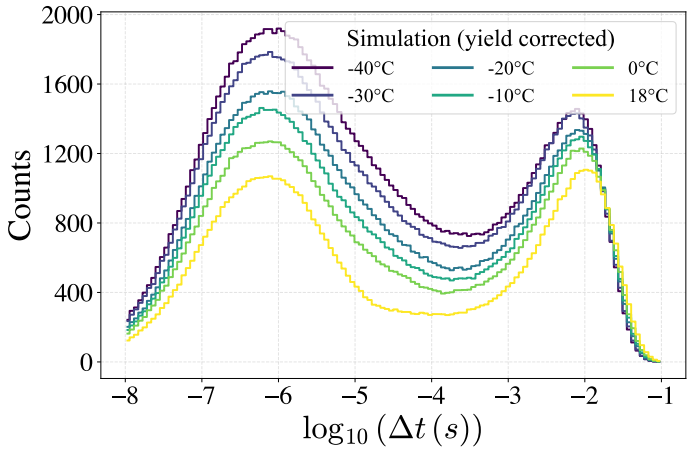

FIGURE 8.9: Yield corrected Δt histograms for the simulation outputs.

The adjustment of the scintillation yields serves as the basis for all further analysis steps. In the following, all references to simulated outputs imply yield corrected simulations. This correction establishes a consistent basis for comparing measurement and simulation. It was, however, derived under the assumption that the correlated rate is entirely driven by

scintillation light output, neglecting any contribution from intrinsic PMT dark noise. Some residual contamination may remain even at low temperatures because intrinsic PMT dark noise cannot be removed entirely from the correlated peak. Nevertheless, the yield correction was performed only for temperatures between $-40\,^{\circ}\mathrm{C}$ and $-10\,^{\circ}\mathrm{C}$, where it provides a sufficiently accurate approximation.
A comparison between measurement and simulation in Chapter 9 demonstrates that the applied yield correction produces a consistent description of the PMT rates. In summary, the temperature dependent yield adjustment establishes a physically coherent optical response for the DVT09 glass and defines the calibrated simulation baseline used in the subsequent analysis.

8.3.3 Intrinsic PMT Dark Rate Estimation

In the previous section, the simulation was adjusted to match the scintillation properties of the specific DVT09 module used for the background measurements. Moreover, intrinsic PMT dark noise needs to be investigated, as it has a huge impact on the uncorrelated rates μ_U, and consequently on the total PMT rates μ_T. In order to quantify the module specific intrinsic PMT dark noise rate $\mu_{\mathrm{DR}}^{\mathrm{PMT}}$ the fitted uncorrelated afterpulsing-removed rates $\mu_U^{\mathrm{meas*}}$ and $\mu_U^{\mathrm{sim,\,YC}}$ resulting from the the yield corrected simulation output are subtracted:

$$\mu_{\mathrm{DR}}^{\mathrm{PMT}}(T) = \mu_U^{\mathrm{meas*}}(T) - \mu_U^{\mathrm{sim},YC}(T). \tag{8.4}$$

This is justified because both measurement and simulation contain the uncorrelated component from radioactive decays in the glass, while only the measurement contains intrinsic PMT dark noise. Subtraction therefore isolates the PMT dark noise rate. The obtained rates are listed in Table 8.2. The uncertainties are dominated by the PMT-to-PMT spread of the measured uncorrelated rates.

Table 8.2: Intrinsic PMT dark rates estimated as the difference between the measured and simulated uncorrelated rates, $\mu_{\mathrm{dark}} = \mu_U^{\mathrm{meas}} - \mu_U^{\mathrm{sim}}$.

Temperature (°C)	$\mu_{\mathrm{DR}}^{\mathrm{PMT}}$ **(1/s)**
$+18$	348.4 ± 107.3
0	210.2 ± 40.8
-10	137.4 ± 15.1
-20	138.7 ± 14.6
-30	161.5 ± 14.1
-40	179.7 ± 15.5

The separated view of the uncorrelated and correlated components is shown in Figure 8.10 across all temperatures. The left bars correspond to the measurement, and the right bars to the simulation. The left plot displays the uncorrelated rates extracted from measurement and simulation. By construction, they agree at all temperatures, since the intrinsic PMT dark rate $\mu_{\mathrm{DR}}^{\mathrm{PMT}}(T)$ is obtained directly from the difference of the uncorrelated components

fitted according to Equation 8.4, and is explicitly added to the simulation. The resulting match therefore reflects the internal consistency of the extraction procedure. Towards warmer temperatures, μ_U^{meas} rises steeply due to the exponential temperature dependence of thermionic emission (Equation 3.2).
The right plot shows the correlated component, which reflects scintillation induced by radioactive decays in the pressure vessel glass. After applying the temperature dependent yield correction, the simulation reproduces both the absolute scale and the temperature trend of the sub-zero measurements. At 0 °C and 18 °C, μ_C^{meas} is biased upward because thermionic dark noise leaks into the short-Δt region and contaminated the correlated peak, while the simulation remains unaffected. On the other hand, the scintillation parameters were extrapolated to room temperatures, assuming a linear dependency of the yield. This might not be true and could also bias the rates.

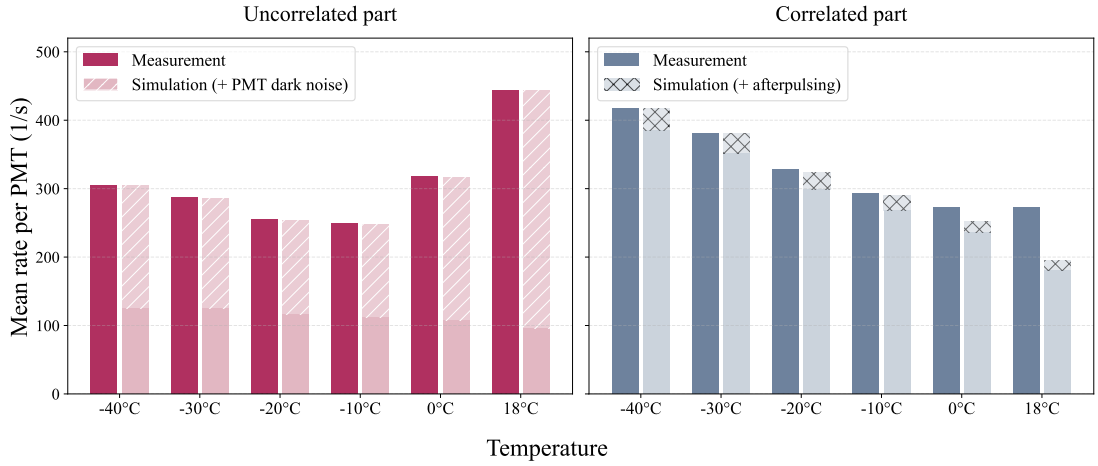

FIGURE 8.10: Uncorrelated (**left**) and correlated (**right**) PMT rates from measurement and simulation. The uncorrelated components match by construction through the intrinsic dark-rate extraction in Equation 8.4. The correlated rates agree in the sub-zero regime after applying the scintillation-yield correction. The corresponding total PMT rates are listed in Chapter 9 in Table 9.1.

The combined analysis of the Δt distributions, the exclusion of unstable PMTs, and the temperature dependent calibration steps establishes a consistent simulation foundation for comparing measurement and simulation. The yield correction aligns the simulated scintillation component with the sub-zero measurements with the specific DVT09 module, while the intrinsic PMT dark rate obtained from the uncorrelated tails ensures agreement of the uncorrelated background across all temperatures. For comparison between measurement and simulation, the afterpulsing and the intrinsic PMT dark noise rates have to be taken into account, as they are absent in the simulation.

8.4 Simulation Based Background Component Analysis

The previous sections established the separation of correlated and uncorrelated background components in data, enabling the recalibration of the scintillation yields in the simulation and the extraction of the intrinsic PMT dark noise. However, the measurement always records a superposition of all underlying physical processes, and the individual contributions from atmospheric muons, intrinsic radioactivity, and detector-specific effects appear as a convolution of overlapping photon emissions. Because their temporal and spatial signatures partially overlap, the individual processes cannot be disentangled experimentally.
In contrast, the simulation allows each physical process to be enabled independently. The following section therefore considers simulation-only datasets, where the atmospheric muon component and the intrinsic radioactivity of the glass are isolated and analyzed separately. This establishes the physical baseline required for interpreting and comparing the measurement with the full simulation in Chapter 9.

Background Coincidence Rates

The total PMT rate μ_T provides no information on the spatial correlations among the PMTs of the mDOM. To resolve the correlations, the background is evaluated in terms of local coincidences (LC) within a fixed time window Δt_{LC}. For each photon hit at time t_i, a coincidence window $[t_i,\ t_i + \Delta t_{\mathrm{LC}}]$ is opened, and all subsequent hits within this interval are assigned to the same window, thus to the same LC event. The multiplicity m of a window is defined as the number of unique PMTs that registered at least one hit within this interval. To avoid double counting of the same activity, non-overlapping windows are implemented. A new window is opened by the first hit occurring after the previous window has closed. For each dataset, the coincidence rate $R(m)$ is obtained from the number N_m of coincidence windows with multiplicity m normalized to the total duration time T_{acq}:

$$R(m) = \frac{N_m}{T_{\mathrm{acq}}}.$$

The coincidence spectrum $R(m)$ characterizes the spatial structure of the background processes. Low multiplicities originate from uncorrelated or localized sources such as intrinsic PMT dark noise or single radioactive decays in the glass. Higher multiplicities reflect bright light sources, in particular atmospheric muons or scintillation bursts involving multiple PMTs. No temperature dependence is applied to the atmospheric muon component and it is therefore simulated with a temperature-independent flux, as neither the muon flux nor the Cherenkov yield nor the water conditions change with the module temperature, while air scintillation is negligible.

8.4.1 ATMOSPHERIC MUONS BACKGROUND

In this section, the influence and expectations of the atmospheric muon component are discussed for which both investigated environments (i.e. air and water) are treated separately. The underlying processes are identical, but their relative impact differs substantially.

IN AIR

In an air environment, photons are generated solely by the propagation of atmospheric muons through the module's glass vessel. The contribution from air scintillation is considered negligible; the same applies to Cherenkov emission. Consequently, any muon passing outside the glass sphere of the mDOM does not result in PMT pulses.
The optical properties of the glass ($n_{\text{glass}} \approx 1.48$) and gel ($n_{\text{gel}} \approx 1.41$) inside the mDOM allow for Cherenkov emission from muons with energies as low as $\approx 150\,\text{MeV}$[2], far below the mean energy of atmospheric muons at the surface ($\approx 4\,\text{GeV}$) [53], which means that every muon traversing the mDOM produces Cherenkov photons. The dominant interaction is continuous ionization, through which the muon deposits energy and creates secondary electrons along its track throughout the mDOM. These secondary electrons can themselves emit additional Cherenkov photons, thereby increasing the overall photon yield and slightly widening the emission cone. The ionization energy loss of the muon and its secondaries also excites the glass molecules, producing a small amount of isotropic scintillation light. This scintillation component is much weaker than the Cherenkov signal.
Radiative processes such as muon bremsstrahlung and pair production remain negligible. These effects become significant only at TeV energies[3] or in much thicker materials (see Figure 2.3) [14]. The continuous ionization losses are approximately $2\,\text{MeV}\,\text{cm}^{-1}$ in glass and gel, corresponding to a few MeV across the module diameter. Contributions from the thin PMT glass envelopes are marginally as well compared to the thickness of 13.5 mm and overall volume of the pressure vessel of the mDOM [32].

IN WATER

When the mDOM is operated in water, the same physical processes remain, but their relative contributions change. The effective muon induced photon yield increases significantly because Cherenkov emission also occurs in the surrounding medium ($n_{\text{water}} \approx 1.33$), where the Cherenkov angle is larger ($\theta_C \approx 41°$) (Equation 2.1). Consequently, muons that do not traverse the mDOM directly can still illuminate several PMTs simultaneously, generating high-multiplicity local coincidences.

[2] The Cherenkov threshold follows from $\beta_{\text{thr}} = 1/n$, $\gamma_{\text{thr}} = \frac{1}{\sqrt{1-\beta_{\text{thr}}^2}}$, $E_{\text{thr}} = \gamma_{\text{thr}} m_\mu c^2$.

[3] Though, energies up to 10 TeV are simulated, the spectrum follows $E^{-2.7}$, and therefore the mean energy is still in the few-GeV range.

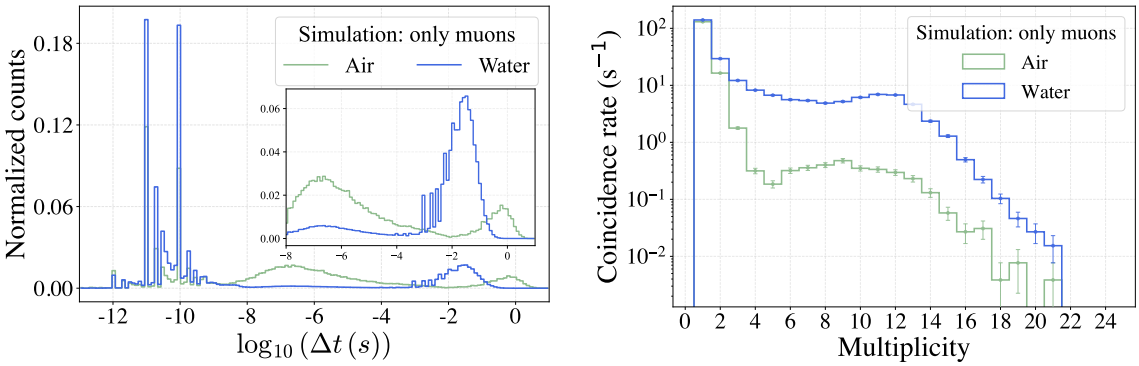

FIGURE 8.11: **Left:** Normalized Δt distributions for simulations including only atmospheric muons in air (green) and in water (blue). **Right:** Corresponding coincidence rate with applied PMT deadtime.

The optical coupling between the glass and water increases the critical angle for total internal reflection from $\theta_{c,\text{air}} \approx 43°$ to $\theta_{c,\text{water}} \approx 64°$[4]. This reduces internal photon trapping in the mDOM and allows a larger fraction of photons to escape into the surrounding water. As a result, fewer internally reflected photons reach the PMTs and the time distribution of detections becomes narrower.

Figure 8.11 illustrates these effects. The normalized Δt distributions exhibit a prompt Cherenkov peak around $-10\ \log_{10}(\text{s})$, largely suppressed in the analysis by the applied PMT deadtime of 10 ns; the zoomed in plot shows the contribution relevant to the analysis. In air, additional structures around $-6.6, \log_{10}(\text{s})$ (250 μs) arise from photons trapped by total internal reflection inside the glass, together with a small scintillation contribution. This mid-Δt feature is strongly reduced in water because photons escape the pressure vessel more efficiently. Total internal reflection occurs about 1.7 times more frequently in air than in water [54]. For even larger time differences (ms to s), the distributions enter the uncorrelated regime of the atmospheric muon background. These late-Δt contributions do not originate from delayed optical propagation but reflect the Poissonian waiting-time distribution of independent muon arrivals.
The coincidence rates (right side) show the simulated general behavior between the module's environment. Operation in water results in a shift toward higher multiplicities m and increased event rates, attributed to Cherenkov radiation triggering multiple PMTs within the 50 ns coincidence window. The average per-PMT rates caused by the muons are:

$$\begin{aligned} \text{No PMT deadtime:} \quad & \bar{\mu}^{\text{muon}}_{\text{T,air}} = 39.6 \pm 8.3\ \text{s}^{-1}, \qquad \bar{\mu}^{\text{muon}}_{\text{T,water}} = 318.3 \pm 159.3\ \text{s}^{-1}, \\ \text{10 ns PMT deadtime:} \quad & \bar{\mu}^{\text{muon}}_{\text{T,air}} = 9.1 \pm 1.4\ \text{s}^{-1}, \qquad \bar{\mu}^{\text{muon}}_{\text{T,water}} = 34.2 \pm 12.7\ \text{s}^{-1}. \end{aligned} \tag{8.5}$$

The uncertainties stem from the standard deviation σ. The large spread in water reflects the directional nature of Cherenkov emission and the asymmetric orientation of the mDOM within the water tank (Figure 5.1). The results are shown for the cases with and

[4]The critical angle is given by $\sin\theta_c = n_2/n_1$ for an interface with $n_1 > n_2$.

without applied PMT deadtime. The strong suppression due to the deadtime demonstrates that most of the photon hits stem from early Cherenkov burst.
Instead of monotonically decreasing with increasing m, the rate shows an intermediate multiplicity accumulation. These plots serve to illustrate the overall expected behavior of the influence of muons to the coincidence rate of the mDOM. A further detailed analysis is discussed in Chapter 9 when the simulation output is compared to measurement results.

8.4.2 SCINTILLATION INDUCED BY TRACE RADIONUCLIDES

This section shows the simulated behavior of the radioactive decays within the pressure vessel glass of the mDOM.
In contrast to the muon background, the steady internal background originates from radioactive decays in the pressure vessel glass of the mDOM. The α, β, and γ emissions from the natural decay chains deposit energy in the glass and induce scintillation and, for sufficiently energetic electrons, Cherenkov light as described in Chapter 4. Photons are emitted isometrically and occur on nanosecond to microsecond timescales, producing the correlated excess seen the Δt distributions.

IN WATER

In a water environment, the radioactivity originating from trace amounts of radioactive isotopes in the glass remains the dominant steady source of background photons, as neither the decay rates nor the scintillation yield depend on the external medium. The optical transition from glass to water, however, modifies photon transport. The higher refractive index of water compared to air increases the critical angle at the boundary, reducing the probability of total internal reflection and thus decreasing the fraction of scintillation photons that remain trapped within the vessel. Consequently, fewer photons are redirected toward the PMTs and the typical photon arrival times shorten. A small additional contribution may arise from Cherenkov emission in the surrounding water from electrons that leave the glass with sufficient energy, but this effect is subdominant.

In Figure 8.12 the influence of the radioactivity within the glass vessel is depicted. The Δt distributions (left) show the reduced fraction of detected photons in water. Cherenkov–induced structures below $-8\ \log_{10}(\mathrm{s})$ are suppressed by the applied 10 ns PMT deadtime, since all photons arriving within this interval are merged into a single hit. A small residual contribution remains, reflecting those rare cases where photons are separated by more than the deadtime. The slight shift of the uncorrelated peak in water towards higher Δt stems from a smaller total rate (Equation 8.6) and therefore longer waiting times. It is also reduced in water relative to air because fewer scintillation photons remain inside the vessel. The different temperatures summarize the temperature dependent scintillation yield well (Figure 4.2), especially looking at the correlated peak. The coincidence rates (right)

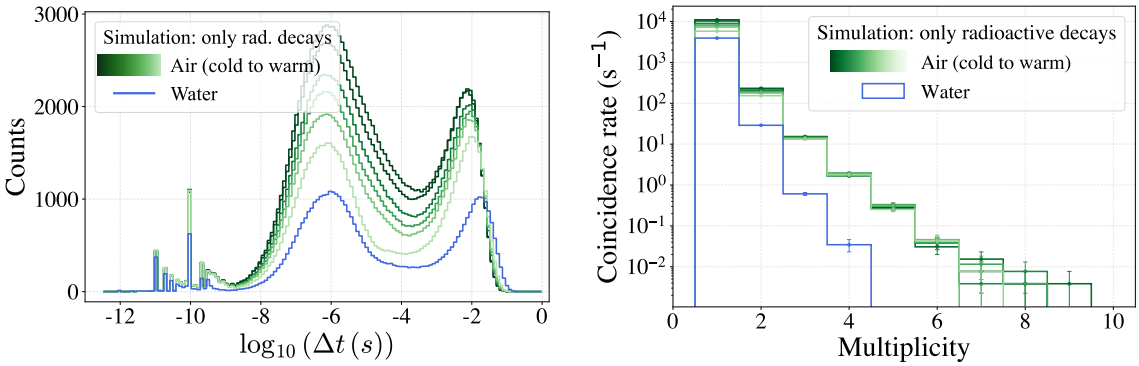

FIGURE 8.12: **Left:** Δt distributions for simulations including only intrinsic radioactivity of the mDOM placed in air (greens, $-40°C$ to $-18°C$) and in water (blue, $16°C$). **Right:** Corresponding coincidence rates.

further reflect the stronger total internal reflection inside the glass when the mDOM operates in air environment, which increases the number of photons retained within the vessel. This leads to higher multiplicities as well as an enhanced single PMT rate ($m = 1$) compared to the water configuration. The averaged per-PMT rates induced by the radioactive decays inside the mDOM including the standard deviation are:

$$\begin{aligned} \text{No PMT deadtime:} \quad & \bar{\mu}^{\text{rad}}_{\text{T,air}} = 299.4 \pm 5.8\ \text{s}^{-1}, \qquad \bar{\mu}^{\text{rad}}_{\text{T,water}} = 193.7 \pm 3.1\ \text{s}^{-1}, \\ 10\,\text{ns PMT deadtime:} \quad & \bar{\mu}^{\text{rad}}_{\text{T,air}} = 266.8 \pm 5.6\ \text{s}^{-1}, \qquad \bar{\mu}^{\text{rad}}_{\text{T,water}} = 172.3 \pm 2.9\ \text{s}^{-1}. \end{aligned} \tag{8.6}$$

Here, the suppression due to the deadtime is lower because the excess is dominated by the scintillation light. Compared to the muon induced rates in Equation 8.5 with PMT deadtime, this shows that the primary background in the mDOM arises from scintillation induced by trace radioactivity in the pressure vessel glass, according to the simulation results. While the comparison of the coincidence spectra induced by the muons (Figure 8.11) and by radioactivity (Figure 8.12) shows that the higher multiplicity region is highly dominated by the atmospheric muons.

In summary, the simulation datasets define the characteristic temporal and spatial signatures of atmospheric muons and trace radioactivity in the glass, thereby providing the reference required to interpret the the coincidence rates of both measurement and the combined simulation of both physical background components in Chapter 9.

9 Comparison of Measurement and Simulation

The calibration and characterization procedures established in the previous chapter provide a simulation (see Section 8.3.2) that reproduces the optical response of the DVT09 module for the physical sources present in the measurement, namely scintillation induced by trace radioactivity in the glass and Cherenkov emission from atmospheric muons. Detector specific effects such as intrinsic PMT dark noise and afterpulsing remain exclusive to the measurement and must therefore be accounted for separately in all subsequent comparisons.
This chapter compares the yield corrected simulation derived in Chapter 8 in combination with the atmospheric muon flux injection described in Chapter 7 with the measured mDOM background (Chapter 5) in both air and water environments. The comparison evaluates the temporal hit distribution and the spatial correlation, followed by an analysis of the coincidence rates.
Unless otherwise stated, the simulation takes the measured atmospheric muon flux $\Phi = 33.0 \pm 4.8\ \mathrm{m^{-2}\,s^{-1}}$ and angular index $n = 1.3$ determined in Chapter 6 as an input, the tank walls are simulated with 1 % reflectivity, accounting for both environments with a coincidence window of 50 ns. For all analyses, a deadtime of 10 ns was applied to each PMT individually in both measurement and simulation.
Throughout this Chapter, air results are shown in green (18°C), and water results in blue (16°C).

9.1 Mean PMT Rate

The total PMT rates averaged over all 24 PMTs for measurement and simulation are listed in Table 9.1. All values are listed including the standard deviation. The air results, decomposed into correlated and uncorrelated components in Figure 8.10, confirm the internal consistency of the simulation calibration procedure: after adding the detector specific contributions from afterpulsing and intrinsic PMT dark rate noise, the simulated sum reproduces the measured mean rates within uncertainties across all temperatures, and shows specifically across sub-zero temperatures good agreements between the simulation and measurement. The uncertainties in the measurement reflect the great PMT rate spread across all 24 PMTs and is especially elevated at warmer temperatures due to PMT dark noise fluctuations. Note that the listed values are obtained from the average rate excluding unstable PMTs listed in Table 8.1. For all subsequent discussions, they are not excluded.
In contrast, the water configuration exhibits a clear discrepancy between the simulated and measured PMT rate. The measured mean PMT rate of 2461 $\mathrm{s^{-1}}$ exceeds the simulated value of 569 $\mathrm{s^{-1}}$ by a factor of four, even after including the detector specific backgrounds

TABLE 9.1: Mean PMT rates from simulation and measurement. After including detector specific afterpulsing (AP) and intrinsic PMT dark rate (PMT-DR) the sum is used for comparison. All listed uncertainties are standard deviations. Unstable PMTs (Table 8.1) were removed to obtain the measured rates.

T (°C)	**Simulation** Mean PMT rate (s^{-1})	**Detector specific** AP / PMT-DR (s^{-1})	**Sum** Total (s^{-1})	**Measurement** Total (s^{-1})
Air				
18	276.0 ± 5.8	14.6 ± 1.3 / 348 ± 107	639 ± 108	717 ± 149
0	342.7 ± 7.2	16.8 ± 1.3 / 210 ± 41	570 ± 42	590 ± 98
-10	380.0 ± 6.8	21.8 ± 1.4 / 137 ± 15	539 ± 17	541 ± 36
-20	415.0 ± 7.7	23.9 ± 1.5 / 139 ± 15	578 ± 17	583 ± 36
-30	477.1 ± 8.8	29.0 ± 1.7 / 162 ± 14	668 ± 17	667 ± 40
-40	509.8 ± 9.2	32.5 ± 1.8 / 180 ± 16	722 ± 18	721 ± 38
Water				
16	206.5 ± 15.6	14.6 ± 1.3 / 348 ± 107	569 ± 108	2461 ± 870

absent in the simulation. As afterpulsing and intrinsic PMT dark noise are invariant under the change from air to water due to their embedding inside the mDOM, the excess indicates additional water-induced photon backgrounds not implemented in the simulation. The large uncertainty from the measured rate is a direct consequence of Cherenkov photons produced in the water, illuminating the frontside PMTs stronger (see Figure 8.3).
The investigation of the mean PMT rates confirms that the calibrated simulation reproduces the measured mean rates in air across all temperatures, whereas the pronounced rate in water demonstrates the presence of a medium dependent background that lies outside the simulated optical background.

9.2 TEMPORAL ANALYSIS

The temporal structure of the background is examined by analyzing the photon arrival statistics within and across coincidence windows.

9.2.1 Δt DISTRIBUTION

The normalized Δt distributions in Figure 9.1 (left air, right water) exhibit the characteristic structure of a superposition of correlated photon bursts and uncorrelated noise pulses. In the measured data, the correlated afterpulsing peak appears around -5.6 $\log_{10}(\mathrm{s})$, while the uncorrelated region follows the exponential waiting time distribution expected for statistically independent hits (Equation 8.1). The simulation curves are systematically shifted to larger Δt and display a reduced amplitude of the uncorrelated peak. This behavior follows directly from the lower absolute hit rates in the simulation (Table 9.1, first column) and the absence of intrinsic PMT dark noise, and a marginal contribution from afterpulsing. In the measurement, the $\mathcal{O}(350\,\mathrm{s}^{-1})$ thermionic component shortens the mean waiting

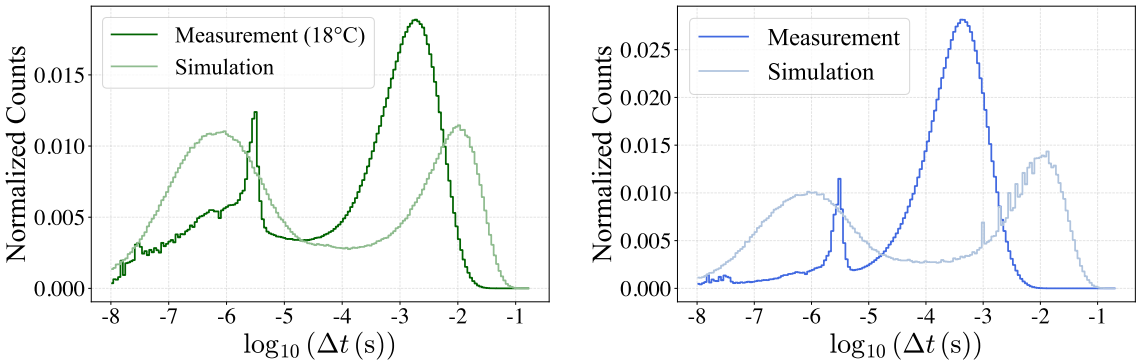

FIGURE 9.1: Normalized Δt distributions for air (**left**) and water (**right**) for measurement and simulation.

time and elevate the uncorrelated peak, whereas the simulation contains only the physical photon background.

9.2.2 Δt-MULTIPLICITY CORRELATION

Figure 9.2 shows the mean inter-hit timing $\langle \Delta t \rangle$ as a function of multiplicity for measurements and simulations in air and water. The quantity $\langle \Delta t \rangle$ denotes the average temporal separation between consecutive photon hits within a coincidence window of 50 ns. At low multiplicities, $\langle \Delta t \rangle$ is relatively large, reflecting uncorrelated photon arrivals, whereas increasing multiplicity produces a rapid decrease of $\langle \Delta t \rangle$ as the hit pattern becomes dominated by prompt Cherenkov photons from single muon tracks.

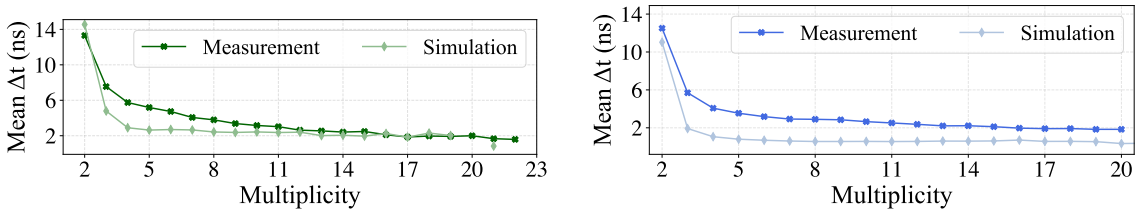

FIGURE 9.2: Mean inter-hit timing $\langle \Delta t \rangle$ within 50 ns coincidence events as a function of multiplicity for air (**left**) and water (**right**).

The simulations in both media show nearly constant and smaller values for $m > 3$, consistent with a pure prompt light scenario in which no additional stochastic pulses are present. The measurements lie systematically above the simulations. This deviation is caused by uncorrelated PMT pulses that the simulation does not include, predominantly thermionic dark noise and afterpulsing. The probability that at least one such pulse occurs within the $\Delta t_w = 50$ ns coincidence window is

$$P_{\text{rand,any}} = 1 - \exp\left(-N(\mu_{\text{DR}} + \mu_{\text{AP}})\,\Delta t_{\text{w}}\right) \approx 4 \times 10^{-4},$$

with $N = 24$ PMTs. Although this probability is small, each additional uncorrelated hit inserts a new temporal interval inside the fixed window. Because $\langle \Delta t \rangle$ is computed over all inter-hit intervals inside a fixed time window, a single uncorrelated pulse introduces an additional, typically long interval and therefore increases the mean rather than merely broadening its distribution. A secondary contribution originates from the PMT TTS of order 2-3 ns [28] which is not simulated.
The stronger discrepancy observed in water follows from its larger single-PMT rate and the medium dependent background identified earlier in Table 9.1, which increases the likelihood of uncorrelated hits and thus accentuate the shift in the measured curve.

9.3 SPATIAL CORRELATION ANALYSIS

Having established the temporal characteristics of photon detections through the Δt-multiplicity analysis, the spatial coherence of the detected photons hits is examined in this section.

9.3.1 PMT CORRELATION

This is achieved by evaluating the pairwise coincidence correlations between all PMTs. Figure 9.3 compares the normalized coincidence rates between any given pair of PMTs within the 50 ns coincidence window for measurements and simulations in air and water, respectively. The representation of the PMT ordering is differently chosen for air and water noted as lower-upper and back-front as depicted in Figure 9.3 corresponding to the asymmetric mDOM placement inside the water tank during measurements (see Figure 5.1).
In air (top), simulation and measurement show overall good agreement in both the global structure and the relative intensity pattern. The PMT ordering reflects the upper and lower hemispheres of the module, and enhanced lateral correlations between neighboring PMTs within each hemisphere indicate the spatial clustering of internally generated photons. The simulation, however, exhibits stronger correlations between vertically aligned equatorial PMTs of opposite hemispheres. This difference originates from the optical model: the glass vessel and the optical gel are treated as continuous media in the simulation, whereas the real mDOM consists of two glass hemispheres mechanically joined at the equatorial interface. Moreover, the optical gel does not fully fill the internal volume, creating an additional refractive boundary. Both interfaces act as weak Fresnel transitions that partially reflect and attenuate photons, thereby reducing inter-hemispheric transmission and suppressing the vertical correlations observed in the measurement, as quantified by the relative deviation matrix shown in the right panel. The reduced inter-hemispheric correlation originates from unmodeled optical interfaces at the equator (see Figure 9.4).

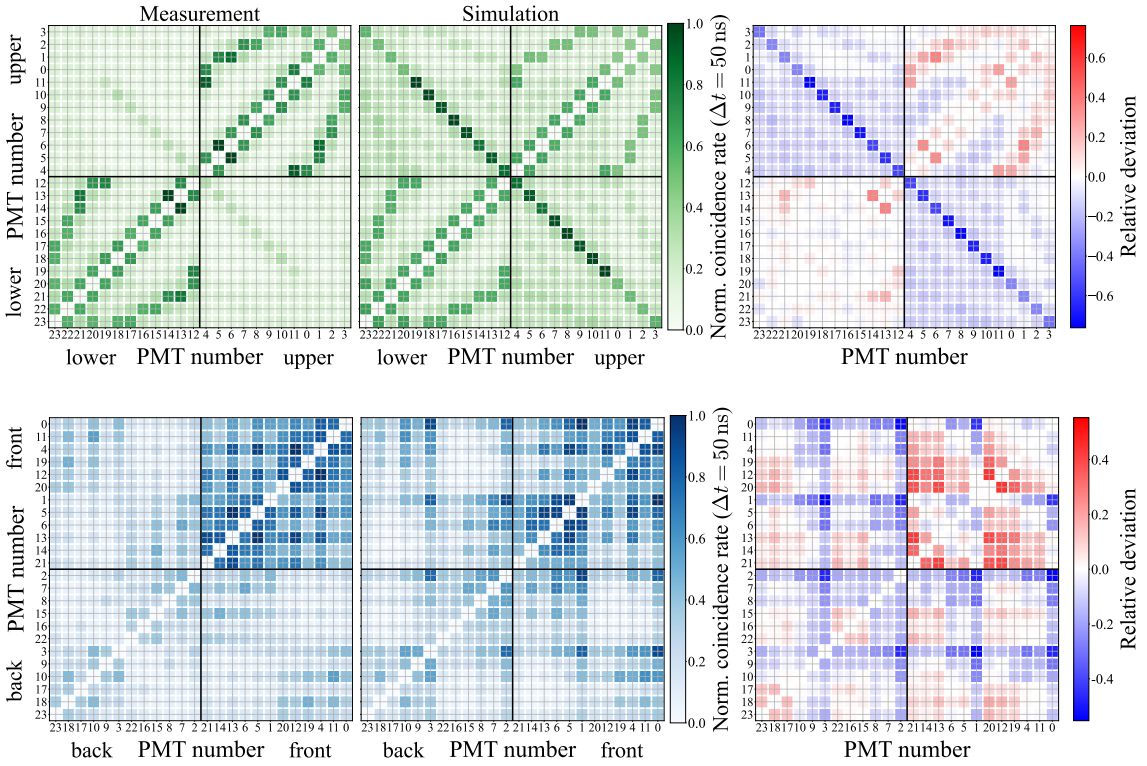

FIGURE 9.3: Normalized coincidence probability matrices between all PMT pairs for air (top) and water (bottom) and their relative deviation. The representation of the PMT ordering is differently chosen for air and water, noted as lower–upper and back–front.

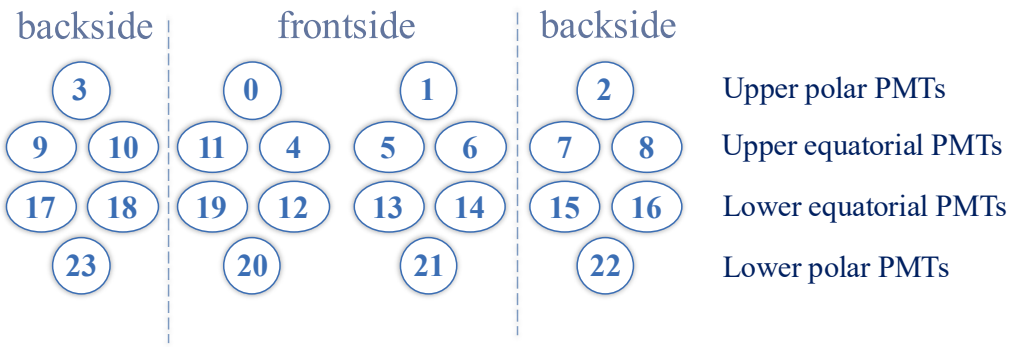

Figure 9.4: PMT ordering: PMTs pointing towards the open tank volume are denoted as frontside. Backside PMTs are close to the tank wall.

In water (bottom), the simulation shows increased correlations between PMTs in the upper hemisphere in comparison to the measurement, in particular the upper polar PMTs. One explanation might be the fact that during measurements the water level did not reach the nominal tank height, whereas the simulation assumes a completely filled volume. This was an oversight not accounted for in the simulation. The additional $\approx$ 30 cm simulated water increases the Cherenkov photon yield near the top of the module and could therefore enhance the simulated correlations for upper PMTs relative to the measurements. Future simulations should account for this.

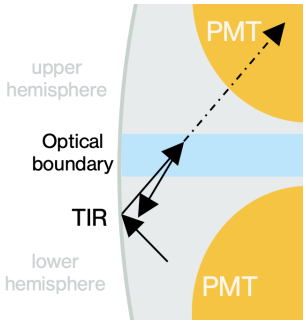

FIGURE 9.4: Schematic illustration of total internal reflection (TIR) and back-reflection at the optical boundary between the two glass hemispheres in the real mDOM.

The measurement shows the clear classification into front- and backside of the module orientation. While backfacing PMTs show less correlations, frontfacing reflect the directional Cherenkov light produced in the water surrounding.
Overall, this spatial correlation analysis demonstrates that the optical photon transport and PMT geometry are accurately represented in the simulation. Small discrepancies, such as the enhanced inter-hemispheric correlation in air and the stronger correlated upper polar PMTs in the simulation, can be attributed to the simplified modeling of the equatorial interface between the hemispheres and the different water level in measurement and simulation.

9.3.2 PMT PARTICIPATION PROBABILITY

The relative contribution of each PMT to coincidence events as a function of the multiplicity is shown in Figure 9.5. It represents the conditional probability $P(\text{PMT}|m)$ that a given PMT contributes to a coincidence event of multiplicity m within 50 ns. Each column is normalized such that $\sum_i P_i(m) = 1$, corresponding to the relative likelihood for a PMT to participate in an event with m coincident hits within the 50 ns window. Darker regions therefore indicate PMTs contributing more frequently to coincidence events of the respective multiplicity.

In air (top), both measurement and simulation exhibit an overall uniform response across most PMTs, consistent with isotropic photon generation. Above $m > 16$, statistical fluctuations dominate the pattern, and are therefore omitted in the figure. Both simulation and measurement show a moderate increased participation for the lower polar PMTs (20-23), nevertheless considerably stronger in the simulation. This is most pronounced at intermediate multiplicities ($m \approx$ 5–13). This feature suggests a locally increased optical photon density near the lower hemisphere due to geometrical effects, which favorable guide photons towards these PMTs. As the simulation models the boundary between both hemisphere ideally, it is plausible, that this feature is more pronounced in the simulation.
In water (bottom), both measurement and simulation show the expected front–back anisotropy associated with the directional Cherenkov field from through-going atmospheric

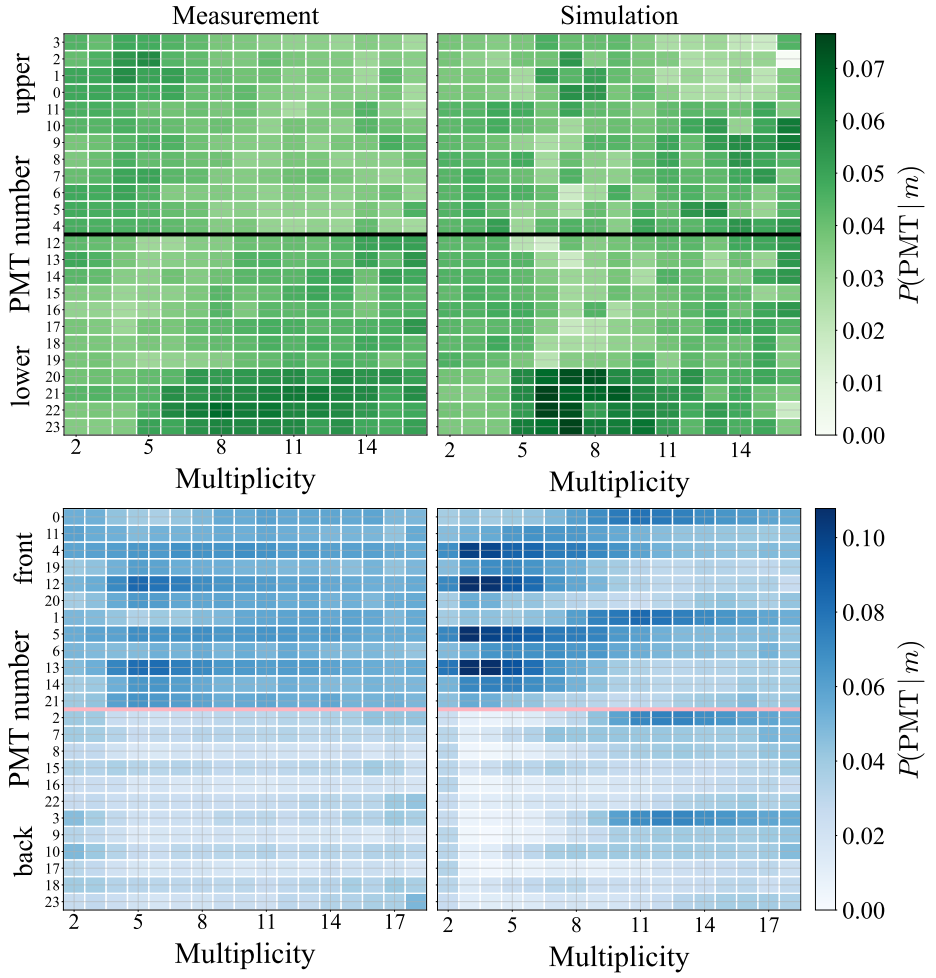

FIGURE 9.5: Conditional probability $P(\mathrm{PMT}|m)$ that a PMT participates in a coincidence event of multiplicity m for air (**top**) and water (**bottom**). Each column is normalized to unity. The representation of the PMT ordering is differently chosen for air and water noted as lower-upper and back-front.

muons as aleardy seen in Figure 9.3. Front-facing PMTs exhibit enhanced participation across all multiplicities, while backside PMTs, viewing the tank wall, contribute substantially less. The simulation reproduces this behavior but systematically overestimates the participation of several front-facing PMTs, especially PMTs 4, 5, 12, and 13. In addition to this effect, the simulation also overestimates the participation of the upper polar PMTs (0–3) at higher multiplicities. The preference was already observed in Figure 9.3 and supports the hypothesis of the difference in the water level of approximately 30 % between measurement and simulation. All four upper polar PMTs start contributing stronger at $m = 10$, likely stemming from close-by downgoing muons, consistent with an increased Cherenkov photon yield due to the higher water-level.

9.4 COINCIDENCE RATES

In Section 8.4, the individual influences of the atmospheric muon flux and photons from scintillation within the pressure vessel on the coincidence rate spectra were discussed. Throughout this section, the coincidence rates introduced in Section 8.4 from the combined background simulation and the comparison to the measurements are presented. Both simulation and measurement are taken under the same time conditions ($T_{\text{acq}} = 260\,\text{s}$ in both cases). Figure 9.6 shows the measured and simulated coincidence rates as a function of multiplicity for both media. The spectra shown are plotted with statistical uncertainties only.

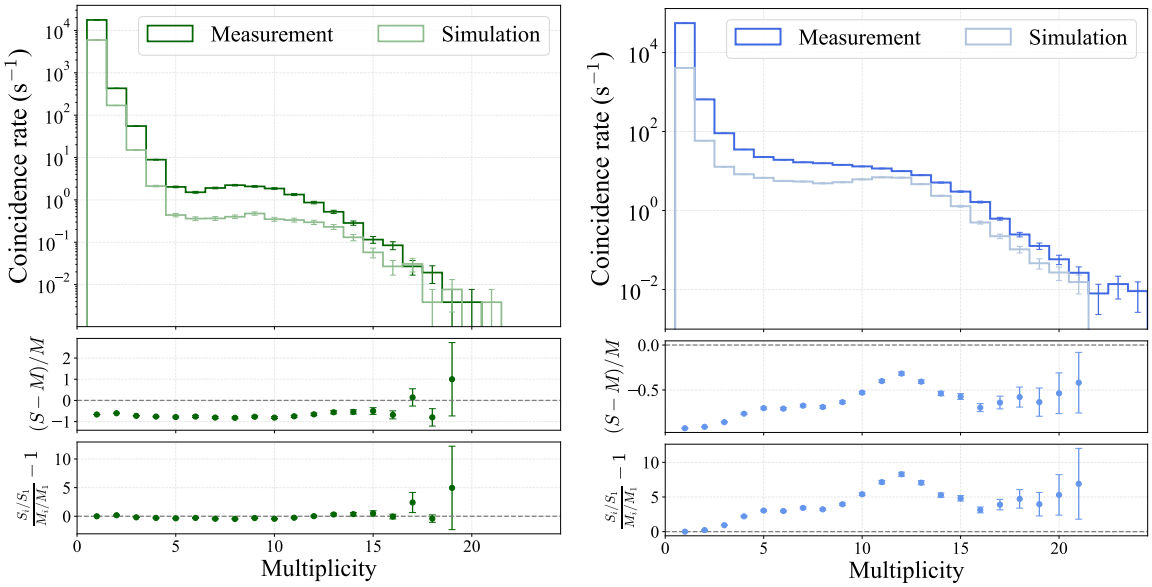

FIGURE 9.6: Measured and simulated coincidence rates as a function of multiplicity for air (left) and water (right).

In air, the simulation underestimates the measured coincidence rate across all multiplicities. This global offset is directly visible in the relative deviation $(S - M)/M$, where M and S denote the measurement and simulation rate, which remains approximately flat and negative over the entire multiplicity range, demonstrating that the simulation systematically underestimates the absolute rate without introducing a multiplicity dependent distortion. However, the shape of the multiplicity spectrum is well reproduced. This is quantified by normalizing both spectra to their respective single rate at $m = 1$ and forming

$$R_i = \frac{(S_i/S_1)}{(M_i/M_1)} - 1,$$

which remains close to zero up to high multiplicities. This indicates that the relative spectral shape is consistent between measurement and simulation, despite the overall normalization mismatch. Both measurement and simulation show a characteristic elevation at intermediate multiplicities, generated by correlated Cherenkov photons from throughgoing atmospheric muons and time-delayed photons retained within the optical module.

Deviations at $m > 15$ are supposed to be dominated by statistical fluctuations.

In water, likewise the simulation underestimates the measurement across all multiplicities, but the structure of the discrepancy differs substantially from results in air. The measured spectrum follows a smooth, monotonic decrease with multiplicity, while the simulation is lower in the low-multiplicity regime and approaches the measurement at high multiplicities. The excess for $m < 5$ is substantially larger than in air and indicates additional uncorrelated photon sources in the tank that are absent in the simulation. This interpretation is supported by the elevated single-PMT rates in water (see Table 9.1) and would manifest as uncorrelated background contributing only in the lower m-range.

Trace radionuclides present in the water may contribute to this effect but cannot account for the full discrepancy: the potassium content of the fill water (7.9 mg, K/l [55]) corresponds to approximately 66 g of potassium in the tank volume. With a natural ^{40}K abundance of 1.17×10^{-4} and a half-life of 1.3×10^{9} yr [56], the resulting activity is $A \simeq 2 \times 10^{3}$ s^{-1}. The number of Cherenkov photons is therefore of order 10^{5} s^{-1}, corresponding to only a few photons per PMT per second. Thus ^{40}K alone is insufficient.
Beyond ^{40}K, further backgrounds might arise from radioactive impurities in the tank walls, the water itself, and the optical module glass. Any β or γ emission depositing energy in the water produces Cherenkov light, while radioactive energy depositions in the water may additionally generate scintillation light. The scintillation properties of the water were not measured, and the simulation does not include any of these processes. Radioactive decays occurring outside the mDOM predominantly illuminate only one or a few PMTs, which populates exactly the low-multiplicity regime where the discrepancy is observed. A quantitative modeling of these contributions was beyond the scope of this thesis. Another consideration should take the luminescence of water into account. In [**AnnaPollmann**] dedicated measurements of the luminescence yield of water were performed, showing a non-negligible yield, $Y \simeq 0.5\,\gamma\,\mathrm{MeV}$. The consideration of this was beyond the scope of this thesis.
The relative deviation $(S - M)/M$ reflect this behavior: they are strongly negative at low multiplicities, indicating the pronounced deficit of simulated uncorrelated photons, and rise toward zero at higher multiplicities, where muon-induced correlated light dominates. The normalized residuals, $(S_i/S_1)/(M_i/M_1) - 1$ increase strongly with multiplicity up to $m = 12$ and reach values of order 3–7. This behavior is not a physical excess of high-multiplicity events in the simulation but a direct consequence of the underestimated single-PMT rate S_1. Because the simulation lacks several uncorrelated background components present in the water measurement, $M_1 \gg S_1$, and all ratios S_i/S_1 are biased high. At multiplicities $m > 12$, the residuals no longer follow a systematic upwards trend but decrease again, flatten for higher m, indicating that the muon-dominated high-multiplicity tail is reproduced with correct relative scaling. Around $m \simeq 10$–14 the simulation shows a elevated peak, which could be consistent with the observation earlier (Figure 9.5) that upper polar PMTs contribute stronger starting at $m = 10$, which artificially increases the multiplicity.

The coincidence-rate comparison shows that the simulation reproduces the shape of the rate behavior in good agreement. However, in both media, the simulation is underestimated, resulting in a systematic offset. In air, this offset is global and constant. Furthermore, the qualitative shape of the distribution is also reproduced for water, the offset is not constant. Together with the highly underestimated single rate ($m = 1$) this leads to the conclusion that the measurement contains background sources producing hits in the low-multiplicity region. The next section investigates the observed deviations between measurement and simulation.

9.5 INVESTIGATION OF SYSTEMATIC EFFECTS

The observed deviations between measurement and simulation motivate a systematic evaluation of selected simulation parameters and experimental conditions that influence the coincidence rates.

9.5.1 VARIATION OF MUON FLUX NORMALIZATION

The constant offset observed in air in Figure 9.6 suggests that the measured coincidence spectrum may be biased by an underestimated atmospheric muon flux normalization. The flux used so far, $\Phi = 33\ \mathrm{m}^{-2}\,\mathrm{s}^{-1}$, is derived from the scintillation panel measurement described in Chapter 6. This value is subject to a simplified detector setup, which might bias the atmospheric muon flux downward, as any inefficiency directly translates into a reduced reconstructed flux.
For comparison, Chapter 6 provides an independent theoretical estimate obtained by propagating the open-sky muon spectrum through the building material. This model explicitly incorporates the building overburden and yields a flux normalization of $\Phi = 83\ \mathrm{m}^{-2}\,\mathrm{s}^{-1}$ (Equation 6.10) for the same angular index $n = 1.3$ derived from the measurement. Although based on simplified geometry and continuous energy-loss assumptions, this estimate represents a physically motivated atmospheric muon flux in the laboratory. To assess the sensitivity of the coincidence spectra to this normalization ambiguity, the simulation was repeated using the theoretical estimated higher flux, $\Phi = 83\ \mathrm{m}^{-2}\,\mathrm{s}^{-1}$ with $n = 1.3$. Figure 9.7 shows the comparison for both media.

Increasing the flux reduces the gap between measurement and simulation across all multiplicities. The relative deviations and the residuals remain stable and flat up to $m \simeq 14$, confirming that the spectral shape is unchanged and that the improvement concerns only absolute scaling.
In water, the higher flux increases the simulated rate at all multiplicities. At low multiplicities the simulation remains below the measurement, most likely due to an unknown external background from the water tank as discussed in Section 9.4, which is not accounted for in the simulation. Again, the simulation exhibits an excess around $m \simeq 10$–14, and

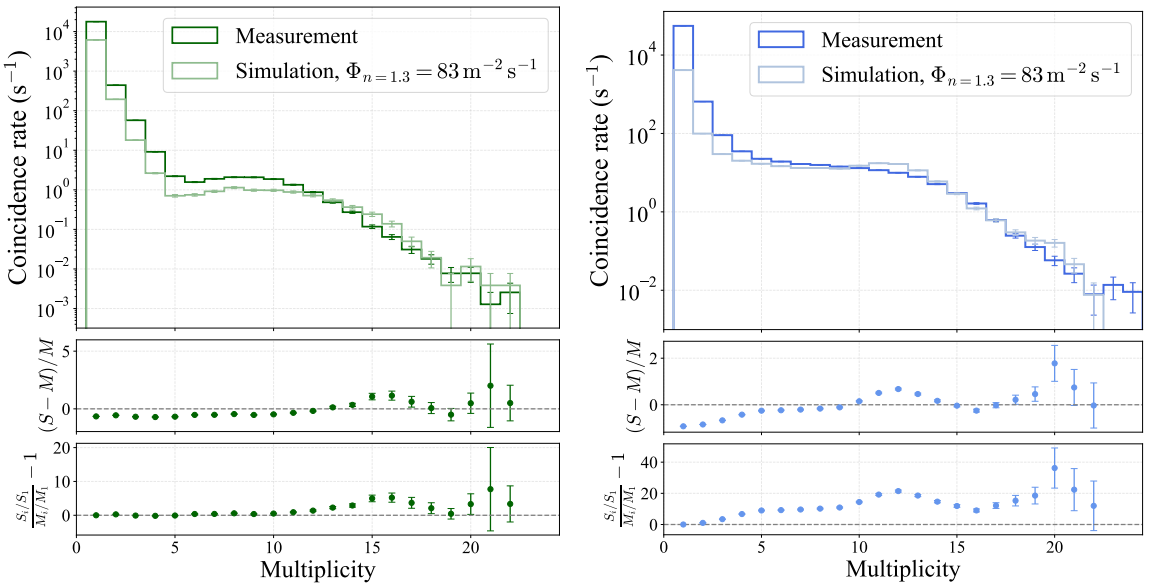

FIGURE 9.7: Measured and simulated coincidence rates as a function of multiplicity for air (left) and water (right). The simulation was performed with atmospheric muon flux normalization $\Phi_{n=1.3} = 83\ \mathrm{m}^{-2}\,\mathrm{s}^{-1}$.

the simulation exceeds the measurement, which arises from the higher photon yield seen by the upper polar PMTs in the simulation due to the overestimated water level. Beyond that multiplicity region, the simulation and measurements agree before large fluctuations occur.

Table 9.2 lists the mean PMT rate of the higher flux, $\Phi_{\mathrm{n=1.3}} = 83\ \mathrm{m}^{-2}\,\mathrm{s}^{-1}$. For comparison, the measured and lower flux ($\Phi = 33\ \mathrm{m}^{-2}\,\mathrm{s}^{-1}$) rates are also listed. The higher flux normalization does increase the rate only by a few percent.

In conclusion, the muon flux normalization $\Phi = 83\ \mathrm{m}^{-2}\,\mathrm{s}^{-1}$ decreases the constant discrepancy of the coincidence rates between measurement and simulation in air. In water, the discrepancy is likewise reduced, leading to better overall consistency. At large multiplicities statistical fluctuations arise. In water, the distinct excess around $m \simeq 12$ might be explained by the different nominal water level heights in measurement and simulation, leading to a greater participation of the upper polar PMTs in the simulation. When the mDOM is placed in water, the measurements revealed an increased mean PMT rate (Table 9.1), which is not visible in the simulation. This missing uncorrelated background contributes to the low multiplicity bins, hence, increasing the deviations between measurement and simulation in the lower region. This is not observed in the air plot, as the offset between measurement and simulation is constant. Intrinsic PMT dark noise and afterpulsing would not contribute to the higher multiplicities. The remaining, however, smaller, constant offset in air for multiplicities up to $\simeq 10$ suggests a slightly higher flux normalization. However, this flux would make the simulation exceed the measurement at higher multiplicities, thereby increasing the deviation between measurement and simulation.

TABLE 9.2: Mean PMT rates for simulation with $\Phi = 33\ \mathrm{m^{-2}\,s^{-1}}$ and $\Phi = 83\ \mathrm{m^{-2}\,s^{-1}}$, compared to the measurement. PMT afterpulsing and intrinsic dark noise are added to the simulation values. Rates for Φ_{33} and measurement were already shown in Table 9.1.

Medium	$\mu_{\mathrm{sim}}(\Phi = 33)$ (1/s)	$\mu_{\mathrm{sim}}(\Phi = 83)$ (1/s)	μ_{meas} (1/s)
Air	639 ± 108	653 ± 109	717 ± 149
Water	569 ± 108	613 ± 109	2461 ± 872

9.5.2 ANGULAR DISTRIBUTION

The zenith dependence of the atmospheric muon flux used in the simulations follows the empirical form $I(\theta) = I_0 \cos\theta^n$. The exponent was determined in Chapter 6, yielding $n = 1.3 \pm 0.2$ (Equation 6.7). This fitted value is used for all simulations employing either the measured flux normalization $\Phi = 33\ \mathrm{m^{-2}\,s^{-1}}$ or the theoretically estimated normalization $\Phi_{n=1.3} = 83\ \mathrm{m^{-2}\,s^{-1}}$. The theoretical estimate accounts for the building overburden but does not independently constrain the angular distribution. Consequently, the true exponent within the laboratory may deviate from the fitted value.

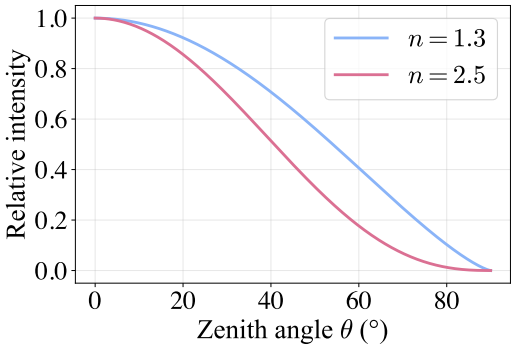

FIGURE 9.8: Relative zenith distributions for the angular exponents $n = 1.3$ and $n = 2.5$.

To quantify the sensitivity of the coincidence rates to such deviations, two simulations were performed with identical flux normalization of $\Phi = 83\ \mathrm{m^{-2}\,s^{-1}}$ but different angular exponents. One uses the fitted value $n = 1.3$, while the second adopts a steeper distribution with $n = 2.5$, representative of a more vertical dominated muon flux (see Figure 9.8). The resulting coincidence rates are shown in Figure 9.9. In both air (left) and water (right), the two angular hypotheses lead to nearly identical multiplicity shapes and normalizations. With the total flux fixed, the integrated number of muons entering the tank remains unchanged, and the different angular weightings produce only minimal modifications to the spatial illumination of the module. The coincidence rates therefore exhibit no significant dependence on the precise value of the exponent.

9.5.3 VARIATION OF COINCIDENCE TIME WINDOW

The previous multiplicity spectra were computed using a fixed coincidence window of 50 ns. Enlarging this window modifies the probability that additional, temporally uncorrelated photon hits fall inside a coincidence event, and therefore provided a direct probe of the temporal structure of the underlying optical background. Figure 9.10 shows the measured and simulated multiplicity spectra obtained for coincidence windows of 25 ns, 1 µs, 500 µs and 1 ms for both air (top) and water (bottom) using $\Phi_{n=1.3} = 83\ \mathrm{m^{-2}\,s^{-1}}$ as an

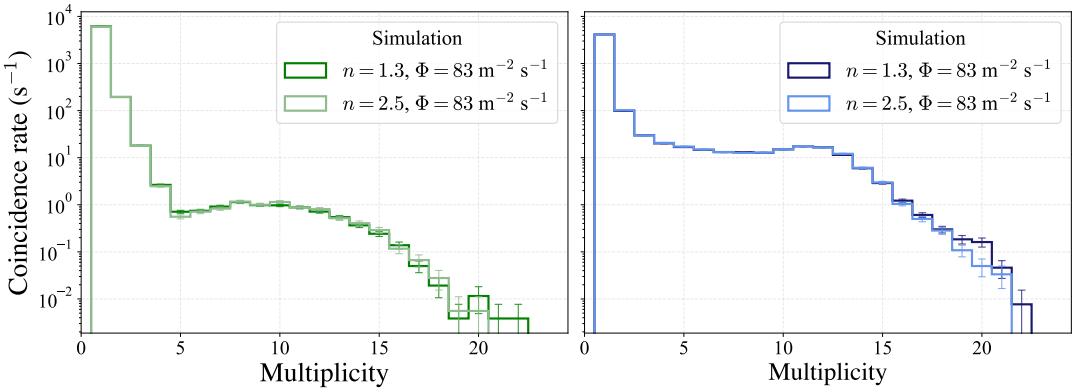

FIGURE 9.9: Simulated coincidence-rate spectra in air (left) and water (right) for angular exponents $n = 1.3$ and $n = 2.5$, using a fixed flux normalization of $\Phi = 83\,\mathrm{m}^{-2}\,\mathrm{s}^{-1}$.

input. In air, enlarging the coincidence window predominantly increases the probability that intrinsic PMT dark noise hits fall inside a local coincidence window Δt_{LC}. At 18 °C, the intrinsic PMT dark rate is $\mu_{\mathrm{DR}}^{\mathrm{PMT}} \approx 350\,\mathrm{s}^{-1}$ per PMT (see Table 8.2), corresponding to a total PMT dark rate of $8400\,\mathrm{s}^{-1}$ for the complete mDOM. The probability that at least one dark noise pulse occurs inside Δt_{LC} is

$$P(\Delta t_{\mathrm{LC}}) = 1 - e^{-\mu_{\mathrm{tot}}\,\Delta t_{\mathrm{LC}}}.$$

This yields $P(1\,\mu\mathrm{s}) < 1\,\%$, but $P(500\,\mu\mathrm{s}) \simeq 98.5\,\%$ and $P(1\,\mathrm{ms}) \simeq 99.98\,\%$. Thus, essentially every time window contains at least one uncorrelated PMT pulse. Because these pulses are spatially uncorrelated and uniformly distributed across the 24 PMTs, they accumulate within each coincidence window and shift the measured multiplicity distribution systematically toward higher multiplicities while depleting the lowest bins. The simulation does not exhibit this behavior because it contains neither intrinsic PMT dark noise nor afterpulsing. Accordingly, the spectra show only a weak dependence on Δt_{LC}, with a moderate increase in rate only when the window extends far beyond the prompt-light scale.

In water, enlarging the coincidence window reveals a qualitatively similar behavior. The simulation shows only a weak dependence on Δt_{LC} because it contains only the physical photon background from intrinsic radioactivity in the glass and atmospheric muons. Both physical photon sources included in the simulation—Cherenkov emission from atmospheric muons and scintillation from trace radioactivity in the glass—produce photon fields that are effectively prompt on the time scales relevant for the coincidence windows considered here. Cherenkov emission is instantaneous, and although glass scintillation exhibits decay constants in the µs regime, the resulting photons are emitted locally inside the module and illuminate only a limited subset of PMTs. Because the simulation does not include intrinsic PMT dark noise or afterpulsing, these localized scintillation bursts do not accumulate additional uncorrelated hits. Consequently, the simulated multiplicity spectra remain nearly invariant when Δt_{LC} is increased from tens of ns to the ms range.
In the measurement the situation is different. A substantial fraction of the observed single-PMT rate originates from PMT-intrinsic processes. These uncorrelated pulses populate all

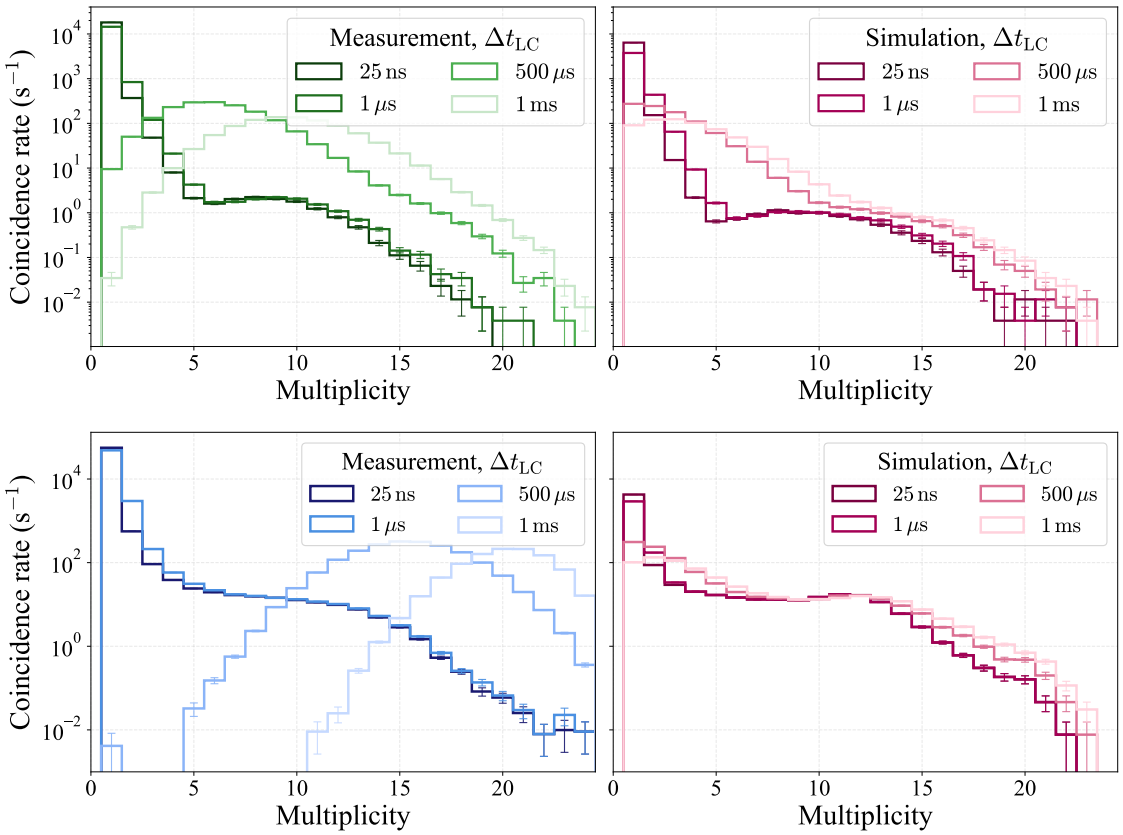

FIGURE 9.10: Multiplicity spectra for coincidence windows of 25 ns, 1 µs, 500 µs and 1 ms in air (top) and water (bottom), compared to simulation.

PMTs uniformly and independently of the optical photon field. As Δt_{LC} increases, the probability for such pulses to enter a coincidence window rises steeply and they add statistically independent hits to all multiplicities. This mechanism is absent in the simulation and therefore explains why the measured multiplicity spectra increase strongly at large Δt_{LC}, while the simulated spectra remain nearly unchanged. In water the effect is enhanced by the significantly higher total PMT rate, which further increases the probability of uncorrelated pulses contributing to each coincidence window.

A realistic simulation of these effects requires the inclusion of intrinsic PMT dark noise and afterpulsing, as well as a characterization of the medium-dependent background in water. Possible origins include radiogenic β- and γ-decays in the water, and photons undergoing extended propagation due to scattering or reflections in the tank. All such processes contribute uncorrelated single-PMT hits that naturally accumulate at large Δt_{LC} and explain the observed behavior in the measured spectra.

9.5.4 Tank-Wall Reflectivity

The reflectivity of the tank walls represents an additional optical parameter that can influence photon propagation inside the water volume, and thereby the resulting coincidence rates. The tank used in the measurements is constructed from black plastic, which is expected to exhibit low reflectivity.
To assess the impact of this parameter, simulations were performed with wall reflectivities of 1 %, 3 % and 5 % using $\Phi_{n=1.3} = 83\ \mathrm{m}^{-2}\,\mathrm{s}^{-1}$. The resulting coincidence rates for the water configuration are shown in Figure 9.11. Increasing the reflectivity primarily affects the muon-dominated high-multiplicity region. As the reflectivity increases, a larger fraction of photons undergoes wall reflections and remains within the tank volume, leading to a small but systematic increase in the coincidence rate at high multiplicities. At low multiplicities, where uncorrelated photons dominate, the effect is negligible because the absorption length of water in the relevant wavelength range is only of order a few meters, i.e. short compared with the tank dimensions, causing most photons to be absorbed before a wall reflection can contribute [49].

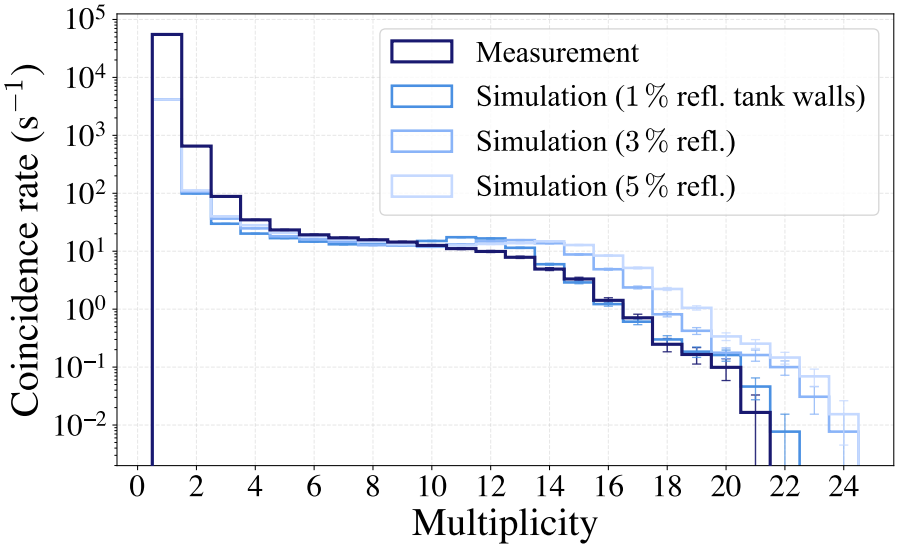

FIGURE 9.11: Coincidence-rate spectra in water for simulations with tank-wall reflectivities of 1 %, 3 % and 5 %, shown together with the measurement.

9.5.5 Environmental Light Influence

The measurements were intended to be performed under light-tight conditions, with the roller shutters of the water-tank setup designed to block external illumination. Long-exposure photographs taken inside the tank with the shutters closed and the laboratory ceiling lights switched on revealed several localized points of stray-light penetration. To assess whether this leakage could influence the coincidence rates, dedicated measurements were taken with the laboratory lights switched on and off while the mDOM was

operated in water.
The resulting coincidence spectra, shown in Fig. 9.12, exhibit no measurable difference between the two conditions. These datasets were recorded at an early stage of the project using a preliminary processing algorithm based on a sliding Δt_{LC} instead of a fixed Δt_{LC}, and the spectra are therefore not directly comparable to the coincidence rates presented in the previous sections. Nevertheless, any meaningful sensitivity to environmental illumination would manifest as an overall enhancement of the coincidence rate across all multiplicities. The absence of such a change demonstrates that stray light does not contribute to the observed background and can be excluded as a source of the strong low-multiplicity excess observed in water (see Table 9.1).

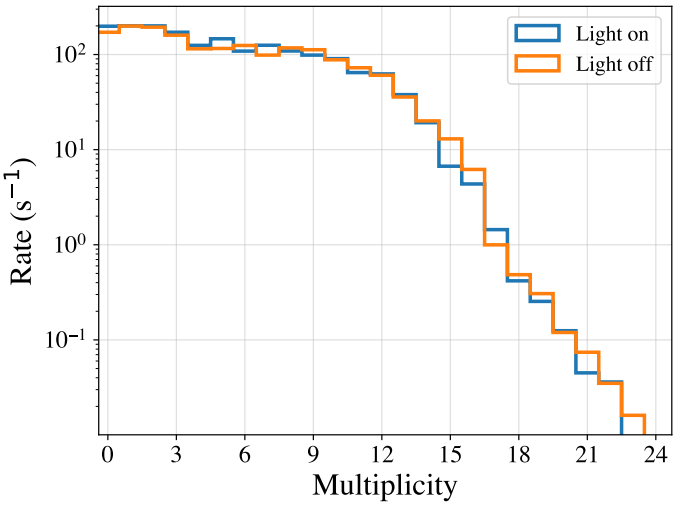

FIGURE 9.12: Multiplicity spectrum in water with the laboratory ceiling lights switched on and off, showing no detectable influence of external illumination. This multiplicity spectrum was evaluated using a different analysis algorithm and is therefore not directly comparable to the one presented previously.

10 Summary and Outlook

This thesis aimed to validate the simulation of the mDOM within the OMSim framework [8] by benchmarking its predicted background behavior against controlled measurements in air and water. Since an experimental characterization under true in-ice conditions is not feasible, these controlled environments are essential for constraining the simulation and enable a reliable projection of the mDOM performance to the IceCube Upgrade detector.

A genuine comparison between measurement and simulation requires that all background components relevant in the laboratory environment are consistently represented in the model. In the mDOM, the dominant contributions arise from trace radionuclides contained in the borosilicate pressure vessel glass, from intrinsic PMT dark noise, and atmospheric muons. The dominant radioactivity-induced background is already implemented in OMSim, whereas the atmospheric muon contribution is specific to the laboratory conditions. For this reason, a dedicated two-panel scintillation measurement was performed, which yields a total downward muon flux of $\Phi_{\text{meas}} = (33.0 \pm 4.8)\ \text{m}^{-2}\ \text{s}^{-1}$, and was complemented by a theoretical estimate accounting for the building overburden, which results $\Phi_{\text{theo}} = (83.1 \pm 11.0)\ \text{m}^{-2}\ \text{s}^{-1}$.
The simulation was extended to include a muon injection model normalized to the atmospheric muon flux. Independent studies ([35, 21]) have shown that scintillation parameters of borosilicate glass vary between production batches. To account for this, the scintillation yield was calibrated to the specific DVT09 module by requiring that the simulated correlated PMT rate matches the measured one. This yield correction ensures that the simulation reproduces the optical photon production of the actual module.

After including detector-specific effects—intrinsic PMT dark noise and afterpulsing—the calibrated simulation reproduces the measured mean PMT rates in air across the full temperature range (Table 9.1). The temporal and spatial analyses in air confirm this result. Small residual discrepancies, such as enhanced inter-hemispheric correlations and elevated participation probabilities of lower polar PMTs in the simulation, were traced to simplified modeling of the pressure vessel and optical gel. The simulation treats these as continuous media, whereas the real mDOM contains refractive boundaries at the equator and gel gaps that attenuate inter-hemisphere photon transport.
The coincidence-rate spectra in air display a constant offset when using the measured flux Φ_{meas}, while their spectral shape is reproduced precisely. The simulation underestimates the absolute rate by roughly a factor of five. This demonstrates that the correlated-light physics is implemented correctly but that the absolute rate normalization is biased by an underestimated muon flux. Using the theoretical flux Φ_{theo} reduces this offset close to one and improves the agreement between measurement and simulation. The influence of absent uncorrelated hits in the simulation from intrinsic PMT dark noise and afterpulsing becomes most visible when the coincidence time window is enlarged from ns to ms: the

measurement shifts toward higher multiplicities, whereas the simulation remains nearly invariant, as it contains no stochastic PMT pulses by construction.

In water, Cherenkov photons are released in the environment of the mDOM due to traversing atmospheric muons. Comparing the mean PMT rates reveals a pronounced discrepancy between measurement and simulation: the simulated rate underestimated the measured rate by $1800\,s^{-1}$ per PMT (Table 9.2). The temporal and spatial analysis, together with the coincidence rates, demonstrates that this excess originates from uncorrelated photon hits. Potential sources such as ^{40}K in the water, tank-wall reflectivity variations, and environmental illumination were evaluated and found to be insufficient. A variation of the Geant4 production step size verified that the energy deposition and resulting photon emission are stable. The angular distribution of the muon flux was also tested; modifying the exponent has no effect on the multiplicity spectra and thus cannot explain the mismatch of the mean PMT rate in water between measurement and simulation.
The spatial correlation in water further identified a systematic overestimation of upper polar PMT activity in the simulation. This effect is traced to an unaccounted mismatch in water level: the simulation assumed a fully filled tank, whereas the real measurement was performed with a water level approximately 30 cm lower. This increases the simulated Cherenkov photon flux on the upper polar PMTs and explains their disproportionate contribution in the simulation.

Altogether, the results demonstrate that the simulation reproduces the correlated optical background-scintillation and muon-induced Cherenkov light-once the scintillation yield is calibrated. The remaining discrepancies suggest that they stem from uncorrelated background absent in the simulation. In air, this is understood and explained by intrinsic PMT dark noise and afterpulsing. In water, they indicate an uncharacterized medium-dependent photon source, likely associated with trace radiogenic processes or luminescence of the water or tank materials.

The water was not characterized in this thesis. A dedicated measurement of water luminescence under controlled excitation would be necessary to assess whether this process contributes at the observed level. Future work should also measure the trace amounts of radioactive isotopes and dissolved impurities, quantify the photon yield from ^{40}K and other radionuclides, in order to validate the observed background excess. Implementing the equatorial glass interface and gel boundaries would bring the simulation to a higher level of accuracy. In particular, incorporating intrinsic PMT dark noise at room temperature and afterpulsing into OMSim would enable a more complete quantitative comparison.

A Atmospheric Muon Parametrizations

The atmospheric muon flux at the Earth's surface is commonly described by an empirical parametrization. A widely used expression is the standard Gaisser formula [**Gaisser1990**], which approximates the differential intensity of surface muons as

$$\frac{dN}{dE\,d\Omega}(E,\theta) \;=\; 0.14\,E^{-2.7}\left[\frac{1}{1+\frac{1.1\,E\cos\theta}{115\ \mathrm{GeV}}}+\frac{0.054}{1+\frac{1.1\,E\cos\theta}{850\ \mathrm{GeV}}}\right], \tag{A.1}$$

with the energy E in GeV and the zenith angle θ measured from the vertical. This expression accounts for muons from pion and kaon decays, and captures the competition between decay and reinteraction in the atmosphere. It is accurate in the range $E \gtrsim 100\,\mathrm{GeV}$ and $\theta \lesssim 70^\circ$, but becomes less reliable at large zenith angles where the flat-Earth approximation is no longer valid.

For improved accuracy at low energies and large zenith angles, Guan et al. [51] introduced a modified parametrization, which corrects for the curvature of the atmosphere and includes a low-energy suppression factor. The flux is expressed as

$$\frac{dN}{dE\,d\Omega}(E,\theta) \;\propto\; E^{-2.7}\left[\frac{1}{1+\frac{1.1\,E\cos\theta^*}{115\ \mathrm{GeV}}}+\frac{0.054}{1+\frac{1.1\,E\cos\theta^*}{850\ \mathrm{GeV}}}\right]\left(1+\frac{3.64}{E\,\cos^{1.29}\theta^*}\right)^{-2.7}, \tag{A.2}$$

where $\cos\theta^*$ is an effective zenith angle to account for the curved atmosphere. This parametrization reproduces measured surface muon intensities from $\mathcal{O}(1\,\mathrm{GeV})$ up to multi-TeV energies and across the full angular range.

In the simulation used for this thesis, muon energies are generated according to Equation (A.2).

B PMT SPECIFICATIONS

TABLE B.1: Requirements for mDOM PMT performance parameters [37] based on KM3NeT specification [57].

Metric	**Specification**	**Tested**
Operational Temperature	$-45°C$ to $30°C$	
Storage Temperature	$-60°C$ to $50°C$	
Cathode Voltage @ Gain 5×10^6	950 V to 1350 V	✓
Quantum Efficiency	$> 7\%$ @ 325 nm	
	$> 25\%$ @ 380 nm	✓
	$> 15\%$ @ 500 nm	✓
Mean SPE Amplitude	> 6 mV @ Gain 5×10^6 and 50 Ω load	✓
Transit-Time-Spread (σ)	< 2.0 ns (full frontal illumination @ SPE)	✓
Rise Time (10%–90%)	> 1.0 ns and < 5.0 ns (100 PE pulse)	✓
SPE Charge Resolution (σ)	< 0.7 PE	✓
Peak-to-Valley Ratio	> 2.0	✓
Amplitude Linearity (within 10%)	> 100 PE	
Prepulses [−20 ns, −10 ns]	$< 1\%$ @ 0.2 PE threshold and $-20°C$	✓
Late Pulses [15 ns, 80 ns]	$< 5\%$ @ 0.2 PE threshold and $-20°C$	✓
Afterpulses [100 ns, 12 μs]	$< 15\%$ @ 0.2 PE threshold and $-20°C$	✓
Dark Rate	< 150 Hz @ 0.2 PE threshold, $t_{\text{dead}} = 100$ ns, @ $-20°C$ after 5 h in dark	✓

C Additional Provided Figures

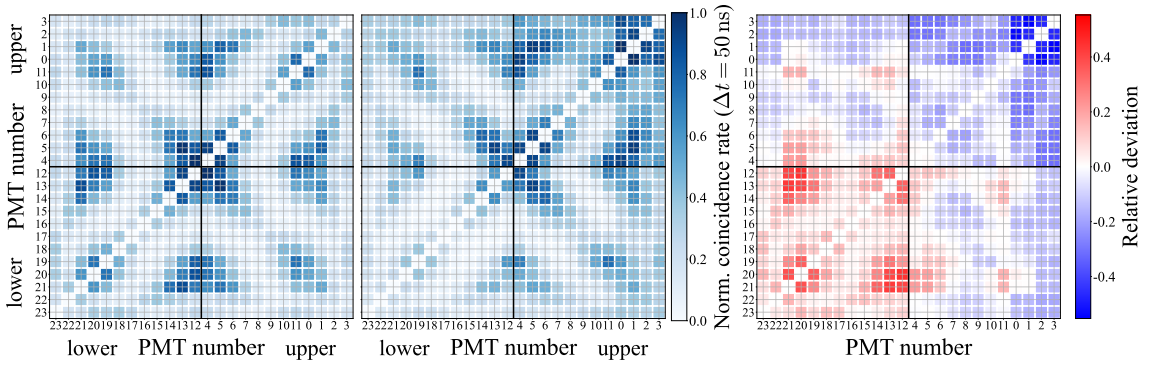

FIGURE C.1: Normalized coincidence probability matrices between all PMT pairs for water and their relative deviation. In this representation the PMTs are classified into lower and upper PMTs, directly comparable with the structure yielded in air in Figure 9.3.

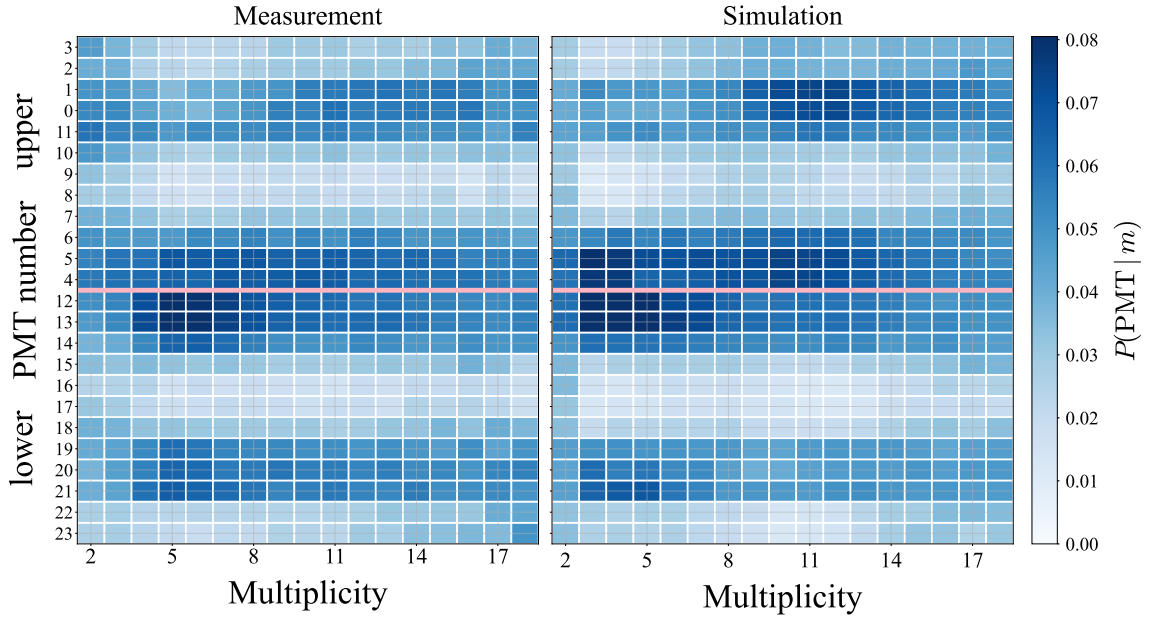

FIGURE C.2: Conditional probability $P(\mathrm{PMT}|m)$ that a PMT participates in a coincidence event of multiplicity m for water. In this representation the PMTs are classified into lower and upper PMTs, directly comparable with the structure yielded in air in Figure 9.5.

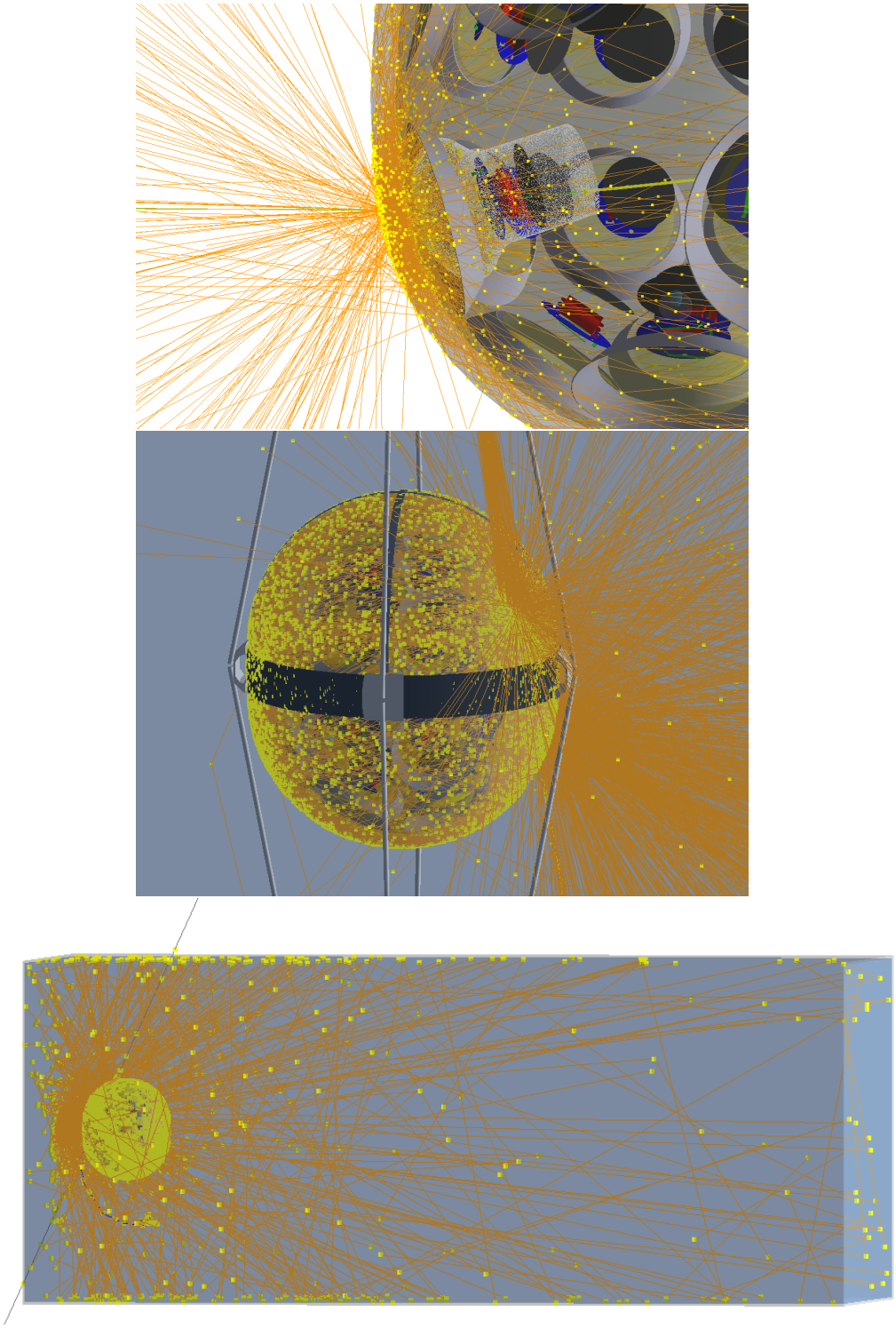

FIGURE C.3: Different perspectives of a simulated muon traversing the mDOM in an air environment, with photon paths shown in orange and interaction points in yellow.

BIBLIOGRAPHY

[1] IceCube Collaboration. "First observation of PeV-energy neutrinos with IceCube". *Phys. Rev. Lett.* 111 (2013), p. 021103. DOI: 10.1103/PhysRevLett.111.021103. arXiv: 1304.5356 [astro-ph.HE].

[2] IceCube Collaboration. "Evidence for High-Energy Extraterrestrial Neutrinos at the IceCube Detector". *Science* 342 (2013), p. 1242856. DOI: 10.1126/science.1242856. arXiv: 1311.5238 [astro-ph.HE].

[3] IceCube Collaboration. "Neutrino emission from the direction of the blazar TXS 0506+056 prior to the IceCube-170922A alert". *Science* 361 (2018), pp. 147–151. DOI: 10.1126/science.aat2890. arXiv: 1807.08794 [astro-ph.HE].

[4] IceCube Collaboration. "Evidence for neutrino emission from the nearby active galaxy NGC 1068". *Science* 378 (2022), pp. 538–543. DOI: 10.1126/science.abg3395. arXiv: 2211.09972 [astro-ph.HE].

[5] A. Ishihara for the IceCube Collaboration. "The IceCube Upgrade – Design and Science Goals". In: *Proceedings of Science (ICRC2019)*. Vol. 358. 2021, p. 1031. DOI: 10.22323/1.358.1031.

[6] L. Classen. "The mDOM: A Multi-PMT Digital Optical Module for the IceCube-Gen2 Neutrino Telescope". PhD thesis. Friedrich-Alexander-Universität Erlangen-Nürnberg, 2017.

[7] M G Aartsen et al. "IceCube-Gen2: the window to the extreme Universe". *Journal of Physics G: Nuclear and Particle Physics* 48.6 (Apr. 2021), p. 060501. DOI: 10.1088/1361-6471/abbd48.

[8] IceCube Collaboration. *OMSim: Geant4 Framework for IceCube Optical Module Studies*. https://github.com/icecube/OMSim. 2025.

[9] J. Alvarez-Muñiz et al. "Cosmic Rays". *Progress of Theoretical and Experimental Physics* 2024.8 (2024). Particle Data Group Review, p. 083C01. DOI: 10.1093/ptep/ptae083.

[10] Lars Bergström and Ariel Goobar. *Cosmology and Particle Astrophysics*. 3rd ed. Springer, 2021. DOI: 10.1007/978-3-030-65066-5.

[11] Alessandro De Angelis and Mário Pimenta. *Introduction to Particle and Astroparticle Physics: Multimessenger Astronomy and its Particle Physics Foundation*. 2nd ed. Springer, 2018. DOI: 10.1007/978-3-319-78181-8.

[12] Thomas K. Gaisser, Ralph Engel, and Elisa Resconi. *Cosmic Rays and Particle Physics*. 2nd ed. Cambridge University Press, 2016. DOI: 10.1017/CBO9781139192194.

[13] Robert Marcus Wagner. "Measurement of very high energy gamma–ray emission from four blazars using the MAGIC telescope and a comparative blazar study". PhD Thesis. Technische Universität München, 2006. URL: https://mediatum.ub.tum.de/doc/604099/.

[14] R. L. et al. (Particle Data Group) Workman. "Passage of particles through matter". *Progress of Theoretical and Experimental Physics* 8 (2022), p. 083C01. DOI: 10.1093/ptep/ptac097.

[15] IceCube Collaboration. "Energy Reconstruction Methods in the IceCube Neutrino Telescope". *Journal of Instrumentation* 9 (2014), P03009. DOI: 10.1088/1748-0221/9/03/P03009. arXiv: 1311.4767 [physics.ins-det].

[16] M. Aker et al. "Direct neutrino-mass measurement based on 259 days of KATRIN data". *arXiv:2406.13516* (2024).

[17] Carlo Giunti and Chung W. Kim. *Fundamentals of Neutrino Physics and Astrophysics*. Oxford University Press, 2007. ISBN: 978-0-19-850871-7.

[18] Bruce T. Cleveland et al. "Measurement of the Solar Electron Neutrino Flux with the Homestake Chlorine Detector". *The Astrophysical Journal* 496.1 (Mar. 1998), p. 505. DOI: 10.1086/305343. URL: https://doi.org/10.1086/305343.

[19] K. S. Hirata et al. "Real-time, directional measurement of ^{8}B solar neutrinos in the Kamiokande II detector". *Phys. Rev. D* 44 (8 Oct. 1991), pp. 2241–2260. DOI: 10.1103/PhysRevD.44.2241.

[20] The Royal Swedish Academy of Sciences. *The Nobel Prize in Physics 2015 – Press Release*. https://www.nobelprize.org/prizes/physics/2015/press-release/. Accessed: 2025-12-05. 2015.

[21] M.A. Unland Elorrieta. "Studies on dark rates induced by radioactive decays of the multi-PMT digital optical module for future IceCube extensions". MA thesis. Westfälische Wilhelms-Universität Münster and University of Sevilla, 2017.

[22] Mark Thomson. *Modern Particle Physics*. 7th printing, 2021. Cambridge University Press, 2013.

[23] R. Abbasi et al. "IceTop: The surface component of IceCube". *Nuclear Instruments and Methods in Physics Research Section A: Accelerators, Spectrometers, Detectors and Associated Equipment* 700 (2013), pp. 188–220. ISSN: 0168-9002. DOI: https://doi.org/10.1016/j.nima.2012.10.067.

[24] IceCube Collaboration. "Physics potential of the IceCube Upgrade for atmospheric neutrino oscillations". *arXiv preprint* (2025). arXiv:2509.13066v1. arXiv: 2509.13066 [hep-ex].

[25] S. Mechbal and N. Feigl. "Characterization and testing of the IceCube Upgrade mDOM". In: *Proceedings of Science (ICRC2023)*. Vol. 444. 2024, p. 1183. DOI: 10.22323/1.444.1183.

[26] IceCube Collaboration. "Physics potential of the IceCube Upgrade for atmospheric neutrino oscillations". *arXiv e-prints* (Sept. 2025). DOI: 10.48550/arXiv.2509.13066. arXiv: 2509.13066 [hep-ex].

[27] C. J. Lozano Mariscal et al. "Sensitivity of multi-PMT optical modules in Antarctic ice to supernova neutrinos of MeV energy". *European Physical Journal C* 81 (2021), p. 1058. DOI: 10.1140/epjc/s10052-021-09809-y.

[28] M. Unland Elorrieta. "Development and Characterisation of the Multi-PMT Digital Optical Module for the IceCube Upgrade". PhD thesis. Westfälische Wilhelms-Universität Münster, 2023.

[29] S. Adrián-Martínez et al. "The KM3NeT Multi-PMT Digital Optical Module". *Journal of Instrumentation* 8 (2013), P03006. DOI: 10.1088/1748-0221/8/03/P03006.

[30] R. Abbasi, K.-H. Sulanke, et al. "Design and performance of the multi-PMT optical module for IceCube Upgrade". In: *Proceedings of the 37th International Cosmic Ray Conference (ICRC2021)*. Vol. 395. PoS(ICRC2021). 2021, p. 1070. DOI: 10.22323/1.395.1070.

[31] M. G. Aartsen et al. "The IceCube Neutrino Observatory: instrumentation and online systems". *Journal of Instrumentation* 12.03 (2017), P03012. DOI: 10.1088/1748-0221/12/03/P03012.

[32] J. Schneider. "Characterisation of the mDOM and Simulation Studies for the IceCube Upgrade". PhD thesis. RWTH Aachen University, 2024. URL: https://doi.org/10.25593/open-fau-1009.

[33] A. G. Wright. "PMT background". In: *The Photomultiplier Handbook*. Oxford University Press, 2017. ISBN: 9780199655092. DOI: 10.1093/oso/9780199655092.003.0006.

[34] Hamamatsu Photonics. *Photomultiplier Tubes: Basics and Applications*. 4th. Datasheet / Handbook. 2017.

[35] M. Dittmer. "Characterisation of Scintillation Light Induced by Radioactive Excitation in the mDOM Glass Pressure Vessel". MA thesis. Westfälische Wilhelms-Universität Münster, 2020.

[36] L.Y. Halve. "Validation of Optical Sensors for the mDOM of the IceCube Upgrade". PhD thesis. RWTH Aachen University, 2024. DOI: 10.18154/RWTH-2024-05501.

[37] IceCube Collaboration. "Acceptance Tests of more than 10 000 Photomultiplier Tubes for the multi-PMT Digital Optical Modules of the IceCube Upgrade". *arXiv preprint arXiv:2404.19589* (2024). DOI: 10.48550/arXiv.2404.19589. arXiv: 2404.19589 [astro-ph.IM].

[38] T. Anderson et al. "Design and Performance of the mDOM Mainboard for the IceCube Upgrade". In: *Proceedings of the 38th International Cosmic Ray Conference (ICRC2023)*. Vol. 444. PoS. 2024, p. 0967. DOI: 10.22323/1.444.0967.

[39] W. R. Leo. *Techniques for Nuclear and Particle Physics Experiments*. Springer-Verlag Berlin Heidelberg, 1987. ISBN: 3-540-17386-2.

[40] R. Salh. "Defect Related Luminescence in Silicon Dioxide Network: A Review". In: *Crystalline Silicon — Properties and Uses*. Ed. by M. Martin. InTech, 2011. DOI: 10.5772/22607.

[41] M. Dittmer. "Characterization and Development Efforts Towards Optical Modules Intended for IceCube-Gen2 and Future Detector Extension: Sensitivity Studies on NGC 1068". PhD thesis. Münster, Germany: Westfälische Wilhelms-Universität Münster, in writing.

[42] M.A. Unland Elorrieta, A. Kappes, and A. Franckowiak. "Preliminary measurements of mDOM sensitivity in air". Unpublished. 2024.

[43] A.Sperling. *Aufbau und Test eines Plastikszintillatordetektors zur Demonstration kosmischer Strahlung*. Bachelor's Thesis. 2010.

[44] L. N. Bogdanova et al. "Cosmic muon flux at shallow depths underground". *arXiv:nucl-ex/0601019* (2006). URL: https://arxiv.org/abs/nucl-ex/0601019.

[45] Topographic-Map.com. *Topographic map of Münster*. Accessed: 2025-12-03. 2024. URL: https://de-de.topographic-map.com/map-gzvnx/M%C3%BCnster/.

[46] S. Agostinelli et al. "GEANT4—a simulation toolkit". *Nuclear Instruments and Methods in Physics Research Section A: Accelerators, Spectrometers, Detectors and Associated Equipment* 506.3 (2003), pp. 250–303. DOI: 10.1016/S0168-9002(03)01368-8.

[47] B. Herold. "Simulation and Measurement of Optical Background in the Deep Sea Using a Multi-PMT Optical Module". PhD thesis. Friedrich-Alexander-Universität Erlangen-Nürnberg (FAU), 2017.

[48] Francisco Javier Vara Carbonell. "Gel pad sensitivity studies and muon reconstruction in a water basin in Geant4 for IceCube multi-PMT optical modules". MA thesis. Westfälische Wilhelms-Universität Münster, 2022.

[49] Robin M. Pope and Edward S. Fry. "Absorption spectrum (380–700 nm) of pure water. II. Integrating cavity measurements". *Appl. Opt.* 36.33 (Nov. 1997), pp. 8710–8723. DOI: 10.1364/AO.36.008710.

[50] Curtis D. Mobley. *Light and Water: Radiative Transfer in Natural Waters*. Academic Press, 1994.

[51] M. Guan et al. "A parametrization of the cosmic-ray muon flux at sea-level". *Chinese Physics C* 40 (2015), p. 113001. DOI: 10.1088/1674-1137/40/11/113001. arXiv: 1509.06176 [hep-ex].

[52] M.A. Unland Elorrieta et al. "Characterisation of the Hamamatsu R12199-01 HA MOD photomultiplier tube for low temperature applications". *Journal of Instrumentation* 14.03 (Mar. 2019), P03015. DOI: 10.1088/1748-0221/14/03/P03015.

[53] S. Cecchini and M. Spurio. "Atmospheric muons: experimental aspects". *Geoscientific Instrumentation, Methods and Data Systems* 1.2 (2012), pp. 185–196. DOI: 10.5194/gi-1-185-2012.

[54] M. Dittmer. Private communication.

[55] Stadtwerke Münster. *Trinkwasseranalyse 2024*. https://opendata.stadt-muenster.de/dataset/trinkwasseranalyse-der-stadtwerke-mÃijnster.

[56] National Nuclear Data Center. *Nuclear Structure and Decay Data for* ^{40}K. URL: https://www.nndc.bnl.gov/.

[57] S. Aiello et al. "Characterisation of the Hamamatsu photomultipliers for the KM3NeT Neutrino Telescope". *Journal of Instrumentation* 13.05 (2018), P05035. DOI: 10.1088/1748-0221/13/05/P05035.

Acknowledgements

I would like to express my gratitude to Prof. Alexander Kappes for the opportunity to do both my Bachelor's and Master's theses within this interesting research field, as well as for the opportunity to participate in the mDOM production. I am grateful for the chance to gain insight into the IceCube experiment. I am thankful to the members of the working group—Martin, Markus, Javi, Berit, Daniel and Nicolai-for creating an environment in which I could seek help whenever needed.
And last, thanks to my beloved family, who had far too little of my time in recent years and was always supporting me, you are the best.